



Max-Planck-Institut für Metallforschung
Stuttgart

Segregation and Phase Transformations at Interfaces

Gabriel Alejandro López

Dissertation
an der
Universität Stuttgart

Bericht Nr. 157
Juli 2004

Segregation and Phase Transformations at Interfaces

Von der Fakultät Chemie der Universität Stuttgart zur
Erlangung der Würde eines Doktors der Naturwissenschaften (Dr.rer.nat.)
genehmigte Abhandlung

Vorgelegt von

Gabriel Alejandro López

aus San Pedro/Argentinien

Hauptberichter: Prof. Dr. Ir. E.J. Mittemeijer

Mitberichter: Prof. Dr. Dr. h. c. M. Rühle

Mitprüfer: Prof. Dr. F. Aldinger

Tag der Einreichung: 07.05.2004

Tag der mündlichen Prüfung: 27.07.2004

INSTITUT FÜR METALLKUNDE DER UNIVERSITÄT STUTTGART
MAX-PLANCK-INSTITUT FÜR METALLFORSCHUNG
STUTTGART, 2004

Contents

1. Introduction	1
1.1. General remarks	1
1.2. Scope and contents of this thesis	2
2. Grain-boundary and surface segregation in the Cu–Bi system ...	7
Abstract	7
2.1. Introduction	9
2.2. Experimental details.....	11
2.2.1. <i>Specimen preparation</i>	11
2.2.2. <i>Auger electron spectroscopy</i>	14
2.3. Results and discussion	15
2.4. Conclusions	21
3. The solubility of C in solid Cu	23
Abstract	23
3.1. Introduction	25
3.2. Experimental details.....	27
3.2.1. <i>Specimen preparation</i>	27
3.2.2. <i>Combustion analysis</i>	29
3.3. Results and discussion	31
3.4. Conclusions	35
4. Discontinuous precipitation in a Cu-4.5 at.% In alloy	37
Abstract	37
4.1. Introduction	39
4.2. Experimental details	40
4.3. Results and discussion	43
4.3.1. <i>Overall morphology</i>	43
4.3.2. <i>Early stages</i>	43

4.3.3. <i>Steady-state growth</i>	48
4.4. Conclusions	59
5. Grain-boundary phase transitions in the Al–Mg system and their influence on high-strain rate superplasticity	61
Abstract	61
5.1. Introduction	63
5.2. Experimental details.....	64
5.3. Results and discussion	65
5.4. Conclusions	70
6. Grain-boundary wetting by a solid phase: microstructural development in a Zn-5 wt.% Al alloy	71
Abstract	71
6.1. Introduction	73
6.2. Experimental details	77
6.3. Results and discussion	79
6.3.1. <i>As-cast microstructure</i>	79
6.3.2. <i>Morphology of the grain-boundary precipitation</i>	81
6.3.3. <i>Composition of the Al-rich and Zn-rich phases</i>	84
6.3.4. <i>Quantification of the solid-phase wetting</i>	84
6.3.5. <i>Growth kinetics of the Al-rich phase formed at the grain boundaries</i>	89
6.4. Final remark	91
6.5. Conclusions	91
7. Kurzfassung der Dissertation der deutscher Sprache	93
7.1. Einleitung	93
7.2. Korngrenzen- und Oberflächensegregation im System Cu– Bi	95
7.3. Löslichkeit von C in festem Cu	97
7.4. Diskontinuierliche Ausscheidung in einer Cu-4,5 At.-% In-	

Legierung	98
7.5. Korngrenzenphasenumwandlungen im System Al–Mg und ihr Einfluss auf die Superplastizität	100
7.6. Benetzung durch eine feste Phase: Gefügeentwicklung in einer Zn-5 Gew.-% Al-Legierung	102
7.7. Zusammenfassung und Ausblick	106
References	109
Danksagung	117
Curriculum vitae	119

1. Introduction

1.1. General remarks

The fabrication of metallic materials has long been recognized as of crucial importance to mankind: even periods in the human history were named according to the capability of producing metals, like the Bronze Age or the Iron Age. It was only appreciated in the last century that the properties of a metallic material are not primarily determined by the overall chemical composition, but rather by the distribution of the chemical elements and the crystal defects, i.e. its microstructure. Nowadays, the major goal of modern materials science and engineering is the optimization or design of materials microstructure for low cost but best performance of a fabricated part under service conditions. A deep understanding of the thermodynamics and kinetics of phase transformations is required to be able to control and modify the microstructure [1].

To achieve this goal the understanding of phenomena occurring at interfaces in materials like grain boundaries (GBs) and free surfaces (FSs) is a prerequisite [2,3]. The importance of interfaces in materials is based on the inhomogeneity due to their very presence: the physical properties at or near interfaces can differ drastically from those of bulk material. For example, under certain conditions a normally ductile polycrystalline material like Cu, if doped with a very small amount of Bi, can become completely brittle upon segregation of Bi atoms at the GBs in Cu [4].

The main goal of the present thesis is to contribute to the understanding of interfacial phenomena occurring in very common metallic systems as alloys based on Cu, Al and Zn.

1.2. Scope and contents of this thesis

Heat treatments can be used to promote processes occurring at interfaces as those mentioned above and, thereby, change the properties of polycrystalline materials. Segregation at interfaces, discontinuous precipitation reaction and GB wetting can be mentioned as examples of these processes. The current thesis presents studies on these topics.

The phenomenon of solute-atom segregation consists of a local change in the composition at interfaces, FSs and GBs, in a solid. This process is schematically represented in Fig. 1.1a. The decrease in the Gibbs energy of a system resulting from the interaction of solute atoms with the strain field around GBs is the driving force for equilibrium segregation. An investigation about the GB and FS segregation of Bi in Cu bicrystals under identical conditions is presented in Chapter 2, i.e., same temperature, same impurity content of the matrix, same crystallographic orientation of the interfaces, and – last but not least important – same experimental conditions during the measurement. By means of a special method, Cu bicrystals containing deliberately made *internal* cavities at the interfaces were fabricated and subsequently doped with Bi. Therefore, the high partial vapour pressure of Bi did not disturb the equilibrium segregation at the *internal* free surfaces, upon annealing of the samples at temperatures between 1073 and 1223 K. The annealed Cu bicrystals doped with Bi were fractured along the GBs in an ultra-high vacuum chamber for Auger electron spectroscopy. For the first time, equilibrium conditions for segregation of Bi at FSs in Cu were assured and this segregation was detected experimentally. From the comparison between the Auger spectra, it was concluded that the segregation level at FSs was higher than that at GBs.

During the investigation of the segregation of Bi at interfaces in Cu, an unexpected occurrence of a C signal was detected in the Auger measure-

ments. Since the moulds employed for the growth of the Cu single crystals – used for the fabrication of the bicrystals – were made from graphite, a possible dissolution of C was considered as the source of the C detected. According to the literature, the data available about the solubility of C in solid Cu are contradicting. Therefore, a particular investigation was undertaken (Chapter 3). This work provides, for the first time, reliable data on the solubility of C in solid Cu in the temperature range 1143 – 1293 K. Layers of C were vapour deposited onto high-purity Cu slices, which were annealed for 72 and 240 h at different temperatures. The C content in the samples was determined by means of a very precise combustion analysis. The equilibrium values determined are 50 times (!) smaller than the data reported before and as included in the most recent assessment of the equilibrium phase diagram. A Henrian behaviour for the carbon activity in the interstitial solid solution was observed.

The discontinuous precipitation reaction as another example of process control by interface properties is presented in Chapter 4. This reaction concerns the formation of a solute-depleted phase and a precipitate phase as a usually lamellar microstructure behind a moving GB, the so-called reaction front (Fig. 1.1b). In this reaction the crystal structure of the solute-depleted phase remains the same as the parent phase. A discontinuous change in both the crystal orientation and the solute concentration of the parent phase across the moving interface characterizes this kind of reaction. From a practical point of view, discontinuous precipitation reactions can have a deleterious effect on alloyed parts. Therefore, the understanding of their reaction kinetics can be helpful to prevent failures.

An extensive study on the morphology and kinetics of the discontinuous precipitation reaction in a Cu-4.5 at.% In alloy was performed by means of analytical transmission electron microscopy. GB movement was observed experimentally before the precipitation reaction started at this GB. Subsequent proceeding of the discontinuous precipitation reaction led

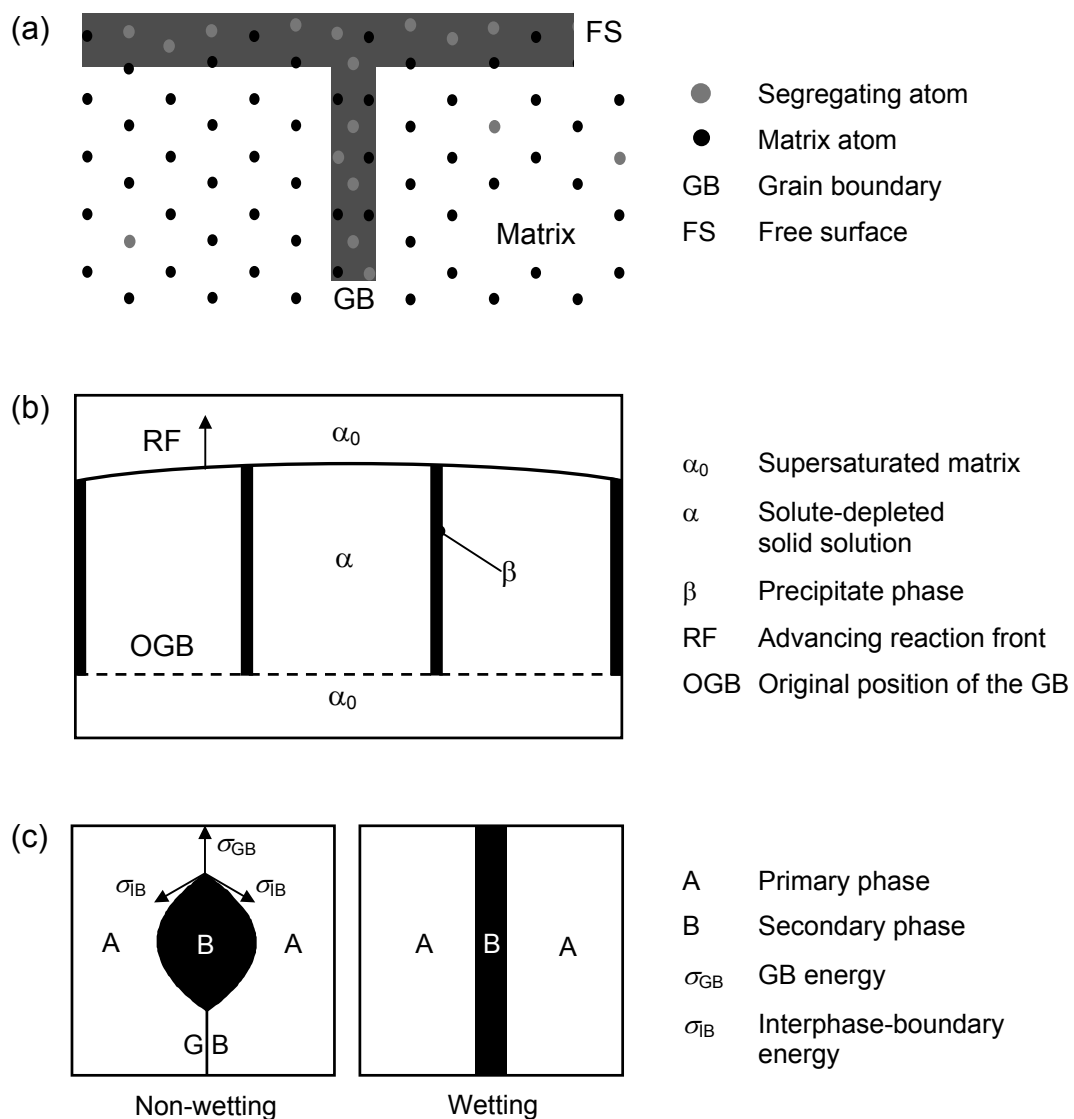


Fig. 1.1. Schematic representation of interfacial segregation at a grain boundary (GB) and at a free surface (FS) (a), discontinuous precipitation (b) and GB wetting (c).

to the formation of an ($\alpha + \delta(\text{Cu}_7\text{In}_3)$) lamellar two-phase microstructure, where α represents the In-depleted solid solution and δ denotes the precipitate phase. By application of energy-dispersive X-ray microanalysis, a solute depletion in the α lamellae in the wake of the advancing reaction front was observed. Indium concentration profiles were determined parallel

to the moving reaction front for individual α lamellae. The concentration profiles fall into two categories, namely, symmetrical ones and asymmetrical ones with respect to the central axis of the α lamella. These phenomena were attributed to a regular morphology and to an irregular morphology of the discontinuous precipitates, respectively. Local analysis of the kinetics of the discontinuous precipitation reaction was performed. Local grain-boundary diffusivity values for moving GBs were thus determined. In contrast with earlier interpretations in previous investigations, claiming that the diffusivities of moving GBs are much larger than of stationary GBs, this work demonstrates unequivocally that diffusivity data for moving and stationary GBs are of the same order of magnitude.

Studies on GB wetting in Al–Mg and Zn–Al alloys are presented in Chapters 5 and 6. GB wetting consists basically of replacing an existing GB by a layer of a second phase and thereby reducing the overall interfacial energy. At a relatively low temperature a chain of isolated second-phase particles occurs at the GB. Upon crossing the wetting temperature the GB will be fully covered by a wetting layer of the second phase (Fig. 1.1c). The effect of wetting layers can be detrimental (e.g. enhanced brittleness) or beneficial (e.g. improved plasticity). Conventional GB wetting by a *liquid* phase was studied, for the first time, in Al–Mg polycrystals (Mg contents of 5, 10, 15 and 20 wt.%). Samples of these alloys were annealed at temperatures between 763 and 903 K. It was observed that above 871 K all GBs in the solid Al-rich phase were wetted by a liquid phase. Below 813 K no GBs wetted by a liquid phase were observed. The maximal and minimal temperatures of GB wetting, T_{wmax} and T_{wmin} , were determined. Between 813 and 871 K the percentage of the wetted GBs gradually increases from 0 to 100 %. The correspondent tie-lines were constructed in the bulk Al–Mg phase diagram. The observation of GB wetting in the Al–Mg system provides an explanation for the mechanical behaviour of Al–Mg alloys. The experimental T_{wmax} and T_{wmin} data allow to

estimate the position of the *GB solidus line* in the phase diagram. On this basis, the occurrence of prewetting (or premelting) in the one-phase region of the phase diagram was suggested as the reason for the high-strain high-rate superplasticity observed in Al–Mg alloys in a narrow temperature range just below the bulk solidus line.

Inspection of the scientific basis for GB wetting by a liquid phase leads to the suggestion that “wetting” by a second solid phase may be possible, too. Until now no work about GB wetting by a *solid* phase was reported. In this work a systematic study of solid wetting has been performed, for the first time (Chapter 6). The microstructural development of Zn-5 wt.% Al polycrystals produced upon annealing in the temperature range 523–648 K was studied. The Al-rich phase formed either chains of separated lens-like precipitates or continuous layers at the Zn-rich phase/Zn-rich phase GBs upon annealing at different temperatures. The contact angle at the intersection between the Al-rich phase/Zn-rich phase interphase boundaries and the Zn-rich phase/Zn-rich phase GB decreased with increasing temperature. It became zero at a certain temperature, and remained zero above this solid-state wetting temperature, i.e., a continuous Al-rich phase layer covered the Zn-rich phase/Zn-rich phase GBs. The fraction of wetted GBs increased with increasing temperature and was independent of annealing time. The growth of the Al-rich phase at the GBs is controlled by volume diffusion in the matrix phase.

2. Grain-boundary and surface segregation in the Cu–Bi system

G.A. López, W. Gust and E.J. Mittemeijer

Abstract

Grain boundary and surface segregation of Bi in Cu were investigated under identical conditions. Cu bicrystals containing deliberately made internal cavities at the interfaces were doped with Bi, annealed at different temperatures, and broken in an Auger microprobe. The segregation level at the free surfaces was found to be higher than that at grain boundaries.

2.1. Introduction

Many important properties of materials are strongly influenced by the behaviour of the interfaces, such as grain boundaries (GBs) and free surfaces (FSs). Solute atoms can segregate to these planar defects to minimize the Gibbs energy of the system, and thereby affect the bulk properties of the material [4–6]. Segregation to FSs mainly influences properties like adhesion, wear and corrosion; GB segregation affects the GB diffusion and mobility, intergranular embrittlement, etc. [4,6]. A powerful technique applied to investigate segregation is Auger electron spectroscopy (AES) [7], due to its rapid identification of the segregants and very high depth resolution.

Surface segregation as well as grain-boundary segregation was investigated in many systems [4–6,8–11]. However, only in a few cases segregations of impurities at FSs and at GBs were systematically compared. Because the driving forces for solute segregation at GBs and for solute segregation at FSs are of similar nature [6], to find out the correlation between both types of interface segregation can be a valuable method to predict the segregation at one of the interface types, once it has been determined for the other interface type. A detailed study of FS and GB segregation was performed for Fe–Sn alloys [12]. Segregation of impurities to both types of interfaces was investigated in Ni, in a Ni–In alloy as well as in Ni₃Al [13–17]. It appears that segregation at FSs is stronger than at GBs [6]. However, in some cases the segregation level is similar for FSs and GBs [14] and, moreover, there are systems where the segregation of elements with low solubility at GBs is stronger than that at FSs (B in Ni₃Al [18]). Cosegregation of impurities can lead to more pronounced differences between FS and GB segregation, as has been observed in an Fe-6 at.% Si alloy [19]. Further, it was proposed that solute elements that cause intergranular embrittlement, will segregate stronger to FSs than to GBs,

whereas the opposite is expected for species that improve the ductility [20–22], which proposal was confirmed experimentally [15,18]. At the moment a satisfactory, fundamental understanding of the correlation between segregation at FSs and at GBs lacks. Here, experimental data on surface and grain-boundary segregation of Bi in Cu are presented, in order to contribute to this understanding.

GB segregation for the Cu–Bi system was investigated extensively by means of different techniques. Already in 1971 GB segregation of Bi in Cu was exhibited by AES [23]. Equilibrium segregation is segregation at a temperature and composition pertaining to a one-phase region of the equilibrium phase diagram. For this reason, it is required to know accurately the solubility limit of Bi in Cu. Recently the Cu–Bi equilibrium phase diagram was determined with high precision [24]. On this basis an exhaustive study was made of segregation of Bi at GBs in polycrystalline Cu [25,26]. The correlation between GB segregation, faceting and embrittlement in Bi-doped Cu was investigated using analytical electron microscopy [27].

In contrast with the GB segregation described above, surface segregation of Bi in Cu–Bi alloys has been investigated only superficially because of the experimental difficulty posed by the high partial vapour pressure of Bi. Only one work has been dedicated specifically to Bi surface segregation in Cu [28] and further some side results on surface segregation were reported in Refs. [29,30]. Furthermore, according to the equilibrium phase diagram [24], the results presented in these three studies (i.e.[28–30]) were obtained for Bi bulk concentrations above the solubility limit for the range of temperatures concerned, and hence cannot be attributed to a state of equilibrium for surface segregation.

Against the background presented above, a systematic investigation of segregation of Bi at both FSs and GBs in Cu, under identical conditions, is desired. The first results of such a study are presented here. To avoid the

problem of Bi evaporation upon Bi segregation at FSs a special method for sample preparation was applied. The selected misorientation of the Cu bicrystal employed corresponds to a $\Sigma = 19a \{331\}$ symmetrical tilt GB (where Σ denotes the reciprocal density of common lattice sites of the adjoining crystals). This misorientation was selected because, according to the theoretical data for the GB energy given in Ref. [31], the selected GB has a relatively high energy and, therefore, a strong segregation can be expected at this GB [6,32].

2.2. Experimental details

2.2.1. *Specimen preparation*

A special method was applied to produce Cu bicrystals with symmetrical tilt GBs and internal FSs. This technique was used before in a study of segregation in the Ni–In system [13]; here it will be described only briefly. Oriented Cu slices of 4 mm thickness and about 10 mm diameter were cut from cylindrical single crystals grown by the Bridgman technique. The starting material was 99.999 wt.% Cu. The orientation of the crystals was determined by Laue back-reflection patterns. It was taken care that the flat faces of the samples were perpendicular to the desired GB normal. Then, the single crystal slices were prepared by ultramilling using diamond cutters in order to obtain microscopically smooth and plane surfaces. Next, a regular pattern of cavities was made in one of the two bonding surfaces by a combination of a photolithographic process and chemical etching. The surface thus obtained is shown in Fig. 2.1a. After diffusion bonding these cavities provide a pattern of free *internal* surfaces. The cavity depth was approximately 12 μm . To counteract impurities to be incorporated during the preparation process, the single crystalline halves were cleaned ultrasonically in acetone before diffusion bonding.

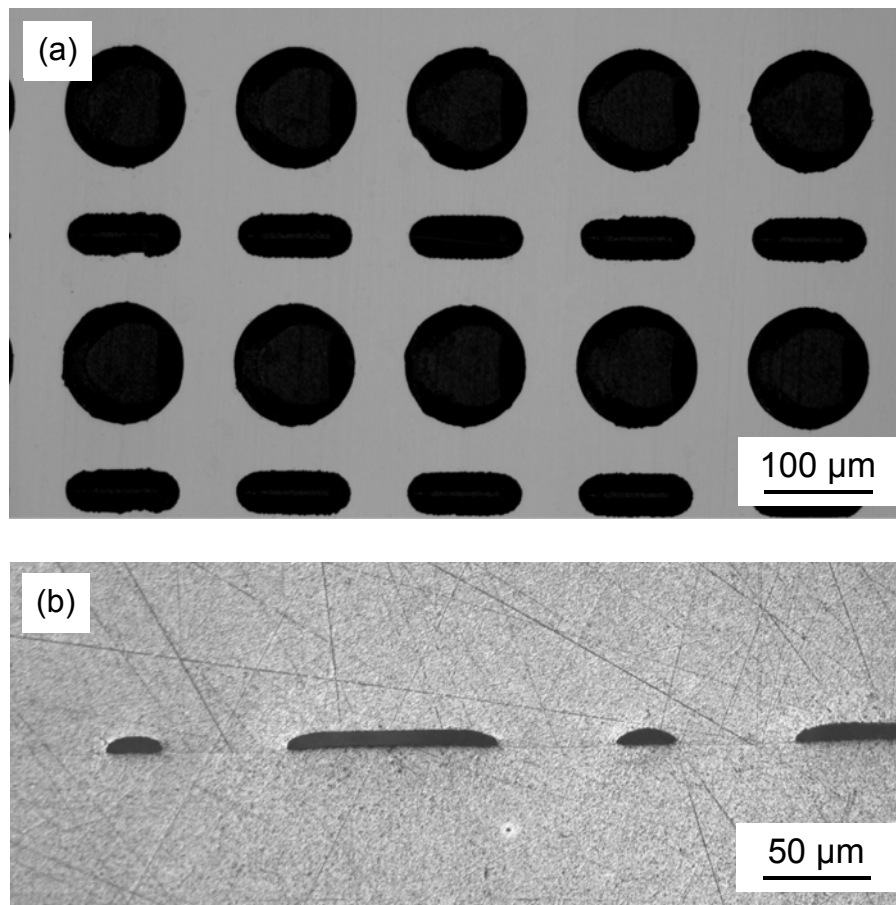


Fig. 2.1. Light optical micrograph of the surface of a Cu single crystal after ultramilling, photolithography and chemical etching (a), and cross-section of a $\{331\}$ symmetrical tilt GB with internal cavities produced by photolithography on the GB face of one of the crystals (b). Cavity depth $\approx 12 \mu\text{m}$; cavity diameter $\approx 100 \mu\text{m}$.

To produce a symmetrical bicrystal, the two surfaces (one with and the other without cavities) were placed face-to-face and rotated 180° one with respect to each other, around the GB normal. Appropriate marks put on the initial specimens allowed an accuracy of about $\pm 1^\circ$ for this rotation. The resulting assembly was fixed between two boron nitride discs in a cylindrical tantalum holder by means of a central screw. The diffusion bonding was carried out in a molybdenum resistance furnace installed inside a turbomolecular pumped vacuum container. The pressure in the system

during diffusion bonding was typically about 6×10^{-5} Pa. The bicrystals were diffusion bonded for 15 h at 1286 K. A cross-section of such a bicrystal showing the symmetrical tilt GB ($\{331\}$ boundary plane; $\langle 011 \rangle$ tilt axis with a tilt angle of 26.5°) with *internal* cavities as produced by this method is presented in Fig. 2.1b.

From each bicrystal up to 6 identically oriented specimens (3 mm x 3 mm x 8 mm) were cut by spark erosion. After cleaning (etching with diluted HNO_3 for several seconds), the samples were doped with Bi. To this end, 2 to 4 samples were encapsulated in evacuated silica tubes (pressure $\approx 10^{-4}$ Pa) together with a Cu - 1 at.% Bi polycrystal, which acts as a Bi-atoms source. Then the ampoules were heat-treated at 1153 K for 22 h, in order that Bi atoms evaporate from the polycrystal and diffuse into the Cu bicrystals. Subsequently, the samples were water quenched, encapsulated again and homogenized in vacuum for 240 h at 1223 K.

A test single crystal of analogous dimensions was also included in the ampoules. After homogenisation, chemical analysis performed by atomic absorption spectroscopy on the test samples indicated a Bi content in the bulk material between 35 and 51 ± 2 at.ppm. The carbon content, as determined by combustion analysis, was 14 ± 4 at.ppm.

Now, the samples were ready to be heat-treated to bring about equilibrium segregation at the GB and at the internal FSs. Several samples were encapsulated again and annealed in the one-phase region of the equilibrium phase diagram [24] at temperatures between 1073 and 1173 K. The annealing time to establish equilibrium segregation was estimated using an existing model for segregation kinetics at GBs and FSs [33]. In the model, volume diffusion from semi-infinitely large adjacent crystals, with a certain bulk concentration of the segregant, to the interface (GB) is considered. The ratio of the interface concentration to the bulk concentration is assumed to be constant. In our case, the annealing times for every tem-

perature were taken at least 5 times longer than those calculated according to the model description, in order to assure segregation levels representative of equilibrium. The sample after homogenisation is taken as representing the equilibrium segregation at 1223 K. The details of the annealing conditions for investigating equilibrium segregation have been listed in Table 2.1.

Table 2.1. Annealing conditions to establish equilibrium segregation for samples with a Bi bulk content of approximately 50 at.ppm.

T (K)	Annealing time (h)	
	$t_{0.9}^*$	This work
1073	5.1	26
1123	2.1	12
1173	0.9	6
1223	0.4	–

* $t_{0.9} = 7.5 s^2 \delta^2 / D$. $t_{0.9}$ is the time for the segregating component to reach 90 % of the equilibrium segregation level at the GB. Here, s is the segregation factor given as the ratio between the GB concentration and the bulk concentration of the segregating element, δ is the GB thickness, and D is the bulk diffusivity [33].

2.2.2. Auger electron spectroscopy (AES)

The annealed Bi-doped Cu bicrystals were broken *in situ* at room temperature in the fracturing device of a JEOL JAMP-7830F high-performance Auger microprobe, equipped with a field emission electron gun and a hemispherical analyser. A notch at the GB along the perimeter of the sample had been made by means of a diamond saw to promote breaking along the GB. After fracture AES spectra were measured at several locations on the fracture surfaces (GBs) as well as on the bottom of the artificial cavities (FSs; cf. Fig. 2.1a). For each sample 15 spectra were obtained for each type of interfaces (GBs and FSs). The pressure in the ultra-high vac-

uum chamber was always lower than 8×10^{-8} Pa. Additionally, Auger-sputtered depth profiles were also recorded on both kinds of interfaces using the discontinuous ion-sputtering mode. The sputter rate for the experimental conditions was 6 nm/min as recorded for SiO₂. The peak-to-peak heights of the Bi (105 eV), Cu (910 eV), Cu (66 eV), and C (275 eV) Auger signals were used to construct the depth profiles. When upon continued sputtering no further changes in the peak intensities were detected, the sputtering was stopped.

2.3. Results and discussion

All the samples investigated broke intergranularly in the fracturing device of the AES microprobe. A typical bicrystal fracture surface is shown in Fig. 2.2: an artificially created FS surrounded by GB regions can be seen (cf. Fig. 2.1b). After breaking the samples, it was easy to find planar areas at the GBs and FSs, where, subsequently, the AES spectra were acquired. The observed small deviations from a fully planar interface may have been caused by strain-induced GB migration during diffusion bonding and facetting [13,27]; note that the walls of the initially circular cavities have become faceted upon annealing. At the bottom of the cavities some dark regions are visible. According to AES spectra recorded from these locations, the dark regions are due to some contamination by carbon. The results presented here have been obtained from carbon-free areas.

Representative Auger spectra obtained from both types of interfaces are shown in Fig. 2.3. The very small amount of Bi in the bulk material (maximally 51 at.ppm, cf. Section 2.2.1.) is far below the detection limit of the Auger measurement. Therefore, the strong peak of Bi in Fig. 2.3a indicates distinct segregation of Bi to FSs. Even although the occurrence of Bi is hardly detectable in Fig. 2.3b (segregation at GBs), Bi must have been

present at the GB otherwise the Cu bicrystal would not have been broken in a brittle way intergranularly. Comparing the Bi peaks, with respect to the low-energy Cu peaks in the same spectra in Fig. 2.3a and b, it follows that the amount of Bi segregated at FSs is much larger than that segregated at the GBs. For symmetrical GBs the segregant concentrations are approximately the same on both surfaces generated after breaking in the vacuum chamber [5,34]. Thus, the total Bi content segregated at GBs is considered to be twice the quantity determined by AES. Even taking into account this effect, the obtained results (Fig. 2.3) still show clearly that Bi segregation to FSs of Cu is considerably stronger than that to GBs for the studied range of temperatures and Bi bulk compositions.

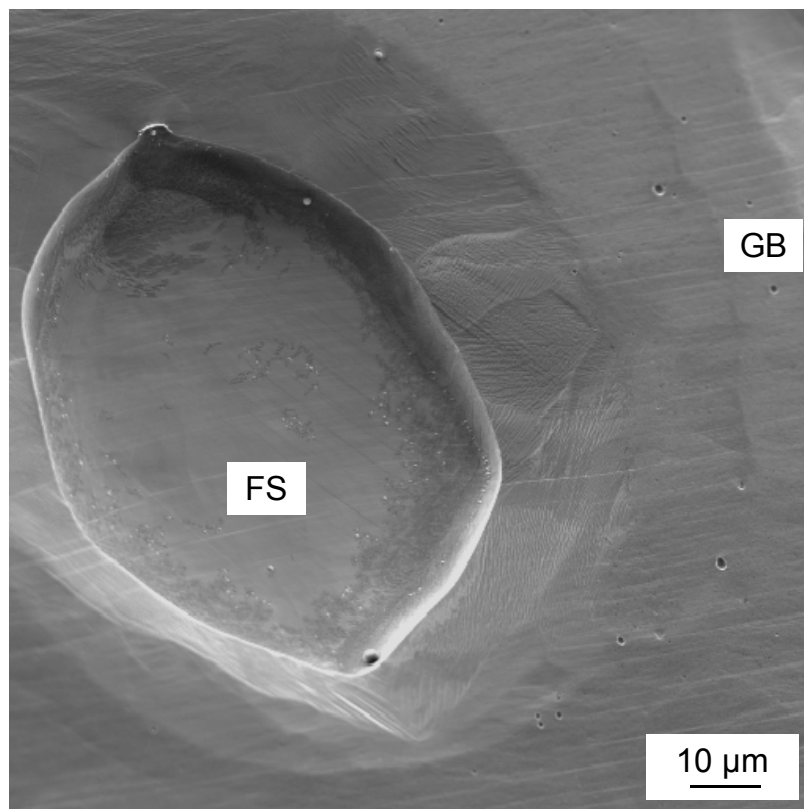


Fig. 2.2. Secondary-electron micrograph of the fracture surface of a sample broken *in situ* in the ultra-high vacuum chamber. Specimen annealed for 6 h at 1173 K; Bi bulk content = 51 ± 2 at.ppm.

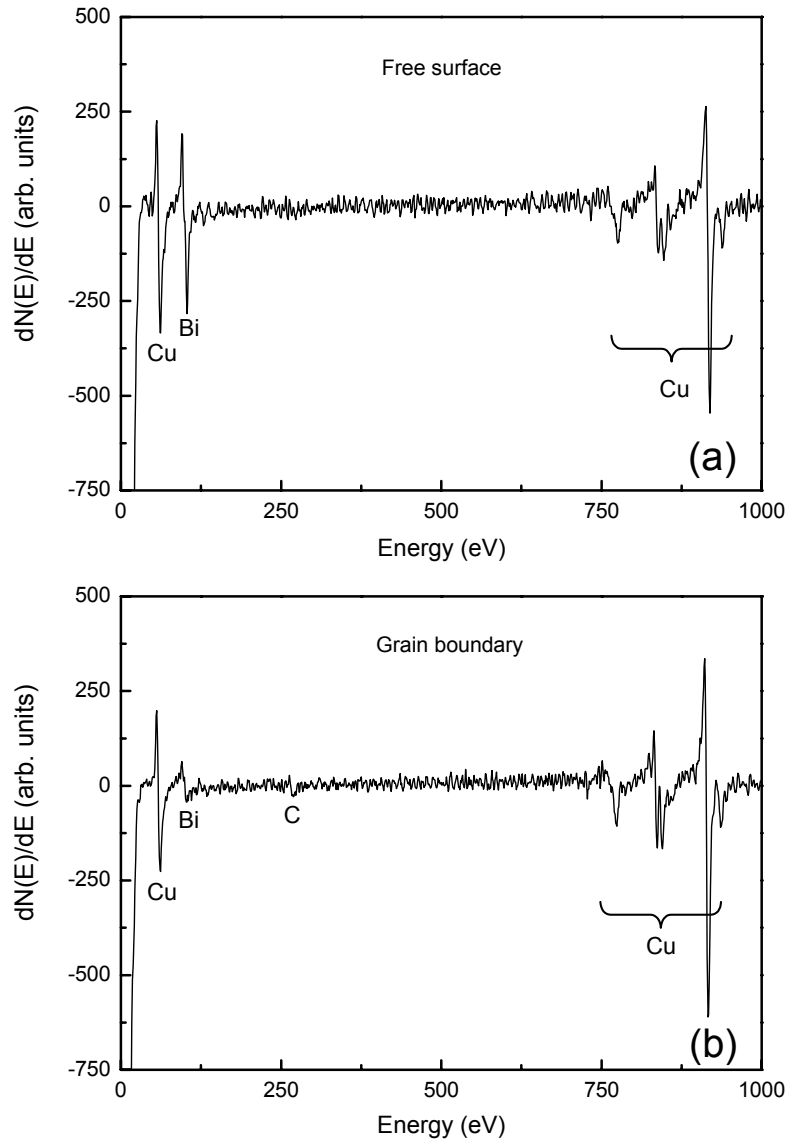


Fig. 2.3. AES spectra (differentiated) recorded from the free surface (cf. a cavity) (a) and from the grain boundary (b) of a sample annealed for 6 h at 1173 K. Bi bulk content = 51 ± 2 at.ppm.

Auger sputter depth profiles as obtained starting from initial FS and GB areas are shown in Fig. 2.4. The presence of Bi is confined to a small region (“segregation layer”) adjacent to the FS and GB. The Bi-rich zone is thinner in case of the GB, again indicating a stronger segregation at the FS than at the GB. This well corresponds with a larger change in the low-

energy Cu peak intensity in the case of the sputter depth profiling at the FS area. Adopting a sputter rate of 6 nm/min (cf. Section 2.2.2.), the segregation layer at the FS has an extent of approximately 1.8 nm. From the Auger spectra acquired at the FSs and GBs of several samples annealed at temperatures from 1073 to 1223 K, it follows that the higher the temperature, the smaller the Bi segregation level to interfaces in Cu. This is consistent with the classical segregation behaviour for dilute alloys according to Ref. [33] (see also [25,35]).

A Bi doping and heat treatment procedure similar to the present one was performed in Refs. [24–26] in a study of segregation of Bi at GBs in polycrystalline Cu. It was asserted in Ref. [36] that, using this method, upon annealing the Bi concentration at the GBs reported in Refs. [24–26] would increase until a maximum value and then would decrease due to Bi evaporation in the evacuated ampoule, and thereby segregation according to equilibrium conditions would not occur for the annealing times applied. Whether this is true or not, such a problem cannot occur with the present work because the small volume of the cavities at the GB and the very long annealing time assure that equilibrium with Bi gas in the cavity must have been attained during annealing.

A further remark is needed regarding the possible contribution of Bi atoms condensed from the vapour during quenching on the detected level of segregation at the FSs. Using the equilibrium Bi vapour pressure and applying the ideal gas equation, the number of Bi atoms present in a cavity at a certain temperature can be estimated. Supposing that upon quenching all these Bi atoms are condensed uniformly on the free surface of the cavity, and taking into account that a monolayer of Bi contains 9.3 at/nm^2 , which is the volume of a Bi atom in solid Bi to the power $2/3$, the enhancement of the Bi content at the FSs caused by such condensation is less than 10^{-3} monolayer, which Bi contribution is negligible. Also, according to careful estimations, the effect of non-equilibrium segregation upon

quenching on the segregation levels is not significant. Note that the experimental error for segregation levels is of the order of 20 % [22].

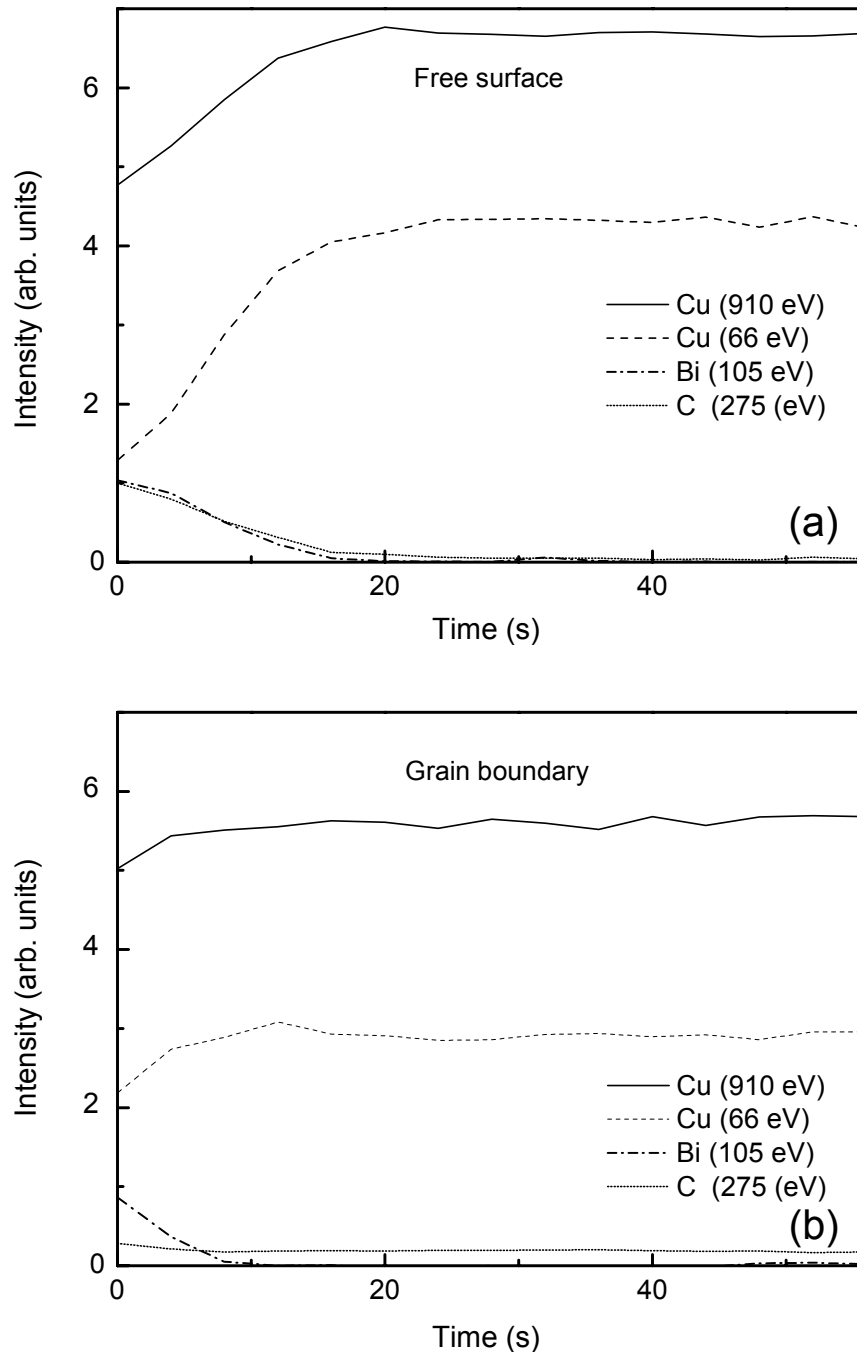


Fig. 2.4. AES sputter depth profiles obtained from regions corresponding to initially the free surface (a) and the grain boundary (b) of a sample annealed for 12 h at 1123 K. Bi bulk content = 51 ± 2 at.ppm.

It was predicted [20–22] that elements which cause intergranular embrittlement (like Bi in Cu) will segregate stronger to FSs than to GBs, whereas the opposite should be true for species that improve intergranular cohesion. Elements with a lower sublimation enthalpy and a larger atomic size with respect to the matrix element will segregate stronger at FSs than at GBs. The effect of B in the enhancement of the ductility of Ni₃Al is well known. In agreement with the theory [20–22] B segregates in this material strongly at GBs and weakly, if at all, at FSs [18]. On the other hand, a similar In segregation level to both types of interfaces was reported [14], although the sublimation enthalpy of In is smaller than that of Ni and the atomic size of In is larger than that of Ni. It was concluded in Ref. [14] that the prediction based on the sublimation enthalpies and atomic sizes given in Ref. [20] can be misleading. In the present case, the sublimation enthalpy of Bi is smaller than the sublimation enthalpy of Cu, and Bi has a considerably larger atomic size than Cu. Therefore, Bi should segregate stronger at FSs than at GBs, in qualitative agreement with the results obtained in the present work.

The only work specifically devoted to Bi surface segregation in Cu until now is Ref. [28]. However, in this work Bi segregation has been studied in ranges of temperature and Bi content where no Bi solubility in Cu is possible according to the equilibrium phase diagram [24]. Therefore, it appears that the data in Ref. [28] refer to Bi precipitation at FSs rather than to Bi segregation. Furthermore, it is not clear how in the work discussed the problem of Bi evaporation during the annealing (see above) was circumvented. In two other studies [29,30] no differences between segregation at FSs and at GBs was observed (1.2 –1.4 monolayers; at temperatures between 673 and 773 K). However, these data have been obtained from specimens with a composition in the two-phase region of the Cu–Bi phase diagram [24], because the reported Bi bulk contents (60 and 42 at.ppm,

respectively) are higher than the solubility limit at the temperatures applied.

Only in the present work, all samples were annealed in the single-phase region and it was assured that no significant Bi evaporation from the FSs could occur, so that equilibrium segregation of Bi to FSs in Cu could be detected, for the first time.

2.4. Conclusions

By means of a special method to produce Cu bicrystals, containing a grain boundary with cavities at the grain-boundary face, the segregation of Bi in Cu simultaneously at the grain boundary and at the free surface (of the cavities) was investigated under identical experimental conditions, i.e. as the result of a single annealing experiment. For the first time, surface segregation of Bi in Cu was determined experimentally applying Auger electron spectroscopy to a bicrystal fractured along the grain boundary. In the ranges of temperature and Bi bulk composition studied in this work the segregation at the free surface was stronger than the segregation at the grain boundary.

3. The solubility of C in solid Cu

G.A. López and E.J. Mittemeijer

Abstract

The solubility of C in solid Cu was determined in the temperature range 1143 – 1293 K. Layers of C were vapour deposited onto high-purity Cu slices, which were annealed for 72 and 240 h at different temperatures. The C content in the samples was determined by means of combustion analysis. A Henrian behaviour for the carbon activity in the interstitial solid solution was observed.

3.1. Introduction

The solubility of C in solid Cu is very small as has been well recognized since a long time. However, the value of this solubility is not well known. According to the newest assessment of the Cu–C equilibrium phase diagram [37] the smoothed solubility values reported in Ref. [38] should be regarded as of tentative, preliminary nature. Precise knowledge of the solubility of C is of great practical importance. For example, if even only minute amounts of C are dissolved during the production of high-purity noble metals exhibiting very small carbon solubilities, as a consequence of using graphite moulds, carbon-oxide gases could be formed when such metals are cast under oxidizing conditions. This could cause gas porosity in e.g. copper-base casting products.

For high-temperature applications matrix-embedded C fibres provide stiffness and prevent failure [39]. The stability of such Cu matrix composites was investigated to check the possibility of replacing electronic contacts of Ag by Cu [40]. In the case of the Cu–C system, the very low mutual solubility and the extremely poor wetting of the C fibres by Cu make the production of such graphite composites difficult. Knowledge of the amount of C which can be dissolved in Cu, upon inward diffusion from the Cu/C interface and thereby establish the desired diffusion bonding, is of cardinal importance for the fabrication and performance of these composites.

The available data on the Cu–C equilibrium phase diagram were summarized in Ref. [37]; no carbide phases were reported. The solubility of C in liquid Cu was extensively studied [41,42]. In contrast with the agreement observed between the data reported by different authors for the solubility of C in liquid Cu for a wide range of high temperatures (1673 – 2123 K), the data published on solubility of C in solid Cu are contradicting [38,43]. In the first investigation [38], the equilibrium solubility of C in solid Cu was

measured between 1058 and 1314 K by a vapour transport technique. Foils of Cu were equilibrated with graphite in presence of a small amount of air. The introduction of C into Cu occurred through vapour transport in the (CO + CO₂) gas atmosphere in contact with the Cu foil. The determination of the C content in Cu was performed by combustion analysis. The solubility data obtained near the melting point of Cu, indicating more than 250 at.ppm at 1273 K, are two orders of magnitude higher than the solubility of C in liquid Cu. The data as reviewed in Ref. [37] are shown in Fig. 3.1. Later, it was speculated that these solubility values were too high, which could have been caused by adsorbed C, CO and CO₂, or trapped intergranular C [42]. For this reason, these solubility data are regarded as tentative in Ref. [37]. In contrast with Ref. [38], it followed from other research that the solubility of C in solid Cu is smaller than 0.5 at.ppm at 1173 K, as determined by using a radiochemical technique [43]. In this investigation, the Cu specimens had been saturated with C by holding the Cu specimens at 1173 K for 20 days in the presence of a millicurie of ethylene or glucose, both marked with C¹⁴. These data were not incorporated in the newest assessment of the Cu–C equilibrium phase diagram [37].

In the past, combustion analysis has been employed successfully for the determination of very low C contents (≥ 1 wt.ppm) in metals, especially in low-carbon steels. Nowadays, metals with extremely low C contents are applied in technological applications, especially in electric and electronic applications. In order to reach high accuracy in the C content determination, a modified combustion method has been developed at the end of the eighties and subsequently improved [44,45]. Thus, paying special attention to reducing the influence of systematic errors inherent to the commonly applied combustion method, a detection limit of 0.5 wt.ppm has been attained. Modern CO₂-gas detectors, mostly high-sensitive infrared cells with a low level of electronic noise, are now available in carbon analysers.

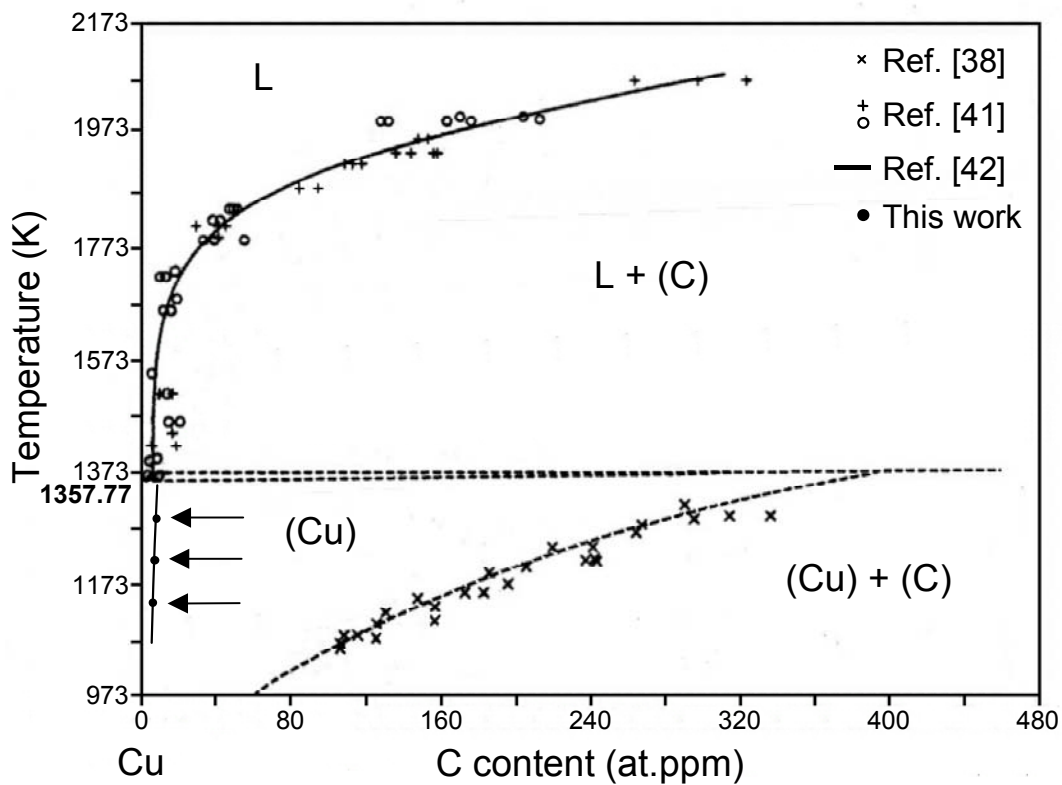


Fig. 3.1. Cu–C equilibrium phase diagram at the Cu-rich side according to Ref. [37]; L = liquid. The new data for the solubility of C in solid Cu are shown for comparison.

Against the background presented above, in this work a precise determination of the solubility of C in solid Cu has been performed. The high precision combustion technique as developed in Refs. [44,45] was employed to determine the C content in the annealed Cu samples.

3.2. Experimental details

3.2.1. *Specimen preparation*

Cylindrical slices of very pure Cu (99.9998 wt.%) with a diameter of 12 mm and a thickness of 4 mm were ground using 1200 grit SiC paper. A layer of

400 nm of graphite (EK 506 high purity, Ringsdorff-Werke, Germany) was deposited onto the surface of the Cu specimens by physical vapour deposition. In this way, intimate contact was assured between Cu and C. Before vapour deposition of C, the Cu samples were cleaned ultrasonically in acetone for 15 min and subsequently were dried by blowing with a CO₂-snow jet. The pressure in the deposition chamber was 1×10^{-4} Pa before sputter cleaning. The target was then sputter-cleaned with Ar⁺ ions for 15 min under a pressure of 7×10^{-1} Pa and a power of 100 W (direct current), thereby eliminating a possible oxide layer on the Cu surface. Then the physical vapour deposition of C onto the Cu slice was performed at room temperature under an argon pressure of 7×10^{-1} Pa and a power of 100 W for 90 min. With respect to the mass of the Cu slice substrate, the amount of C deposited was more than enough to attain the large value of saturation solubility reported in Ref. [38].

Several C-layered Cu samples were encapsulated in glass ampoules under a final vacuum of 5×10^{-7} Pa at room temperature. The ampoules were turbo-pumped for 12 h before closing to reach this vacuum. Subsequently, the ampoules were annealed at three different temperatures: 1143, 1223 and 1293 K, for 72 and 240 h. For these times it is expected that the equilibrium solubility of C in Cu has been reached throughout the slice. The annealing temperature was maintained constant with an accuracy of ± 1 K. After the annealing the samples were quenched by crushing the ampoules in water. After water quenching a dark layer, sometimes partly coloured layer, could be observed on the surface of the samples. This indicated an excess of the carbon (graphite) deposited and a possible oxide layer formed upon contact with water during quenching.

3.2.2. Combustion analysis

The combustion technique consists of burning a sample of material in a flowing stream of oxygen. The CO₂ produced as a result of the combustion of the C present in the sample is taken up into the flowing oxygen. Then the absorption of infrared radiation by this CO₂ is detected in a cell and used for the quantification.

For the determination by this technique of the extremely low C content in metals as Cu much care is required. Typical systematic errors, inherent to the commonly applied combustion method, are an increase in the measured value due to carbonaceous contamination on the surface of the samples and auxiliary materials (crucibles, combustion accelerator, etc.) and an insufficient detection limit of the CO₂ detector due to a low ratio of the signal belonging to the sample and the background signal. The background signal, which is quantified through measurement of a blank value, is produced by the unavoidable contamination of the materials used during the analysis and by the electronic noise. The blank value should be as small as possible (for more details see Refs. [44,45]).

The dark layer observed on the surface of the samples after quenching was completely removed by means of grinding and chemical etching (a solution of equal volume parts of 65 wt.% nitric acid, glacial acetic acid and 85 wt.% phosphoric acid at room temperature) until metallic brightness was observed. Thereafter, the Cu slice of mass of approximately 4 g was cut in small pieces; amounts of about 1 g were used in the combustion analysis. For every sample 4 determinations were done; the average results obtained are reported here.

For every set of measurements the crucibles used in the combustion analysis were degassed in a muffle furnace at 1273 K. Their residual contamination produces an unsatisfactory reproducibility of the recorded

background signal. Therefore, a pre-burning of very pure Cu chips (LECO Metal Accelerator 501-263; 0.5 to 1 mm), which had been annealed at 1073 K for at least 5 h and then cooled under an Ar flow, was performed in the crucible concerned before the sample itself is combusted. In this way, a good reproducibility of the recorded background signal was achieved and the determined blank value is reduced. After this pre-burning and with the crucible still hot (at about 473 K) a weighed mass of the sample, which was freshly etched, together with 1 g of annealed Cu chips were combusted. The charging in the hot crucible avoided surface adsorption of carbonaceous contaminations. The added Cu chips acted as a combustion accelerator, which guaranteed complete sample combustion [44,45].

For every measurement the blank value of the accelerator/crucible system was determined upon burning only annealed pure Cu chips. This blank value was subtracted from the total C amount measured in the respective determination. The resulting C amount is then referred to the mass of the Cu sample, to determine the carbon bulk concentration. A calibration in the very-low-C content range was made using standard steel samples with a C content equal to 286 ± 9 wt.ppm (LECO Chemical Standard High Purity 501-501). For the calibration an amount of 30 mg of this standard sample was weighed with a microbalance (± 0.5 μg sensitivity) to make sure that the range of calibration corresponds well with the amounts of C to be determined (total carbon amounts in the range 0.1 – 2 μg). The determinations were performed employing an ELTRA CS 800 carbon/sulphur analyser equipped with a high-frequency induction furnace. The detection of the CO_2 produced in the combustion was done by means of an infrared CO_2 cell, specially designed for the determination of extremely low C contents.

3.3. Results and discussion

The results from the different determinations of the C content at various temperatures, as determined by means of combustion analysis, are presented in Table 3.1. In the case of the initial, pure Cu, besides the background signal corresponding to the blank value (cf. Fig. 3.2), no peak was observed. For this reason, it is considered that the C content in the initial Cu is in any case not higher than 1 at.ppm (= 0.2 wt.ppm = detection limit). After annealing the Cu/C samples at the three selected temperatures for 72 h and following the steps detailed above for the combustion analyses, a significant amount of CO₂ was detected in the infrared cell. An example is shown in Fig. 3.2 for the sample annealed at 1293 K for 72 h; the peak area corresponds to a C content of 7.4 ± 0.5 at.ppm (1.4 ± 0.1 wt.ppm).

Table 3.1. Carbon content as determined by combustion analysis; t = annealing time .

Sample	C content (at.ppm / wt.ppm)	
	$t = 72$ h	$t = 240$ h
Starting Cu	No peak observed	-
Cu/C annealed at 1293 K	$7.4 \pm 0.5 / 1.4 \pm 0.1$	$7.4 \pm 0.5 / 1.4 \pm 0.1$
Cu/C annealed at 1223 K	$6.3 \pm 0.5 / 1.2 \pm 0.1$	$5.3 \pm 0.5 / 1.0 \pm 0.1$
Cu/C annealed at 1143 K	$4.8 \pm 0.5 / 0.9 \pm 0.1$	$4.8 \pm 0.5 / 0.9 \pm 0.1$
Blank value	$0.2 \pm 0.1 \mu\text{g}$	$0.2 \pm 0.1 \mu\text{g}$

In order to confirm that the determined C-solubility values represent equilibrium values, the C content determinations were repeated for samples that were annealed for a longer period of time (240 h) under the same conditions. As follows from the results gathered in Table 3.1, the C contents as determined after 240 h of annealing agree very well with those

determined after 72 h of annealing. Therefore, it is concluded that equilibrium values for the solubilities were determined.

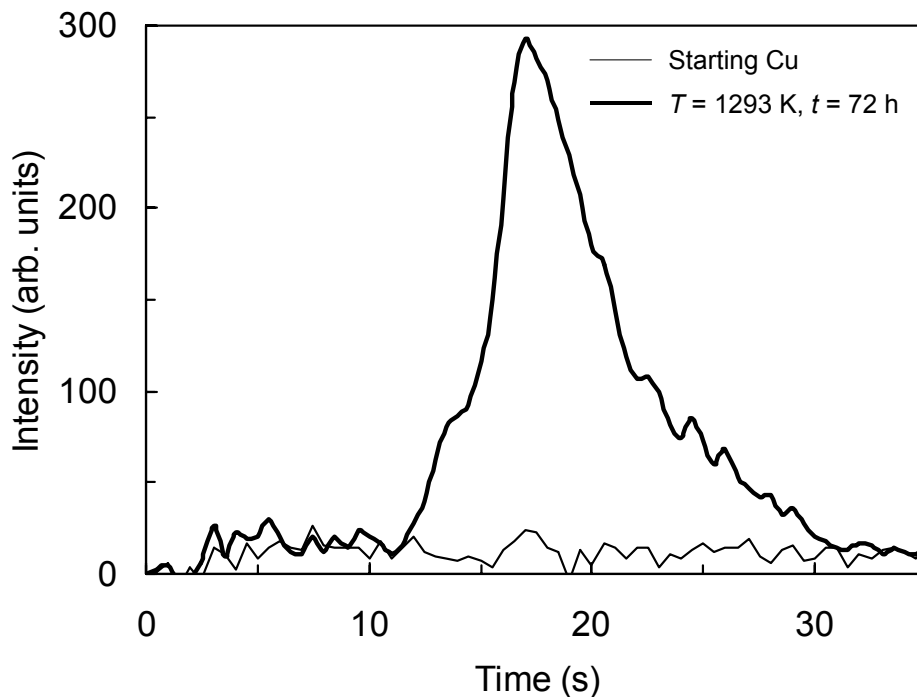


Fig. 3.2. Evolution of CO₂ in the combustion analyser from approximately 1 g of the starting, pure Cu and of a carbon-saturated sample after annealing at 1293 K for 72 h.

On average the blank value obtained in the measurements was 0.2 μg (absolute), with a maximal variation of $\pm 0.1 \mu\text{g}$. In this context, it should be noted that all Cu samples were very homogeneous and the scatter in the four determinations carried out at each temperature and each annealing time was only 0.16 at.ppm (0.03 wt.ppm) in the worst case.

The results presented in Table 3.1 have been indicated in the equilibrium diagram (see arrows in Fig. 3.1). For the temperature of 1223 K the average between the values obtained for the two different annealing times has been indicated. As can be seen in Fig. 3.1, the new solid solubility val-

ues are significantly smaller than the previous data reported in Ref. [38]. Further, it should be noted that a significant C solid solubility has been determined here, which refutes the statement in Ref. [43] that the solubility of C in solid Cu would be smaller than 0.5 at.ppm (0.1 wt.ppm).

As already noted in Ref. [42], adsorbed C, CO and CO₂ could have contributed to the apparently high C contents measured in Ref. [38]. With the current improvements introduced in the procedure applied for the combustion analysis (cf. Section 3.2) this possible influence was reduced significantly in the present work. Another explanation for overestimation of the C solubility in solid Cu could be the presence of a third element with more affinity to C than Cu. The purity of the Cu used in Ref. [38] was not indicated and determinations for the starting material were not reported. The claim of a solubility of C in solid Cu at 1173 K lower than 0.5 at.ppm (0.1 wt.ppm) in Ref. [43] could be caused by inappropriate saturation with C of the Cu specimens.

The solubility of C in solid Cu increases with increasing temperature (Table 3.1). The increase of the solubility of C with increasing temperature in a solid solution in equilibrium with graphite is given by the following equation if Henrian behaviour is assumed for the C activity [46]

$$\frac{x}{1-2x} = \exp\left(-\frac{\Delta H}{RT}\right) \exp\left(\frac{\Delta S}{R}\right) \quad (3.1)$$

where x is the carbon content in mole fraction, ΔH is the partial molar enthalpy of carbon in solution, ΔS is the partial molar excess entropy, R is the gas constant, and T is the absolute temperature. An Arrhenius presentation according to Eq. (3.1) is given in Fig. 3.3. The experimental data can be well fitted with a straight line, as prescribed by Eq. (3.1), implying validation of Henrian behaviour for the C activity in Cu. From the slope of the

straight line fitted (least squares analysis) a partial molar enthalpy of dissolution of C in Cu was determined: $\Delta H = 35.1$ kJ/mol. This value is smaller than the value 51.9 kJ/mol reported in Ref. [38] on the base of much higher (erroneous, see above) solubility data.

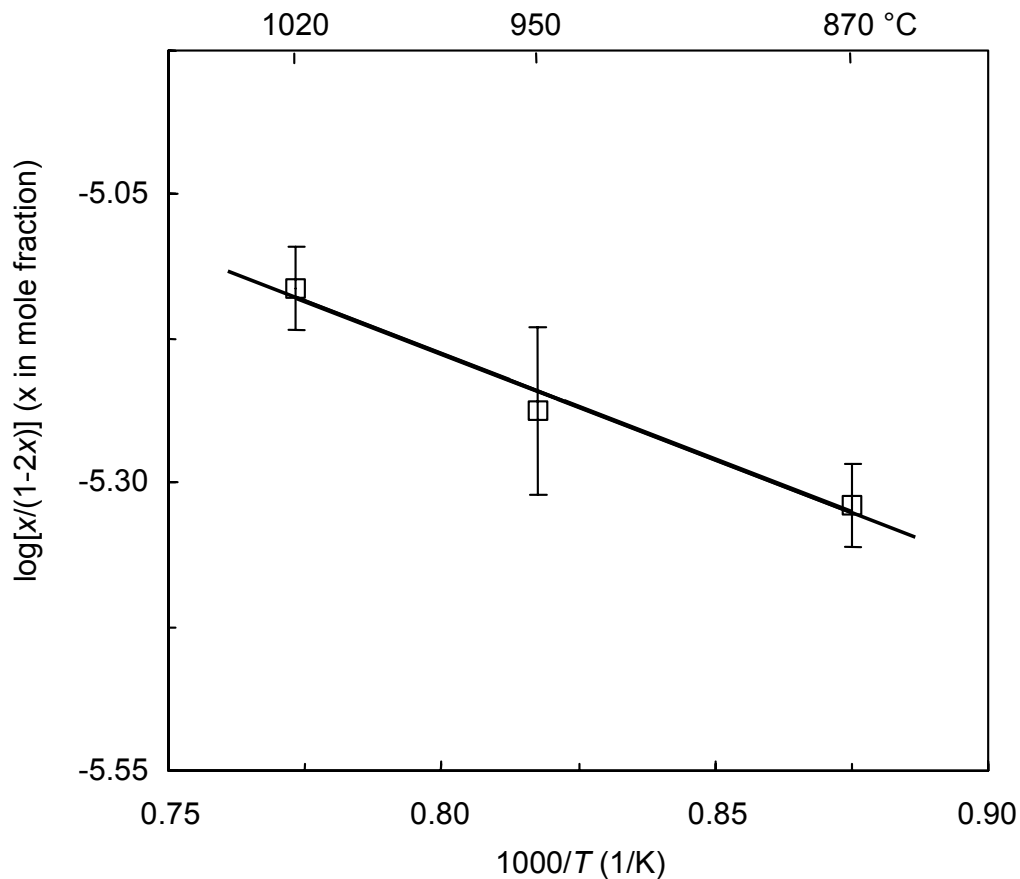


Fig. 3.3. The equilibrium solubility of C in solid Cu as a function of temperature. The experimental error in the C solubility has been indicated by a vertical bar.

An additional comment will be given here on the volume diffusion coefficient of C in Cu, D . In the literature there are no data available. It has been shown that annealing for 72 h at 1143 K and at higher temperatures suffices to saturate with C the Cu substrate slices of a thickness, z , of 4 mm. Hence, an underestimate for the volume diffusion coefficient of C in Cu can be made from the relation $D \approx z^2/2t$. Thus, it follows for a tempera-

ture of 1143 K $D = 3 \times 10^{-11}$ m²/s. This value differs from the volume diffusion coefficient of C in Ni at the same homologous temperature ($T/T_m = 0.84$, where T_m is the melting temperature) only by a factor of 3 [47].

Based on the too high (see above) solubilities of C in *solid* Cu reported in Ref. [38], in comparison with the very low solubility of C in *liquid* Cu near the melting point of pure Cu, it was suggested that a peritectic type of phase diagram instead of a eutectic one would hold for the Cu–C system at the Cu-rich side (cf. Fig. 3.1) [37]. According to the present results, the solubility of C in solid Cu near the melting point is moderately larger than that in the liquid and, if the extrapolated liquidus line reported in Ref. [42] is adopted (solid line in Fig. 3.4), a peritectic type of phase diagram could be drawn indeed (Fig. 3.4). It should be noted that this extrapolation of the liquidus line is based on recent experimental data obtained at high temperatures (above 1823 K; see Fig. 3.1). The experimental data of Ref. [41] are rather old and may be affected by impurities in the starting materials. Yet, the possibility of a eutectic type of phase diagram should not be fully excluded. To make definitive conclusions about the type of the equilibrium phase diagram of the Cu–C system, further investigations on the solubility of C near the melting point of Cu are required.

3.4. Conclusions

The solubility of C in solid Cu was determined by means of a recently improved combustion analysis procedure. Equilibrium values varying from 4.8 ± 0.5 at.ppm (0.9 ± 0.1 wt.ppm) at 1143 K to 7.4 ± 0.5 at.ppm (1.4 ± 0.1 wt.ppm) at 1293 K were determined. These solid-solubility values are 50 times smaller than the data reported before and as included in the most recent assessment of the equilibrium phase diagram. A Henrian behaviour for the carbon activity in the interstitial solid solution was observed.

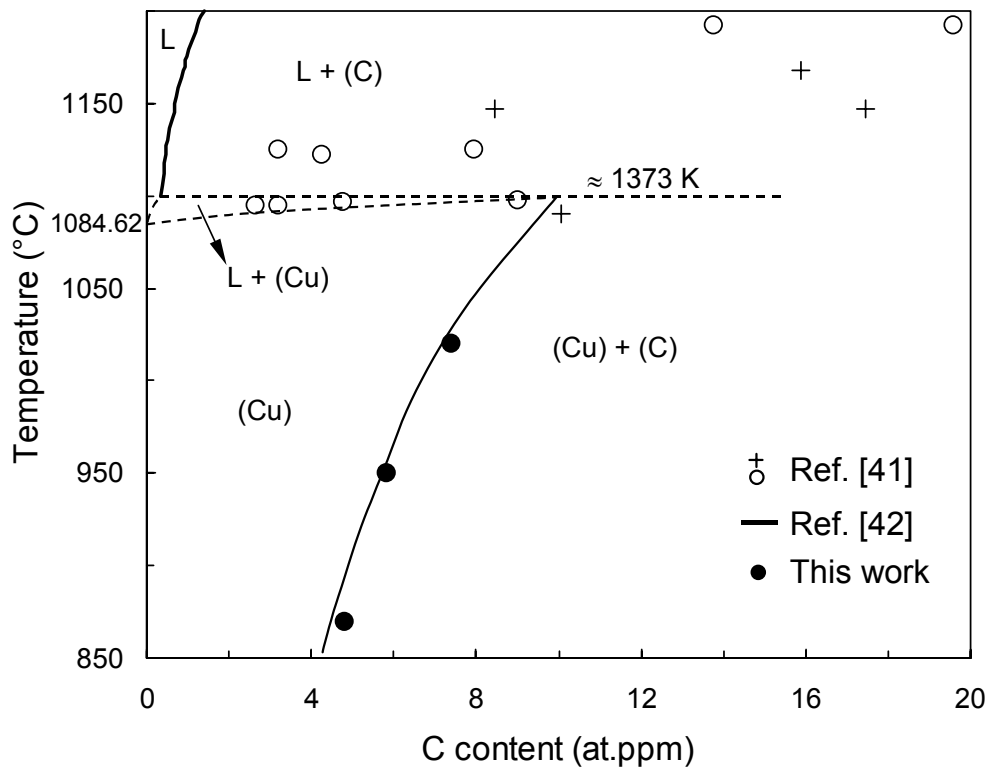


Fig. 3.4. Proposed equilibrium phase diagram of peritectic type for the Cu–C system at the Cu-rich side (see text).

4. Discontinuous precipitation in a Cu-4.5 at.% In alloy

G.A. López, P. Zieba*, W. Gust and E.J. Mittemeijer

* *Institute of Metallurgy and Materials Science, Polish Academy of Sciences, Cracow, Poland*

Abstract

The morphology and kinetics of the discontinuous precipitation reaction in a Cu-4.5 at.% In alloy were studied by means of analytical electron microscopy. A grain boundary movement was experimentally observed before the precipitation reaction at this grain boundary started. Subsequent development of the discontinuous precipitation reaction led to the formation of an ($\alpha + \delta(\text{Cu}_7\text{In}_3)$) lamellar two-phase microstructure, where α is the In-depleted solid solution and δ is the precipitate phase. By application of energy-dispersive X-ray microanalysis a solute depletion in the α lamellae in the wake of the advancing reaction front was observed. Indium concentration profiles were determined parallel to the moving reaction front for individual α lamellae. These concentration profiles fall into two categories, namely symmetrical ones and asymmetrical ones with respect to the central axis of the α lamella, which were attributed to regular morphology and irregular morphology of the discontinuous precipitates, respectively. A local analysis was applied to characterize the kinetics of the discontinuous precipitation reaction and the corresponding grain-boundary diffusivity values were determined.

4.1. Introduction

The typical *discontinuous precipitation* (DP) reaction concerns the formation of a solute-depleted phase and a precipitate phase as a usually lamellar microstructure behind a GB advancing into the supersaturated matrix [48,49]. In this reaction the crystal structure of the solute-depleted phase remains the same as the parent phase. A discontinuous change in both the crystal orientation and the solute concentration of the parent phase across the moving interface characterizes this kind of reaction. A precipitation that involves nucleation and growth without the participation of a (moving) GB is called *continuous precipitation*. These definitions will be used in the present contribution.

Since the late seventies the use of analytical electron microscopy has become a powerful technique to investigate the local chemical composition changes accompanying the DP reaction. By means of this technique it was shown for the first time [50–52] that an abrupt change in the solute concentration occurs across the reaction front (RF), i.e., the moving grain boundary (GB), as well as that a concentration variation exists in the solute depleted lamellae of the parent phase in a direction parallel to the RF. The occurrence of such a concentration variation was predicted in 1959 [53]. Similar investigations of discontinuous precipitation reactions were successfully conducted for systems as Al–Zn [54–56], Co–Al [57], Co–W [58], Mg–Al [52,59,60], Ni–In [61], and Ni–Sn [62,63]. Studies of discontinuous precipitation in Al–Zn [56] and Ni–Sn [63] alloys have initiated the introduction of a local analysis of the DP kinetics instead of the global approach employed previously. Thereby, the discrepancy in the values for diffusivities as determined previously using different global analysis was removed. In the local analysis [63–65] each cell, formed by α and δ lamellae, possesses its own growth velocity, lamellar thickness and concentration variation. In the global approach, average values for these parameters

are employed for the whole population of cells. The results obtained upon applying a local analysis to the DP reaction in the Al–Zn and Ni–Sn systems showed that the diffusion along migrating and stationary GBs occurs with about the same rate [56,63].

In the present work, the morphology and the kinetics of the DP reaction in a Cu-4.5 at.% In alloy was investigated. Analytical electron microscopy was used to determine the solute concentration profile in the solute-depleted solid solution in the wake of the RF of the DP reaction. The Cu–In system was chosen because the kinetic parameters of the DP reaction applying the global approach are well documented [66–71] and reliable data on diffusion along stationary GBs exist [72]. These existing data were compared with the $s\delta D_b$ values (D_b is the GB chemical diffusion coefficient, δ the GB thickness, and s the segregation factor) that were determined here for a wide range of temperatures using the local concept. The activation energy of the DP reaction in Cu–In alloys was determined, for the first time, from the Arrhenius dependence of the *local* $s\delta D_b$ values.

4.2. Experimental details

The Cu-4.5 at.% In alloy was prepared by melting appropriate amounts of Cu and In (both of 99.99 wt.% purity) in an Al_2O_3 crucible and casting the melt into steel moulds of 15 mm diameter. The castings were homogenized at 800 K for 150 h to remove any segregation generated during the casting. To increase the probability of finding suitable places for transmission electron microscopy (TEM) investigation of the DP reaction, a high density of GBs is required. Therefore, the grain size resulting after casting and homogenisation (1 mm) had to be reduced. The rods were cold-worked by hammering leading to 33 % reduction in diameter, cut into 1.5 mm thick slices, and heat-treated at 800 K for 22 h in an evacuated silica

ampoule, which led to a grain size of 30–300 μm as determined using an intersection method after cooling to room temperature for few specimens. Next, the samples used for investigation of DP were directly cooled down to the temperature at which the first stage of a two-stage ageing procedure was carried out. Direct cooling to ageing temperature minimizes the probability of continuous precipitation in the supersaturated matrix (upon cooling to room temperature), which could affect the kinetics of a DP reaction to be induced upon subsequent annealing [67,73].

The first stage of the two-stage ageing procedure was performed at a temperature 50 degrees higher than the temperature of the second stage at which the samples were finally annealed for the TEM investigation. The temperatures of the second stage were in the range 525 – 650 K. The first stage was intended to induce the DP reaction at most GBs of the samples and to overcome the stage of non-cooperative growth of cells. The applied annealing times for the first stage were determined on the basis of the average RF velocities published in the literature [68]. Next, the samples were cooled down to the selected temperature of the second stage and annealed for a certain period of time. During this annealing a new layer of DP products grew with a smaller interlamellar spacing, as compared to the final DP product of the first stage of ageing. This marked change in the interlamellar spacing allowed to determine the distance covered by growth of the DP product in the second ageing stage, which was used to determine the RF velocities. It is noted that the transition period between both ageing steps takes only 5 % of the total time of the second stage. At the end of the second stage, the samples were water quenched.

Before metallographic examination using a light microscope the aged samples were ground and mechanically polished, using 0.05 μm Al_2O_3 suspension in the last polishing step. Chemical etching with a solution of 10 % FeCl_3 in methanol for 10–15 s was utilized to reveal the microstructure of the DP reaction products in the light microscopical analysis.

Thin foils for TEM analysis were prepared from discs of 3 mm in diameter punched from the aged specimens. Finally, jet electropolishing was performed in an electrolyte of 33 % nitric acid in methanol at a temperature of -30 °C with a potential of 5–10 V to get electron transparent areas in the discs. TEM was carried out using a Philips CM 20 Twin microscope equipped with an energy-dispersive X-ray (EDX) spectrometer, enabling compositional analysis with a high lateral resolution (≈ 10 nm). The microscope was operated with an accelerating voltage of a 200 kV in the nano-probe mode using a LaB₆ source of electrons. The lateral size (“full width at half maximum”) of the incident electron beam was 3–9 nm. The specimens were tilted approximately 20° towards a Si(Li) X-ray detector, which resulted in a 40° take-off angle. Attention was paid to the proper location of the region analysed in relation to the incident electron beam and the X-ray detector [74]. The average foil thickness calculated from the contamination spots at the top and bottom of the foil was 100–230 nm. As this method usually overestimates the foil thickness, the results were checked using convergent beam electron diffraction. The difference in the thickness values obtained from the two methods was smaller than 20 %.

The intensity of the characteristic K_α X-ray peaks, I_{Cu} and I_{In} , were recorded for a time of 100 s. This resulted in the accumulation of a few thousand counts for the minor element; the associated relative error (3σ) due to counting statistics was 3–4 %. The In concentration at the points analysed was obtained from the observed characteristic X-ray intensities using the equation [75]:

$$\frac{x_{\text{Cu}}}{x_{\text{In}}} = k \frac{I_{\text{Cu}}}{I_{\text{In}}} \quad (4.1)$$

where x_{Cu} and x_{In} are the mole fractions of Cu and In in the alloy ($x_{\text{Cu}} + x_{\text{In}} = 1$). The factor $k = k_{\text{Cu-Si}} / k_{\text{In-Si}}$ was determined experimentally as the ratio

of the elemental sensitivity factors for pure Cu and pure In, both with respect to Si as the standard element. The measured values were $k_{\text{In-Si}}=1.15$ and $k_{\text{Cu-Si}}=1.73$. The thickness of the α lamellae was estimated directly from the TEM images. To this end special attention was paid to orient the samples in such a way that the α/δ interfaces were perpendicular to the field of view, by an appropriate tilting of the thin foil holder.

4.3. Results and discussion

4.3.1. *Overall morphology*

Typical structures as reported in previous works [66–69,73] on DP in Cu–In alloys were observed. Upon annealing in the two-phase region of the equilibrium phase diagram [76] the parent supersaturated solid solution α_0 decomposed into a lamellar reaction product consisting of the α solute-depleted solid solution and the $\delta(\text{Cu}_7\text{In}_3)$ intermetallic phase. Representative examples of the overall morphology of the DP reaction are shown in Fig. 4.1. The reaction starts at GBs present in the original α_0 supersaturated solid solution, leading to characteristic seams at both sides of these GBs (Fig. 4.1). From examination of the microstructure it can be observed that the parallel growth of the lamellae takes place only after a period of less cooperative evolution of the initial precipitates has been overcome (Fig. 4.1b).

4.3.2. *Early stages*

The details of the morphology and chemistry of the DP reaction can be revealed by using TEM. A first stage of growth is shown in Fig. 4.2: the origi-

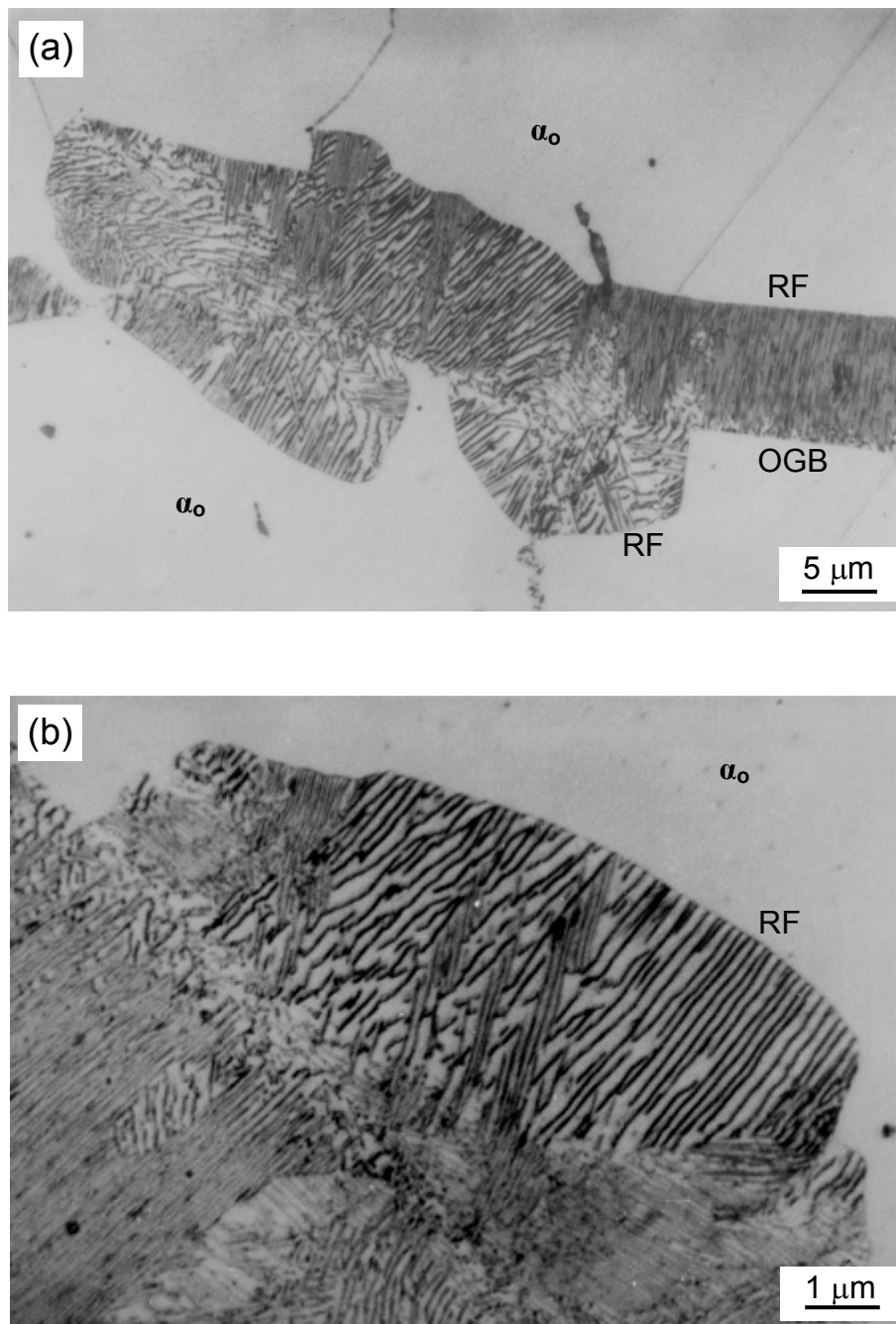


Fig. 4.1. Optical micrographs (bright field) showing growth of colonies of lamellar precipitates in Cu-4.5 at.% In aged for 10 h at 600 K followed by 8 h at 550 K. Formation of a double seam at both sides of the original grain boundary (OGB) (a). Development of arrays (parallel lamellae) of discontinuous precipitates. RF = reaction front; α_0 = supersaturated solid solution.

nal position of the GB has been indicated by a dashed line; apparently the RF has moved from this GB. In a next stage, a strong bowing out of the migrating RF is caused by the formed, pinning $\delta(\text{Cu}_7\text{In}_3)$ precipitates (see Fig. 4. 3a). These precipitates work subsequently as sinks, to which the In atoms diffuse. Afterwards the $(\alpha + \delta)$ lamellar structure is formed.

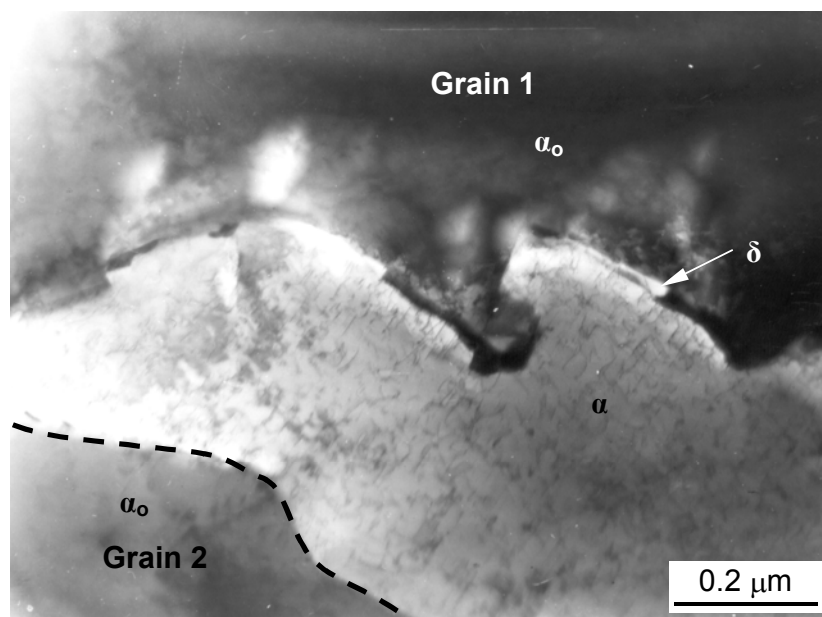


Fig. 4.2. TEM image (bright field) showing the initial stage of formation of $\delta(\text{Cu}_7\text{In}_3)$ precipitates at the moving α_0/α interface (reaction front) in Cu-4.5 at.% In aged for 10 h at 600 K followed by 10 h at 550 K. The position of the original grain boundary is marked by a dashed line.

The migrating RF acts as a diffusion path for the solute atoms as indicated by data obtained from EDX microanalysis. A concentration profile measured along the line A–A in Fig. 4.3a shows that the region swept by the RF has been depleted of In and that an abrupt change in the In content occurs at the α_0/α interface (Fig. 4.3b). A concentration profile measured along the line B–B perpendicularly to the RF is shown in Fig. 4.3c. The In content in the solute-depleted α -phase decreases in the direction from the RF to the original GB in the In-depleted zone.

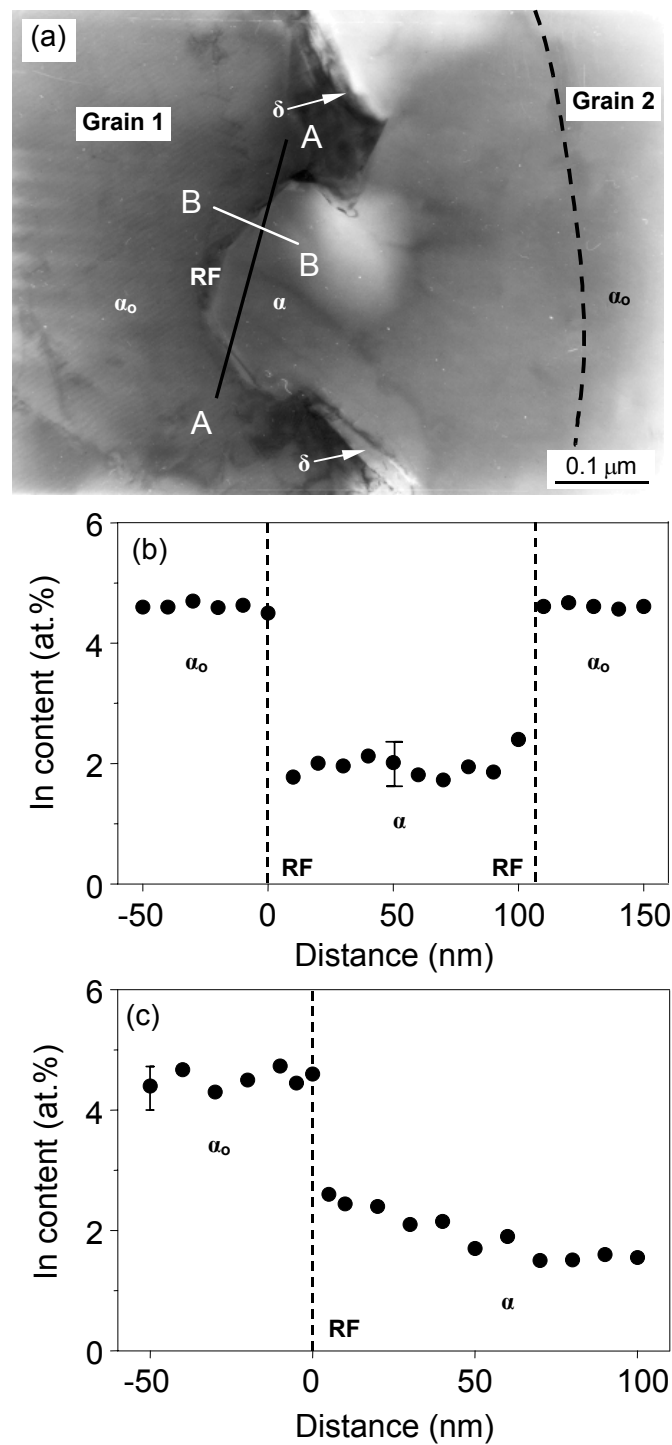


Fig. 4.3. (a) TEM image (bright field) showing grain boundary bowing out between (beginning) In-rich lamellae in Cu-4.5 at.% In aged for 10 h at 600 K followed by 10 h at 550 K. The position of the original grain boundary is marked by a dashed line. (b,c) In concentration profiles taken along the A–A and B–B lines, respectively. The experimental error in the In concentration values indicated by a vertical bar.

The following scenario is suggested for the development of the DP reaction in Cu–In alloys (Fig. 4.4). The originally precipitate-free GB (Fig. 4.4a), from now on the RF, migrates some distance (Fig. 4.4b). The region swept by the RF has become depleted of In and at a certain time, i.e., after some distance of migration of the RF, precipitates of the $\delta(\text{Cu}_7\text{In}_3)$ phase begin to develop (Figs. 4.2 and 4.4c). As the RF continues to migrate a bowing out of the RF between the pinning δ precipitates occurs (Figs. 4.3 and 4.4d). The In atoms caught from the α_0 matrix by the advancing RF diffuse along the RF to the developing δ precipitates, which are situated at the extremities of the bowing boundary and which increase in length. In this way the lamellar precipitate geometry of the DP cells is initiated (Fig. 4.4d). The above picture largely parallels the model proposed previously for the DP reaction in Al-22 at.% Zn alloys [77]. However, in Ref. [77] the initial precipitate spacing is thought to be much larger than the eventual interlamellar spacing of the DP cell, implying renucleation of precipitate lamellae upon continued growth. This contrasts with the results of this work: here lamellar colonies grow directly from the first developed, pinning precipitates at the bowing RF.

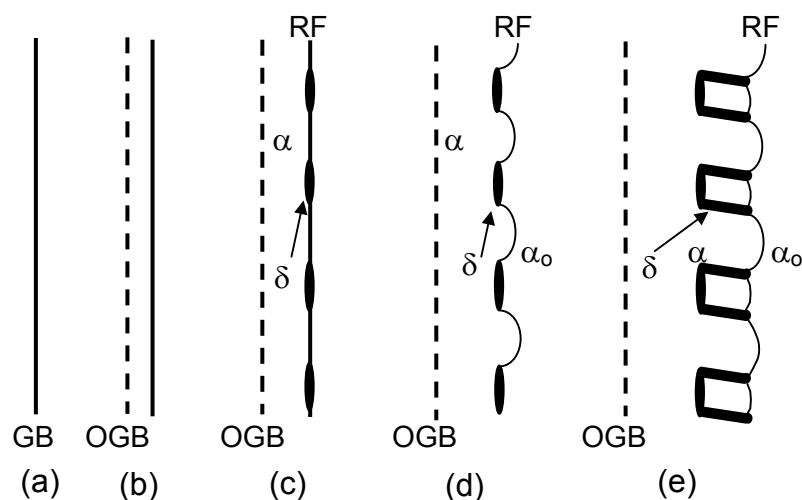


Fig. 4.4. Schematic presentation of the initial stage of the DP reaction: the development of δ lamellae. The position of the original GB (a) is marked by a dashed line and the symbol OGB (b–e).

4.3.3. Steady-state growth

The steady-state stage of growth is characterized by an approximately constant average RF velocity and a nearly constant lamellae spacing (cf. Fig. 4.5). For this stage of growth, In concentration profiles were measured in the solute-depleted α lamellae in the wake of the RF and parallel to it. The In concentration decreased from the middle to the edge of the α lamellae for the range of temperatures investigated. All such measured profiles showed a maximum In content in the middle of the lamella, noticeably higher than the concentration according to the solvus line in the equilibrium phase diagram [76] (see Fig. 4.6). Further, with respect to the central axis of the α lamella, symmetrical and asymmetrical In concentration profiles were observed (Fig. 4.6). The most frequently observed concentration-profile shape was the symmetrical one, as expected for the so-called regular morphology of the lamellar structure [59,60,65], where the interlamellar spacing as well as the growth direction remain almost constant. The asymmetrical concentration-profile shape is attributed to the so-called irregular morphology [59,60,65]. This kind of morphology is ascribed to cases where changes of growth direction, branching or even renucleation of the precipitate lamellae at the RF occur, in order to keep the interlamellar spacing compatible with the steady-state condition.

Symmetrical profiles

The quantitative data obtained in this work for the In concentration profiles in the solute-depleted α lamellae in the wake of and parallel to the advancing RF enable the verification of a theoretical prediction. The α lamellae cannot be solute-depleted down to the equilibrium composition for any non-zero RF velocity. To arrive at a model allowing quantification of this effect the following simplifying assumptions were made [53]:

1. The advancing RF is plane.

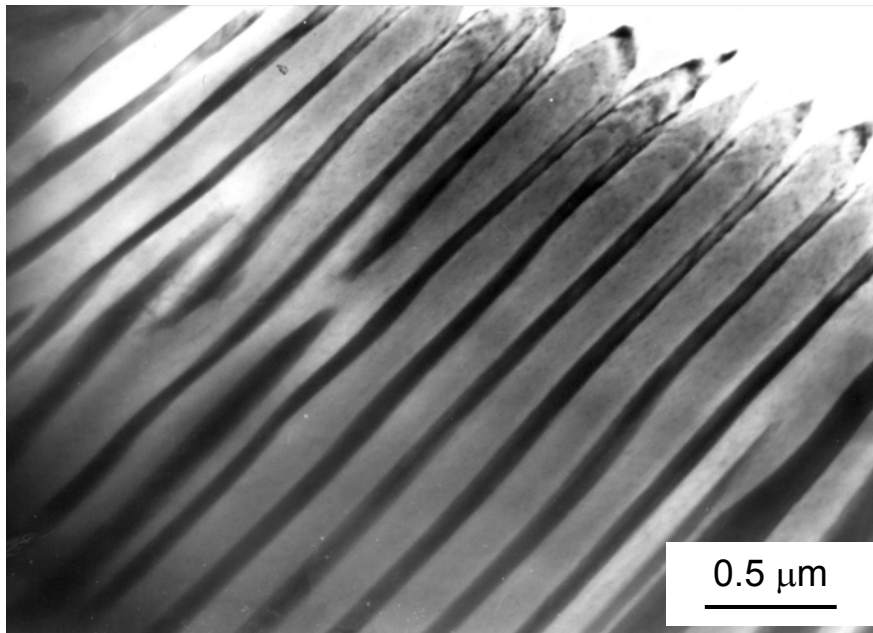


Fig. 4.5. TEM image (bright field) showing the growth of parallel lamellae of the solute-depleted α solid solution and $\delta(\text{Cu}_7\text{In}_3)$ phase in a Cu-4.5 at.% In alloy aged for 10 h at 600 K followed by 10 h at 550 K.

2. Diffusion occurs only along the RF, i.e., volume diffusion in the α and α_0 phases is assumed to be negligible. The thickness of the GB is constant and sufficiently small so that no concentration variation occurs across its thickness. The chemical diffusion coefficient along the GB is concentration-independent.
2. The system is in a steady state, i.e., the concentration gradients along the RF are constant/stationary.
3. The solute concentration in the RF is proportional to the concentration in the solute-depleted α lamella.
4. The (α and δ) phases are in thermodynamic equilibrium at the interface between the (α and δ) lamellae (i.e. local equilibrium).

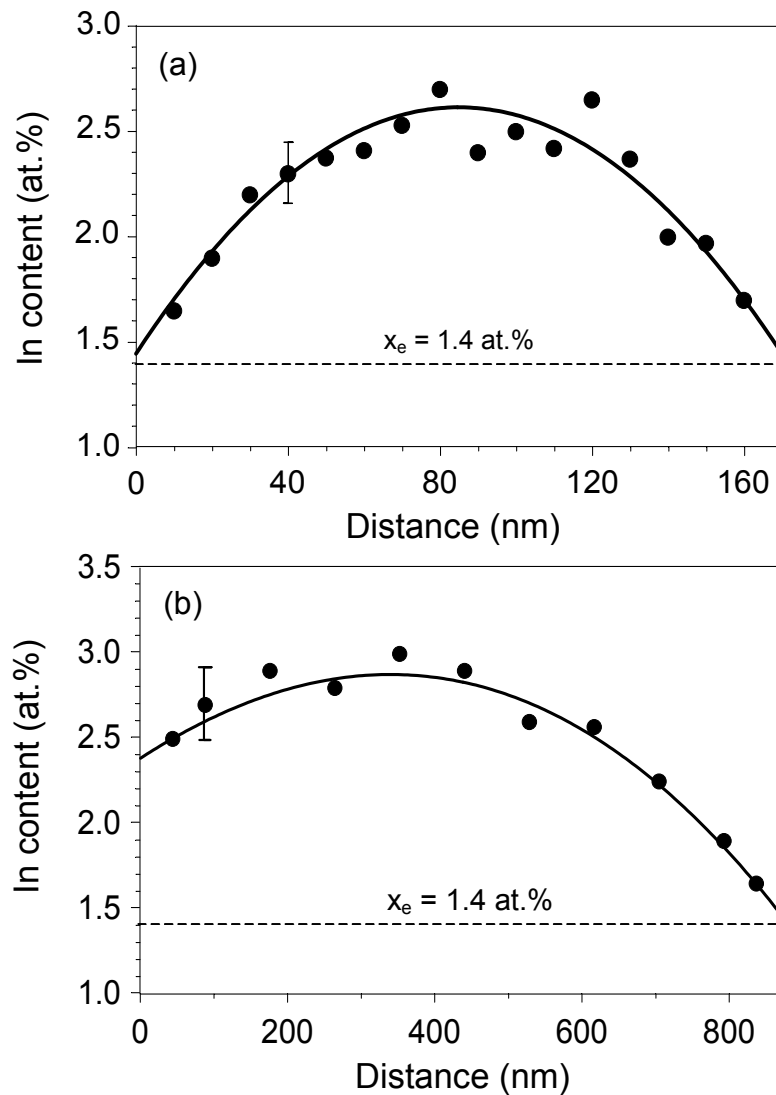


Fig. 4.6. Examples of symmetrical (a) and asymmetrical (b) In concentration profiles measured across the α lamellae in Cu-4.5 at.% In aged for 10 h at 600 K followed by 10 h at 550 K. The concentration x_e at the α/δ interface according to the equilibrium phase diagram [76] has been indicated.

On this basis, after solving the diffusion equation along the RF, the following expression was obtained for the concentration x in the solute-depleted matrix (α) lamella:

$$x(y) = (x_e - x_0) \frac{\cosh\left(\left(y - \frac{1}{2}\right)\sqrt{C}\right)}{\cosh\left(\sqrt{C}/2\right)} + x_0 \quad (4.2)$$

with the dimensionless parameter C given by:

$$C = \frac{v\lambda_{\alpha}^2}{s\delta D_b} \quad (4.3)$$

where x_0 is the solute content in the supersaturated solid solution (α_0), x_e is the equilibrium concentration in the α -phase lamella at the α/δ interface, and y is the coordinate perpendicular to the growth direction and perpendicular to the plane of the α/δ interface, and normalized such that $y=0$ corresponds to one edge of the α lamella at the α/δ interface and $y=1$ corresponds to the opposite edge of the same lamella. The width of the α lamella is given by λ_{α} , and v is the cell growth velocity of the RF. In Eq. (4.3) D_b is the GB chemical GB diffusion coefficient, δ the GB thickness, and s the segregation factor. It follows from Eq. (4.2) that the larger the dimensionless parameter C the higher the expected excess of solute (as compared with x_e), expressed by $x(y)$, in the solute-depleted α solid solution.

The full line in Fig. 4.6a represents the least-squares fit of Eq. (4.2) to the experimental data. In the original paper, x_e was taken as a known boundary condition. For the fitting applied here both x_e and C were taken as fitting parameters. The data used for the fitting and the fit results for x_e and C are collected in Table 4.1. The experimental concentration profiles used for the fitting were determined only for those ($\alpha + \delta$) colonies where the α and δ lamellae exhibited approximately the same thickness for a sufficiently long distance in the growth direction. Because of the two-step annealing procedure, described in Section 4.2., the error in the reaction times associated with possible occurrence of an incubation period for the start of the DP was avoided.

Table 4.1. Local analysis of the DP kinetics. λ_α = width of the α lamella, for C see Eq. (4.3), x_e = In concentration at the α/δ interface (the values indicated for x_e from Ref. [76] are the equilibrium solubilities in α), v is the RF velocity, and $s\delta D_b$ is the chemical GB diffusivity. The values of C and x_e have been determined by fitting Eq. (4.2) to the experimental data. The $s\delta D_b$ values have been determined using Eq. (4.3).

$T(K)$	Lamella No.	λ_α (nm)	C	x_e (at.% In) fit result	x_e (at.% In) [76]	v (nm/s)	$s\delta D_b$ (m^3/s)
525	1	75	2.47	1.21	1.3	0.26	5.9×10^{-25}
	2	120	3.54	1.25		0.20	8.1×10^{-25}
	3	150	3.92	1.27		0.35	2.0×10^{-24}
	4	94	2.97	1.22		0.67	2.0×10^{-24}
	5	105	3.21	1.30		0.88	3.0×10^{-24}
550	1	170	4.73	1.43	1.4	0.36	2.1×10^{-24}
	2	120	2.87	1.30		0.92	4.6×10^{-24}
	3	135	3.57	1.35		0.46	2.3×10^{-24}
	4	160	4.11	1.29		0.78	4.8×10^{-24}
	5	100	2.12	1.32		1.65	7.8×10^{-24}
575	1	190	4.03	1.41	1.6	1.21	1.1×10^{-23}
	2	167	3.94	1.47		0.72	5.1×10^{-24}
	3	150	3.77	1.45		0.99	6.0×10^{-24}
	4	135	3.51	1.43		2.32	1.2×10^{-23}
	5	120	3.27	1.50		0.62	2.7×10^{-24}
600	1	210	3.52	1.65	1.7	0.80	1.1×10^{-23}
	2	190	3.07	1.67		1.70	1.9×10^{-23}
	3	170	2.93	1.62		2.53	2.5×10^{-23}
	4	160	2.54	1.62		2.97	3.0×10^{-23}
	5	140	2.11	1.60		4.30	4.1×10^{-23}
625	1	210	4.22	1.87	2.0	1.35	1.9×10^{-23}
	2	231	4.01	1.90		3.00	4.1×10^{-23}
	3	210	3.76	1.92		5.11	6.0×10^{-23}
	4	189	3.58	1.95		10.0	1.1×10^{-22}
	5	170	3.21	1.91		22.2	1.9×10^{-22}
650	1	370	4.27	2.28	2.3	2.48	8.1×10^{-23}
	2	380	4.83	2.39		3.34	1.0×10^{-22}
	3	330	3.73	2.35		5.82	1.7×10^{-22}
	4	310	3.26	2.30		6.78	2.0×10^{-22}
	5	290	3.01	2.31		10.7	2.9×10^{-22}

Considering the data presented in Table 4.1, it follows that the solute content at the α/δ interface corresponds rather well with the value for the α -phase in equilibrium with the δ -phase [76] (i.e., local equilibrium prevails). This result is compatible with previous results obtained for the DP reaction in Mg–Al [52], Co–Al [57], Co–W [58], and Ni–Sn [63] alloys. It

should be mentioned here that all EDX measurements performed close to the α/δ interfaces were accomplished in such a way that the excited volume belonged still/just to the α solid solution, so that no X-rays were excited from the $\delta(\text{Cu}_7\text{In}_3)$ phase. The lateral resolution of the EDX analysis was about 5–10 nm and thus it was impossible to determine the In content exactly at the α/δ interface. Using atom probe ion microscopy a higher lateral resolution is possible. Applying this technique for the DP reaction in a Ni-7.5 at.% In alloy it was found [78] that the In content in the α lamella at the interface with the δ lamella was significantly higher than the equilibrium concentration ($x_e = 0.9$ vs. 0.45 at.% In).

As follows from Table 4.1 at a constant temperature the parameter C increases with increasing α lamellae thickness. This is compatible with previous results obtained for DP in the Co–Al [57] and Ni–Sn [63] systems. A slight tendency for increase of C with increasing temperature can also be observed. The scatter of the C values at the same temperature indicates that during growth of an individual cell, changes of interlamellar spacing and growth rate occur, indicating that a local approach to kinetic analysis of DP has to be preferred over the global approach where global averages are used for parameters as the lamellar thickness, growth velocity and solute content within the α lamella.

Asymmetrical profiles

The asymmetrical profiles, as a consequence of an irregular growth morphology (see above), cannot be described directly by Eq. (4.2). A modification of the classical model [53] has been proposed in Ref. [57] for the case of an asymmetrical concentration profile in the α lamella parallel to the RF. Instead of the value x_e an arbitrary value x_i was assigned to the solute content at the α/δ interface and it was imposed that $dx/dy=0$ must hold at the coordinate $y=p$ where the solute concentration profile reaches a maximum.

It is obtained for the solute concentration profile parallel to the RF (cf. Eq. (4.2)):

$$x(y) = (x_i - x_0) \frac{\cosh(\sqrt{C}(y - p))}{\cosh(p\sqrt{C})} + x_0 \quad (4.4)$$

Applying an analogous fitting as in the case of symmetrical concentration profiles, values for the C parameter and x_i can be obtained.

A part of a precipitation cell, demonstrating irregular morphology of an α lamella accompanied by two δ lamellae is shown in Fig. 4.7a. Note the change of the α lamella thickness corresponding to the change in growth direction of the δ lamella in the lower part of the figure. The results of EDX measurements of In concentration profiles along the lines z_1 – z_5 (see Fig. 4.7a) are presented in Fig. 4.7b. A symmetrical concentration profile, with respect to the central axis of the α lamella, is observed along z_1 and z_5 . Deviations of the symmetry are observed for the concentration profiles along the lines z_2 – z_4 . It can be seen that the occurrence of asymmetrical profiles leads to an increase of the C parameter (see C values listed in Fig. 4.7b). Although even for the most asymmetrical profiles (z_3 , z_4) the C parameter is larger than 3, these values are well within the range of values obtained for the regular morphology at the same temperature (see Table 4.1). This suggests that both kinds of growth belong to the steady-state stage of the DP reaction.

Diffusivity at the migrating reaction front

An ultimate aim of the investigation of kinetics of the DP reaction has been the determination of the diffusivity at the moving RF. Until now, most of the information concerning the $s\delta D_b$ values (cf. Eq. (4.3)) was derived applying the global approach to the DP. Usually, two different models were used to determine $s\delta D_b$:

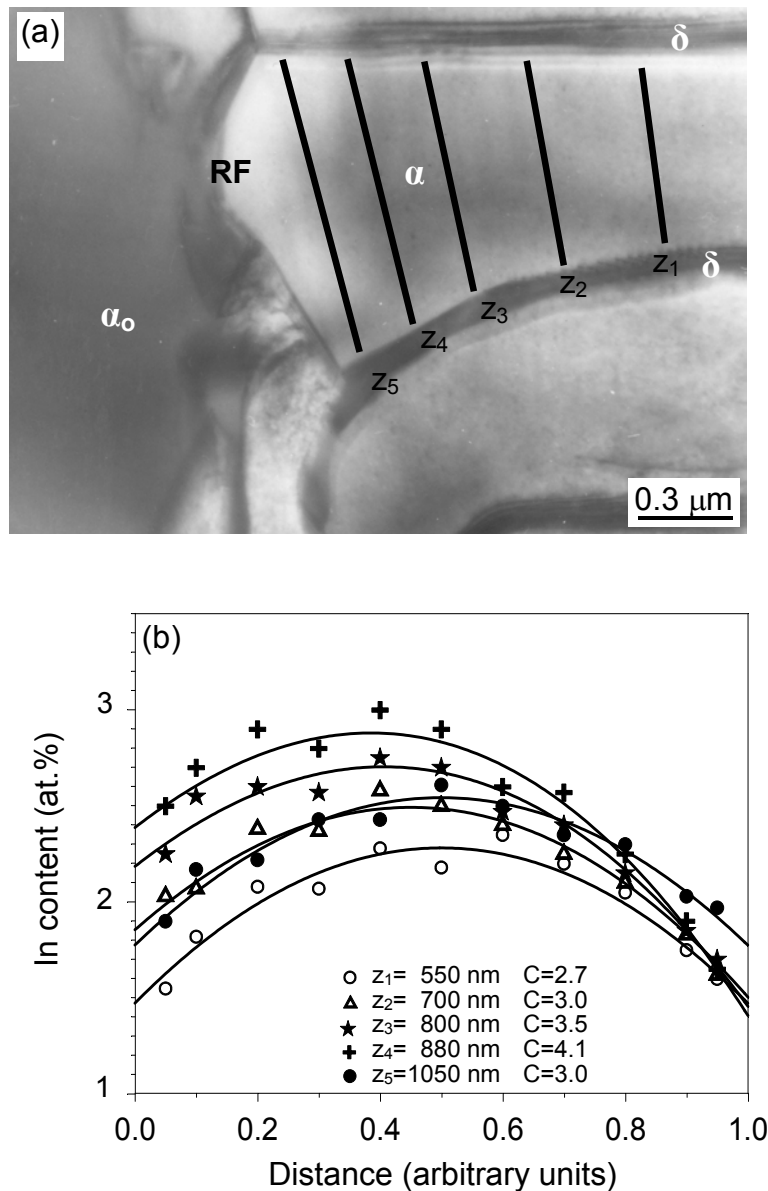


Fig. 4.7. (a) TEM image (bright field) showing a change in the growth direction of lamellae in a single cell of discontinuous precipitates in Cu-4.5 at.% In aged for 10 h at 600 K followed by 10 h at 550 K. (b) In concentration profiles taken across the α lamella at various distances z_1 – z_5 (see (a)) from the reaction front (RF).

1. By integration of Eq. (2) the average value of solute concentration in the α lamella, x_{av} , is obtained:

$$x_{av} = \int_0^{\lambda_\alpha} x(y)dy / (\lambda_\alpha) = \frac{2}{\sqrt{C}} \tanh \frac{\sqrt{C}}{2} \quad (4.5)$$

Knowing x_{av} , from X-ray diffraction measurements (i.e., x_{av} is a global average attained from all simultaneously diffracting cells), it is possible to find a global value for C from Eq. (4.5), and then, using average values for the growth rate and α lamellae thickness, a global value of $s\delta D_b$ follows from Eq. (4.3).

2. According to Ref. [79] it holds:

$$s\delta D_b = -\frac{v_{av}\lambda_\alpha^2 RT}{8\Delta G} \quad (4.6)$$

where R is the gas constant and T is the absolute temperature, v_{av} is the global average RF velocity, λ_α is the average width of the α lamella, and ΔG is the change in the Gibbs energy upon DP.

The theoretical approach adopted in Ref. [79] departs from the general equation for interface mobility, implying that the interface velocity equals the product of the mobility and the driving force, ΔG . Next, the mobility is described in a rather artificial way in terms of also the diffusivity. This contrasts with Ref. [53] where the diffusion problem at the RF is solved rigorously.

In the present work, the $s\delta D_b$ values were calculated using *local values* for the model parameters of the DP kinetics. The determination of a local value for $s\delta D_b$ is straightforward once the optimum, local value of the parameter C has been determined by the fitting using Eq. (4.2). Consequently, the local value of $s\delta D_b$ follows directly from Eq. (4.3). Data used and results thus obtained have been listed in Table 4.1; the $s\delta D_b$ values are graphically presented in the form of an Arrhenius plot in Fig. 4.8. The values of the pre-exponential factor, $(s\delta D_b)_0$, and the activation energy, Q_b ,

corresponding to the Arrhenius plot in Fig. 4.8, have been gathered in Table 4.2, where for the activation energy corresponding to the local values of $s\delta D_b$, the average was taken of the $s\delta D_b$ values at each temperature.

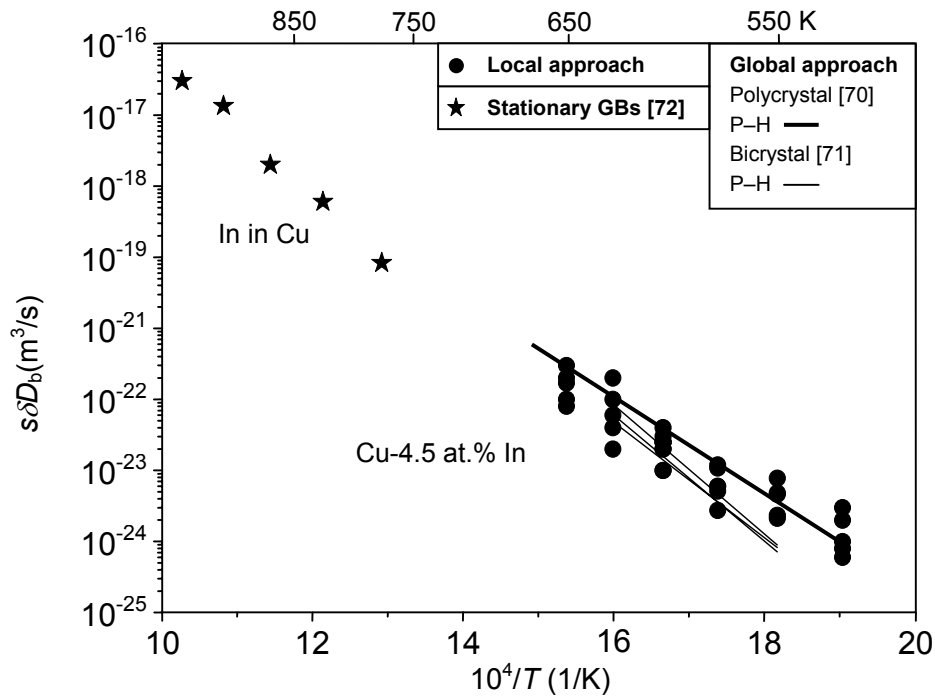


Fig. 4.8. Arrhenius diagram for the grain-boundary diffusivity $s\delta D_b$ along the moving reaction front of the discontinuous precipitation reaction in Cu-4.5 at.% In determined applying global and local data for the RF velocity, lamellar thickness and In concentration. The $s\delta D_b$ values for the tracer diffusion of In in Cu along stationary grain boundaries (GBs) and the $s\delta D_b$ values from the global approach according to the Petermann–Hornbogen (P–H) model (Eq. (4.6)) are shown for comparison.

It follows that the local diffusivities can vary up to a factor of 10 at the same temperature, whereas the experimental accuracy in the obtained diffusivity values is estimated to be within 20 % relative. Local variations in the GB properties can be responsible for this effect: GB structure changes due to varying misorientation of the neighbouring grains or varying inclina-

tion of the GB plane [54] and GB segregation level changes [80]. Further, in the model as applied here (Eqs. (4.2) and (4.3)) it has been assumed that the individual cell growth velocity (v_{in} in Eq. (4.3), see also Table 4.1) is constant, whereas in reality a stop-and-go motion of the RF may occur [81].

Table 4.2. Arrhenius parameters of the grain-boundary diffusivity $s\delta D_b$ of In for the Cu–In system.

Method	$(s\delta D_b)_0$ (m ³ /s)	Q_b (kJ/mol)
Local analysis	2.8×10^{-13}	115
Global analysis		
P–H, polycrystal [70]	1×10^{-10}	144
P–H, bicrystal [71]	$7 \times 10^{-10} - 6 \times 10^{-13}$	146–174
Stationary GBs [72]	4.9×10^{-7}	203

The diffusivity values obtained applying the local approach (full circles in Fig. 4.8) are in a good agreement with the global values obtained applying the model given in Ref. [79] (full lines in Fig. 4.8). Besides, it is observed that the local results for the $s\delta D_b$ values are compatible with the extrapolation of data obtained for diffusivities of In in stationary GBs of Cu at much higher temperatures (see Fig. 4.8). Hence, the results suggest that the rates of diffusion along moving GBs and stationary GBs are similar. Therefore, the diffusivity values obtained for a migrating RF of a DP reaction can be a source of reliable information about the diffusion rate along GBs in general, especially for systems and/or at temperatures where (radiotracer) diffusion data along stationary GBs are not/will not become available.

Application of the model according to Eqs. (4.2) and (4.3) requires that the contribution of volume diffusion of In is negligible. Using the volume diffusion coefficient (D) of In in Cu [82], at the highest temperature employed in the present investigation (650 K) and considering an interlamellar spacing of 300 nm, the equation $t = \lambda_{\alpha}^2 / 4D$ gives an annealing time of about 125 h as estimate for an effective diffusion distance of 300 nm, which time is much longer than the annealing times applied in this study and thus the contribution of volume diffusion can indeed be considered negligible.

4.4. Conclusions

1. The discontinuous precipitation reaction in the Cu-4.5 at.% In alloy involves the initial formation of an α -phase, adjacent to an original grain boundary, which is solute-depleted, followed by the formation of δ precipitates at the reaction front and finally the development of an ($\alpha + \delta$) lamellar microstructure.
2. The In concentration profiles measured in individual In-depleted α lamellae in the wake of the advancing reaction front and parallel to it fall into two categories, namely symmetrical ones and asymmetrical ones, with respect to the central axis of the α lamella. These concentration profile shapes were attributed to regular and irregular growth modes of the discontinuous precipitation product, respectively.
3. Fitting of the theoretical expression for the lateral concentration profiles to experimental data as indicated in conclusion 2 leads to the determination of local values for the chemical grain-boundary diffusivities $s\delta D_b$ in the corresponding reaction front.

4. The chemical grain-boundary diffusivity at the moving reaction front of the discontinuous precipitation reaction in Cu-4.5 at.% In alloy is of the same order of magnitude as the In-radiotracer diffusivity at stationary grain boundaries of pure Cu.

5. Grain-boundary phase transitions in the Al–Mg system and their influence on high-strain rate superplasticity

*B.B. Straumal**, *G.A. López*, *E.J. Mittemeijer*, *W. Gust*
and *A.P. Zhilyaev***

** Institute of Solid State Physics, Russian Academy of Sciences, Chernogolovka, Moscow District, Russia*

*** Institute for Physics of Advanced Materials, Ufa State Aviation Technical University, Ufa, Russia*

Abstract

Grain-boundary (GB) wetting phase transitions were studied, for the first time, in Al–Mg polycrystals (Mg contents of 5, 10, 15 and 20 wt.%; temperature range 763–903 K). It was observed that above 871 K all GBs in the solid Al-rich phase were wetted by a liquid phase. Below 813 K no GBs wetted by a liquid phase were observed. The maximal and minimal temperatures of the GB wetting phase transitions, T_{wmax} and T_{wmin} , were determined. Between 813 and 871 K the percentage of the wetted GBs gradually increases from 0 to 100 %. Grain-boundary *prewetting* (or *premelting*) is given as an explanation for the hitherto not understood high-strain rate superplasticity observed for ternary Al–Mg–X alloys in a narrow temperature range just below the bulk solidus line.

5.1. Introduction

It is well known that some of the most important properties of modern materials in high-technology applications are strongly influenced or even controlled by the occurrence of interfaces such as grain boundaries (GBs) and interphase boundaries (IBs) [83]. The study of nanocrystalline solids increased pronouncedly in the last decade. Due to the inherently high concentration of GBs in nanomaterials the understanding of the interface properties has become of great importance. All processes that can change the properties of GBs (and IBs) affect drastically the bulk behaviour of polycrystalline materials. GB phase transitions provide an important example of such processes [84–88]. GB wetting phase transitions have recently been included in the traditional phase diagrams of several systems [3,88–93].

The occurrence of wetting depends on the GB energy, σ_{GB} . Consider the contact angle θ between a bicrystal and a liquid phase (Fig. 5.1). When σ_{GB} is lower than $2\sigma_{\text{SL}}$, where σ_{SL} is the energy of the solid/liquid interphase, the GB is non-wetted and $\theta > 0^\circ$ (Fig. 5.1a). But if $\sigma_{\text{GB}} \geq 2\sigma_{\text{SL}}$, the GB is wetted and the contact angle $\theta = 0^\circ$ (Fig. 5.1b). The temperature dependence of $2\sigma_{\text{SL}}$ is stronger than that of σ_{GB} . If the curves describing the temperature dependencies of σ_{GB} and $2\sigma_{\text{SL}}$ intersect, the GB wetting phase transition will occur upon heating at the temperature T_w of their intersection (Fig. 5.1c). At $T \geq T_w$ the contact angle is $\theta = 0^\circ$.

The phenomenon of superplasticity has drawn much interest in recent years. Usually superplasticity was observed at relatively low strain rates, typically about 10^{-4} to 10^{-3} s^{-1} . However, it sometimes occurs at extremely high strain rates (up to 10^2 s^{-1}) [94–99] and in this case it is called high-strain rate superplasticity. A small grain size ($\approx 1 \mu\text{m}$) appears to be important for the occurrence of this phenomenon. Additionally, it has often been

observed at temperatures close to the matrix solidus temperature [100,101].

In the present work, the GB wetting phase transition in the two-phase (S+L) region of the Al–Mg system has been investigated. It will be suggested that the occurrence of *prewetting* (or *premelting*) is the reason for the observed high-strain rate superplasticity.

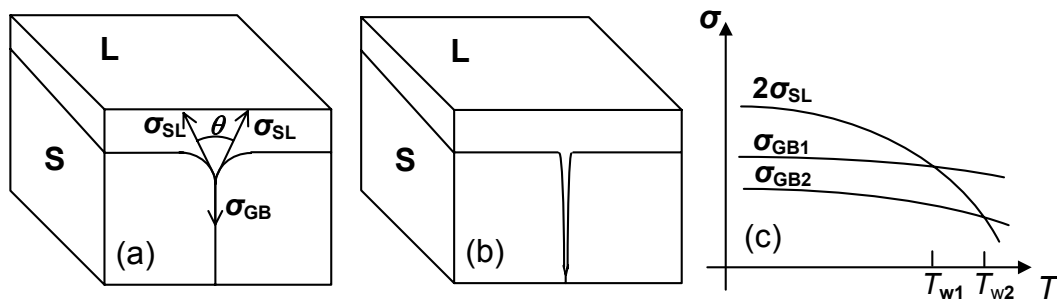


Fig. 5.1. A non-wetted GB in contact with a liquid phase at $T < T_w$, $\theta > 0^\circ$ (a). A completely wetted GB, $\theta = 0^\circ$, $T \geq T_w$ (b). Schematic dependences of $\sigma_{GB}(T)$ and $2\sigma_{SL}(T)$ for two different GBs. They intersect at the T_{w1} and T_{w2} of the GB wetting phase transition (c). L = liquid; S = solid.

5.2. Experimental details

Al (99.999 wt.%) and Mg (99.95 wt.%) were utilised for the preparation of cylinders (diameter ≈ 7 mm) of four Al–Mg alloys with Mg contents of 5, 10, 15 and 20 wt.%. For the wetting experiments, slices (2 mm thick) of the different alloys were cut and sealed into evacuated silica ampoules with a residual pressure of approximately 4×10^{-4} Pa at room temperature. Then, several samples were annealed in furnaces for three days at temperatures between 763 and 903 K, in steps of 10 degrees. The annealing temperature was maintained constant with an accuracy of ± 1 degree. After the anneals the specimens were quenched in water. After quenching, for the metallographic analysis the specimens were embedded in resin and

then mechanically ground and polished, using 1 μm diamond paste in the last polishing step. The unetched samples were inspected by means of light microscopy.

A quantitative analysis of the wetting transition was performed adopting the following criterion: every GB was considered to be wetted only when a liquid layer had covered the whole GB; if such a layer appeared to be interrupted, the GB was regarded as a non-wetted GB. Accordingly, the percentage of wetted GBs was determined on the basis of light microscopy analysis. At least 100 GBs were analysed at each temperature.

5.3. Results and discussion

Optical micrographs of samples annealed at three different temperatures are shown in Fig. 5.2. Upon annealing at 883 K (and at higher temperatures) GB wetting is clearly observed: all GBs were wetted (see the light grey layers at the original GBs in Fig. 5.2a). Upon annealing at 854 K just 26 % of the GBs are wetted (Fig. 5.2b), and no GBs were wetted for annealing temperatures below 813 K. Partial melting occurred in the interior of grains; however, such a liquid in the interior of the solid phase is isolated (see light grey spots in the interior of the grains). Pores can also be observed in the micrographs (see the black spots). The pores are probably formed during solidification of the liquid by rapid quenching. The fraction of wetted GBs is shown as a function of the temperature in Fig. 5.3. Between 813 and 883 K the fraction of the wetted GBs gradually increases with increasing temperature from 0 to 100 %. Therefore, the GB wetting phase transition proceeds in the Al–Mg system between 813 and 883 K. It means that all GB wetting phase transition tie-lines, one for each individual GB, lie between 813 and 883 K. Consequently, $T_{\text{wmin}} = 813$ K is the minimal and $T_{\text{wmax}} = 883$ K is the maximal temperature of the GB wetting phase transi-

tion in the Al–Mg system. Assuming that the bulk solidus and bulk liquidus does also hold for GB phases at their interface, the respective tie-lines at T_{wmin} and T_{wmax} have been drawn in the two-phase (S+L) area of the Al–Mg bulk phase diagram (Fig. 5.4).

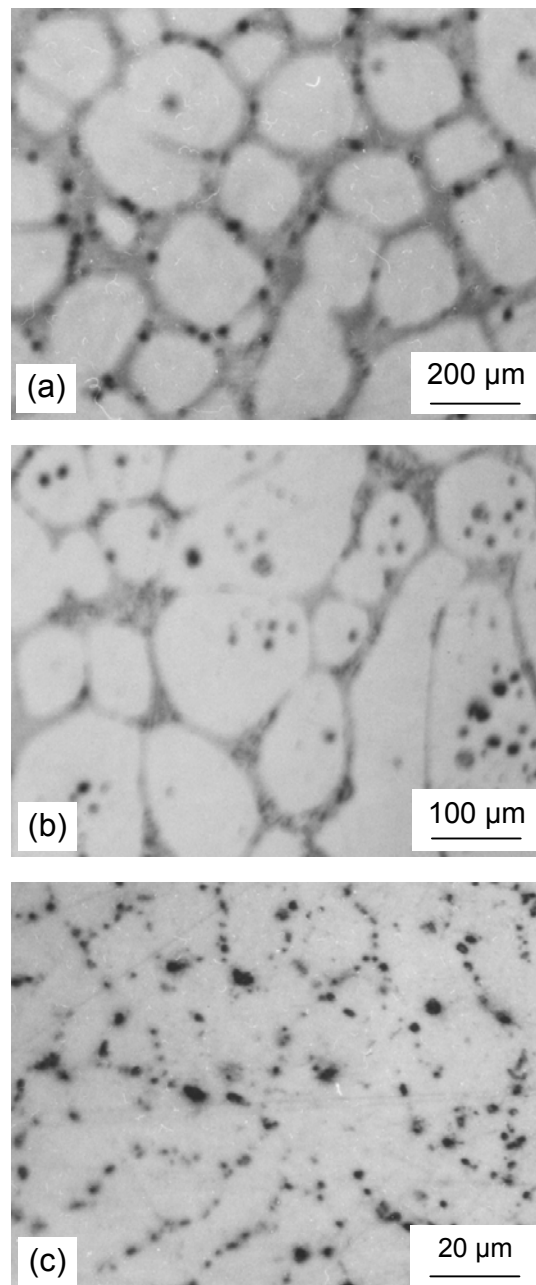


Fig. 5.2. Optical micrographs of samples annealed at 883 K (a), 853 K (b) and 803 K (c) for 1 h.

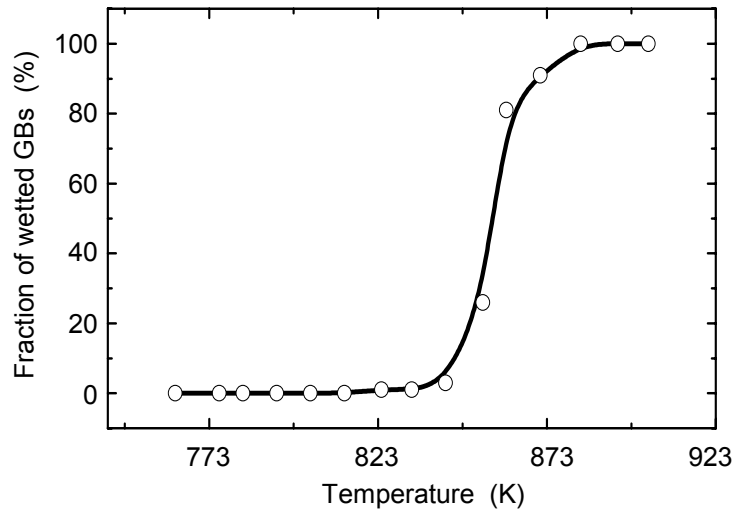


Fig. 5.3. Temperature dependence of the fraction of wetted GBs in the Al–Mg system.

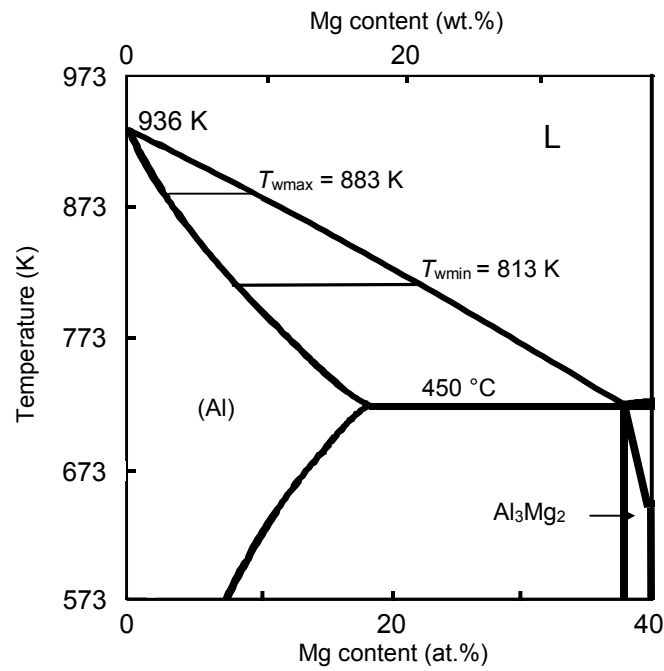


Fig. 5.4. Al–Mg equilibrium phase diagram [102] and the tie-lines of GB wetting phase transitions (thin lines).

Obviously the presence of a liquid phase at GBs will affect critically the deformation characteristics of the alloy. Studying pure shear of a commercial Al-5 wt.% Mg alloy Iwasaki et al. [103] found that the shear strain to failure drops drastically at the solidus temperature. Above the solidus temperature in the two-phase area (S+L) the shear strain to failure is about six times lower than in the pure solid solution.

Now, having observed that wetting of GBs occurs in the bulk (S + L) two-phase region of the Al–Mg system, it may be suggested that a *premelting* (or *prewetting*) of GBs may also occur in the (Al) single-phase region near the bulk solidus line. Due to this phenomenon a thin liquid-like layer, which is not stable in the bulk, can be formed at the GBs [92,104]. This kind of GB phase transitions has previously been observed for other systems and may be described by the so-called GB solidus line [25,84–87,92,104–107].

The extraordinary high-strain rate superplasticity phenomenon was observed in nanostructured ternary Al–Mg–X alloys and nanostructured metal–matrix composites with an Al–Mg–X matrix [96–101,108–111]. The maximal elongation to failure increases drastically from 200–300 % up to 2000–2500 % in a very narrow temperature interval of about 10 degrees *just below the respective solidus temperature*. This phenomenon is technologically important not only due to the extremely high elongation to failure, but also due to the high strain rate (up to 10^2 s^{-1}) which is many orders of magnitude higher than that of conventional superplasticity (between 10^{-2} and 10^{-5} s^{-1}). Until now no satisfactory explanation has been offered for this phenomenon as observed in Al–Mg–X alloys in a narrow temperature interval below the solidus temperature.

It is suggested here that GB *prewetting* (or *premelting*) is responsible for high-strain rate superplasticity. In that case, the GBs would be covered by a liquid-like thin layer, leading to an enhanced plasticity of the nanos-

structured polycrystals. Using this hypothesis, one may evaluate existing observations. Such results for the Al–Mg–Zn system have been reported in Refs. [100,101,108–111]. Analysis of the micrographs published in Refs. [100,101,108,109] shows that GB wetting proceeds also in ternary Al–Mg–Zn alloys. From these micrographs it is possible to estimate $T_{wmax} = 808$ K for technical 7xxx Al–Mg–Zn alloys (see the pseudo-binary phase diagram in Fig. 5.5). The addition of Zn to Al–Mg alloys apparently lowers T_{wmax} in comparison with the binary Al–Mg alloys (cf. Fig. 5.4). At 748 K about 50 % of GBs are still wetted (see $T_{w50\%}$ tie-line in Fig. 5.5). Unfortunately, the micrographs of the Al–Mg–Zn alloys published in Refs. [100,101,108,109] do not permit us to estimate $T_{wmin} < T_{w50\%}$. Additionally, most of the data points lie a short distance underneath the bulk solidus and also the maximal elongation to failure was observed below the bulk solidus [100, 101,108–111]. This indicates that *prewetting* (or *premelting*) is indeed responsible for the high-strain rate superplasticity in also these alloys.

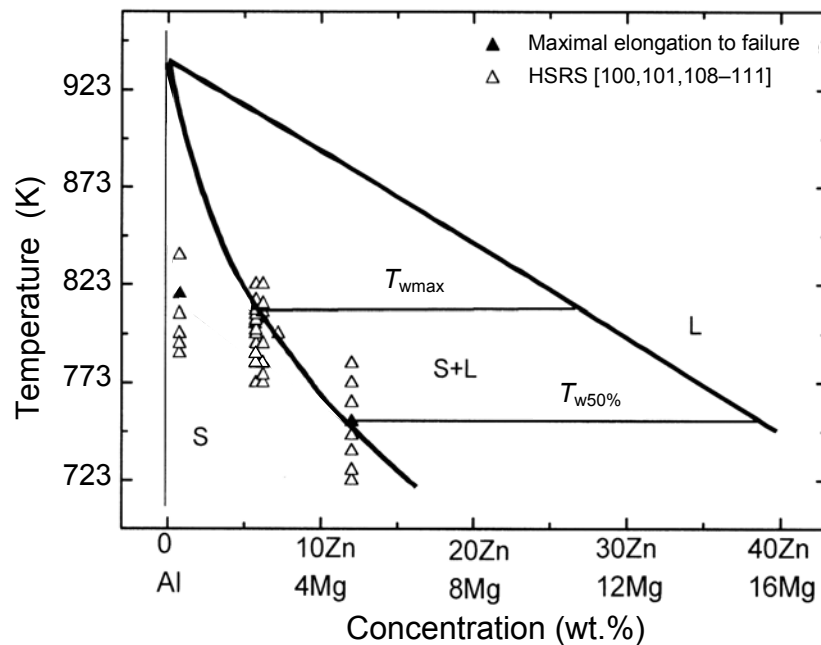


Fig. 5.5. Pseudo-binary phase diagram for 7xxx Al–Mg–Zn alloys (thick lines), containing GB wetting phase transition lines (thin lines). HSRS = high-strain rate superplasticity.

5.4. Conclusions

The Al–Mg system exhibits grain-boundary wetting. On the basis of grain-boundary wetting data the maximal and minimal temperatures, $T_{w\max}$ and $T_{w\min}$, of grain-boundary wetting phase transitions have been indicated and the corresponding tie-lines in the two-phase (S + L) region of the respective bulk phase diagram can be drawn. The occurrence of the grain-boundary *prewetting* (or *premelting*) can be considered as the origin of high-strain rate superplasticity upon deformation.

6. Grain-boundary wetting by a solid phase: microstructural development in a Zn-5 wt.% Al alloy

G.A. López, E.J. Mittemeijer and B.B. Straumal*

* *Institute of Solid State Physics, Russian Academy of Sciences, Chernogolovka, Moscow District, Russia*

Abstract

A systematic study of grain-boundary wetting by a solid phase was carried out for the first time. The microstructure of Zn-5 wt.% Al polycrystals was studied in the temperature range 523–648 K. The Al-rich phase formed either chains of separated lens-like precipitates or continuous layers at the Zn-rich phase/Zn-rich phase grain boundaries upon annealing at different temperatures. The contact angle at the intersection between the Al-rich phase/Zn-rich phase interphase boundaries and the Zn-rich phase/Zn-rich phase grain boundary decreased with increasing temperature. It became zero at a certain temperature, and remained zero above this *solid-state wetting temperature*, i.e., a continuous Al-rich phase layer covered the Zn-rich phase/Zn-rich phase grain boundaries. The fraction of wetted grain boundaries increased with increasing temperature and was independent of annealing time. The growth of the Al-rich phase at the grain boundaries is controlled by volume diffusion in the matrix phase.

6.1. Introduction

Decomposition of supersaturated solid solutions is a very important process occurring upon heat treatment of materials, because thereby the microstructure of the alloy can be changed and thus the properties of the material can be controlled.

Precipitation at grain boundaries (GBs) can occur easier than in the bulk, because the reduction of GB area and thus GB energy favours nucleation [112]. Two morphologies may be distinguished for second-phase (β) particles at a GB in the matrix (α):

1. If the GB energy of grains in the matrix α per unit area, $\sigma_{GB}^{\alpha\alpha}$, is smaller than two times the energy per unit area of the α/β inter-phase boundary (IB), $\sigma_{IB}^{\alpha\beta}$, formed upon precipitation of the β particle on the α/α GB, then the growing α particle tends to reduce its surface, and develops a lens-like shape characterized by a contact angle θ (see Fig. 6.1d). If the surface tensions at the junction the GB and the IBs are balanced (in “equilibrium”), it holds $\sigma_{GB}^{\alpha\alpha} = 2\sigma_{IB}^{\alpha\beta} \cos(\theta/2)$ [113].
2. If $\sigma_{GB}^{\alpha\alpha} > 2\sigma_{IB}^{\alpha\beta}$, the growing β particle tends to increase its surface: a layer of β -phase covers continuously (“wets”) the α/α GB (Fig. 6.1e). In other words: the α/α GB is unstable in contact with the growing β particle and the “equilibrium” (see above) contact angle θ is nil.

Layers of solid second phases fully covering the GBs in a matrix have been observed in many systems. Important examples are Fe_3C layers at GBs in ferritic and austenitic steels [114,115], layers of Cu at GBs in sinte-

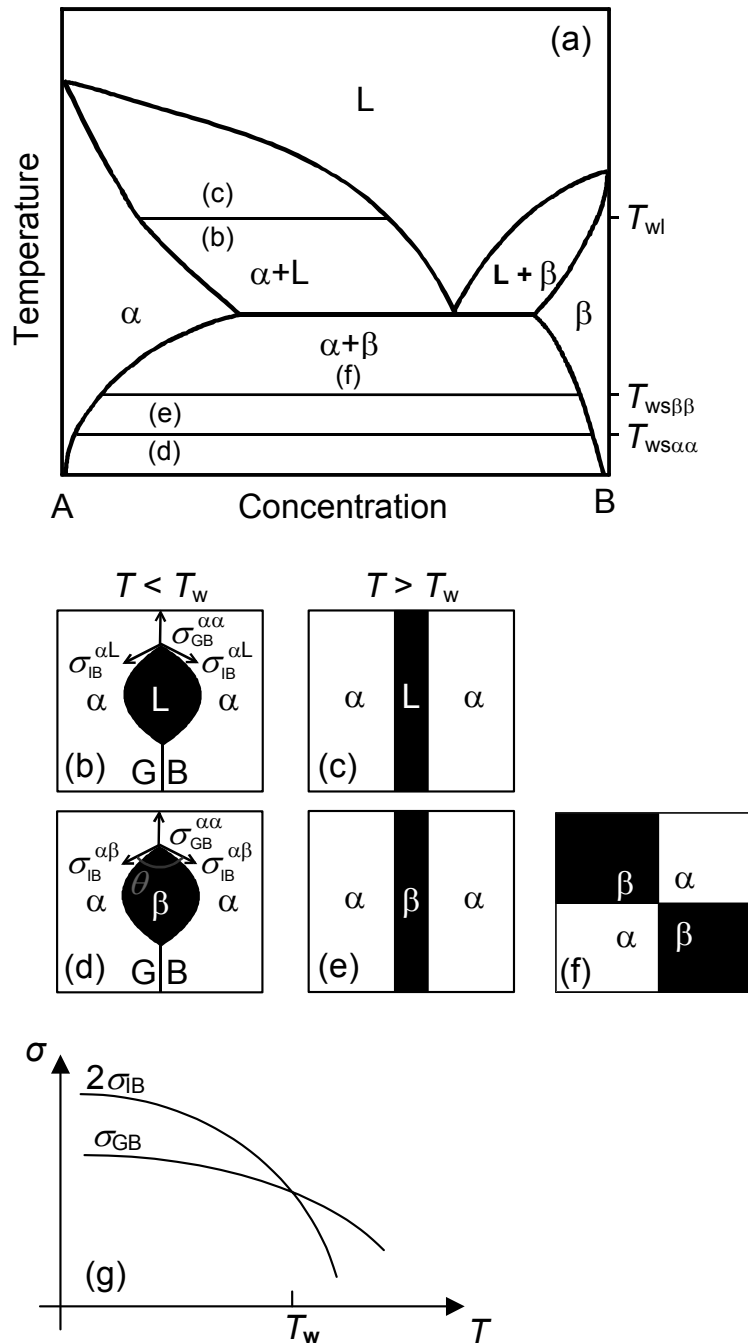


Fig. 6.1. (a) Schematic phase diagram showing tie-lines of GB wetting by a liquid phase and of GB wetting by a solid phase at T_{wl} , and $T_{ws\alpha\alpha}$ and $T_{ws\beta\beta}$, respectively. (b) Liquid phase L does not wet a GB in the solid phase α ($T < T_w$). (c) Liquid phase L wets a GB in the solid phase α ($T > T_w$). (d) Solid phase β does not wet a GB in the solid phase α ($T < T_{ws\alpha\alpha}$). (e) Solid phase β wets a GB in the solid phase α ($T > T_{ws\alpha\alpha}$). (f) Only α/β IBs exist in an ($\alpha+\beta$) polycrystal if wetting occurs at both α/α and β/β GBs ($T > T_{ws\beta\beta}$). (g) Schematic dependencies of σ_{GB} and $2\sigma_{IB}$ on temperature. The point of intersection indicates the wetting temperature, T_w .

red W polycrystals [116–119], α -Zr layers at GBs of β -(Zr, Nb) [120] and Bi layers at GBs in Cu [121]. Such continuous GB layers of a solid second phase can have either detrimental effects (e.g. enhanced brittleness) or favourable effects (e.g. improved plasticity).

The GB wetting (covering) by a layer of a *solid* second phase is analogous to the conventional GB wetting by a *liquid* second phase [84,87,89,90,122–125]: cf. Figs. 6.1b, c and 6.1d, e. The value of the temperature is decisive for the occurrence of wetting. With increasing temperature both the GB energy σ_{GB} and the IB energy σ_{IB} decrease normally. If, at sufficiently low temperature $2\sigma_{\text{IB}} > \sigma_{\text{GB}}$ and, upon increasing temperature, the temperature dependencies $\sigma_{\text{GB}}(T)$ and $2\sigma_{\text{IB}}(T)$ intersect (Fig. 6.1g), then a GB wetting proceeds at the temperature T_w of intersection and at temperatures higher than T_w (cf. points 1 and 2 above). Starting from a relatively low temperature, upon increasing the temperature the contact angle θ decreases down to $\theta = 0$ at T_w . Above T_w the contact angle remains $\theta = 0$ (Fig. 6.1c and e). The *tie-line of GB wetting*, i.e., the tie-line connecting the phases in equilibrium at T_w , can be drawn in the two-phase regions ($\alpha + L$) and ($\alpha + \beta$) of the phase diagram for the cases of liquid and solid GB wetting (Fig. 6.1a). At and above this tie-line the second, *liquid* or *solid*, phase forms a layer separating the crystals. GBs with a relatively low energy possess a relatively high T_w . In polycrystalline materials a spectrum of GBs with different energies exists. Therefore, in polycrystals a range of T_w values occurs: from $T_{w\text{min}}$ to $T_{w\text{max}}$. Corresponding tie-lines at $T_{w\text{min}}$ and $T_{w\text{max}}$ for wetting by a liquid phase have been presented in the Al–Sn, Al–Mg and Al–Zn phase diagrams [90,124,125]. Above $T_{w\text{max}}$ all GBs are completely wetted. At temperatures between $T_{w\text{min}}$ and $T_{w\text{max}}$ only a fraction of the total number of GBs is wetted. Below $T_{w\text{min}}$ all GBs are not wetted, and the second phase appears at the GBs only as (chains of) isolated particles. Peculiar electrical and mechanical properties of materials can be caused by a layer of a second phase fully covering the GBs. This

has relevance especially for nanocrystalline materials that have a large volume fraction of GBs. Tie-lines as mentioned can then be very useful with a view to practical applications.

The wetting phenomenon, although described above deliberately in a general way, has until now been discussed and observed in the literature with respect to wetting by a *liquid* phase. The purpose of this contribution is to demonstrate that wetting by a solid phase can occur and be explained on the basis of the same thermodynamic background. The following predictions can thus be made in advance:

- *Transition* from incomplete coverage (wetting) of a single GB by a solid second phase to complete coverage (wetting) of that GB with increasing temperature at a certain, solid-state wetting temperature, T_{ws} ;
- Dependence of T_{ws} on the GB energy (low T_{ws} for high σ_{GB}^{aa} and vice versa);
- Increase of the fraction of GBs covered by a solid phase from 0 to 100 % with increasing temperature from T_{wsmin} to T_{wsmax} .

These phenomena of solid-phase wetting have been studied and discussed, for the first time, in this work. To this end the Al–Zn system has been chosen. For this system the occurrence of conventional liquid-phase wetting was shown recently for the two-phase ((Al) + L) region of the Al–Zn phase diagram [125]. The current study demonstrates the occurrence of solid-phase wetting and, as a final result, provides the tie-line for first occurrence of solid-phase wetting in the Al–Zn phase diagram.

6.2. Experimental details

A Zn-5 wt.% Al alloy was produced by melting the corresponding amounts of Zn (99.999 wt.%, Hereaus) and Al (99.9995 wt.%, VAW Aluminium AG), and subsequent cooling down under vacuum (residual pressure of about 10^{-5} Pa). Slices (2 mm thick) of the alloy were prepared by sawing, grinding and chemical etching for 15 s (using a 5 wt.% HF aqueous solution). Next, these samples were sealed in evacuated silica ampoules (residual pressure of approximately 10^{-4} Pa) and annealed in a tube furnace at several temperatures between 523 and 648 K (see Fig. 6.2) for 336, 672 and 2016 h (temperature control within 1 degree). Thereafter the specimens were quenched by crushing the ampoules in water.

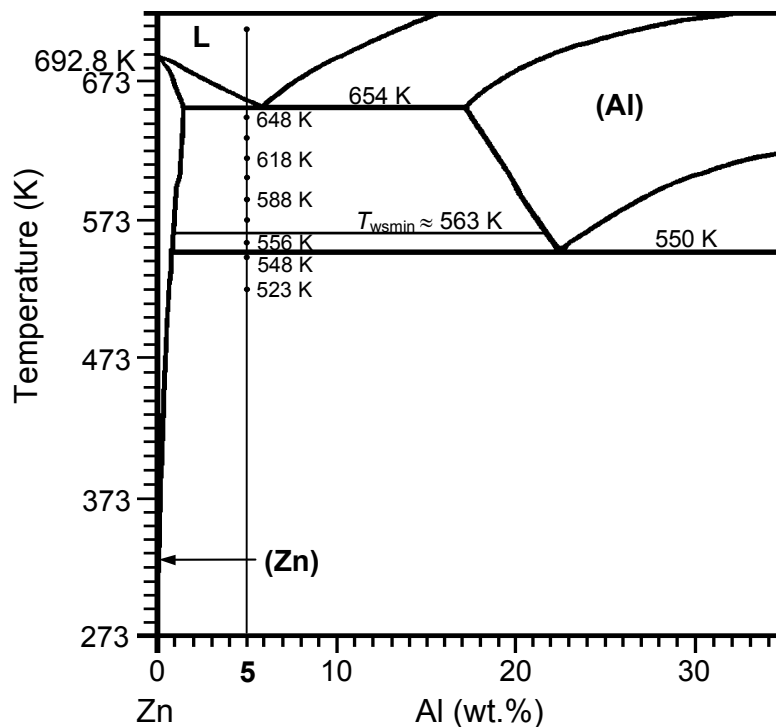


Fig. 6.2. The Zn–Al equilibrium phase diagram [19]. The vertical thin line represents the Zn-5 wt.% Al alloy of this study. Points at that line represent the annealing temperatures applied. The tie-line at $T_{wsmin} \approx 563$ K represents the minimal temperature determined in this work for wetting of Zn-rich phase/Zn-rich phase GBs by the Al-rich phase.

The microstructure of the specimens was studied by optical microscopy (microscope Zeiss Axiophot) and scanning electron microscopy (field emission microscope JEOL JSM 6300 F). For the metallographic investigations the samples were etched for 15 s with a 5 wt.% HF aqueous solution.

The quantification of the wetted GBs by light microscopical analysis was performed adopting the following criterion: every GB was considered to be wetted only when a continuous layer had covered the whole (visible part of the) GB; if such a layer appeared to be interrupted, the GB was regarded as a non-wetted GB. At least 100 GBs were analysed at each temperature. In addition, using an imaging software (ProImage 3.20) the thicknesses of the second phase at the GBs were measured to investigate the growth kinetics. The average thickness value from 40–50 measurements and the corresponding standard deviation were determined for every annealing time (see above) at 523, 548, 556, 618 and 648 K. The accuracy of these kinetic data would be enhanced by applying longer annealing times at the temperatures mentioned, but the relative slowness of the process makes this impossible for a practical period of time of investigation (longest annealing time applied was 2016 h).

To confirm the presence of the different phases X-ray diffraction patterns were taken from cross-sections of the samples. The data were recorded employing a Philips X'Pert MPD diffractometer equipped with a graphite monochromator applying Co K_{α} radiation. The data were acquired in the diffraction angle range $20 - 120^{\circ}$, with a step width of 0.05° and a step time of 25 s. To identify the phases the characteristic peaks were compared with those given in the database of the International Centre for Diffraction Data (see cards 89–4037 for Al and 87–0713 for Zn). In addition, the reflection positions were determined by peak fitting with symmetric pseudo-Voigt functions (PROFIT; Sonneveld & Delhez, 1996). From these data the lattice parameters were determined for both phases.

The measurement of the chemical composition of the phases was carried out using electron probe microanalysis (Cameca SX100 instrument equipped with 5 wavelength-dispersive spectrometers). The measurements were performed at an accelerating voltage of 15 kV, a beam current of 20 nA and a take-off angle of 40°. The time per single point measurement was 60 s. The intensities of the K_{α} X-ray lines were taken as the difference between the peak maxima and the background intensities at the left and right sides of the peaks using thallium acid phthalate (for Al) and large-area LiF (for Zn) crystals as monochromators. The measured Al K_{α} and Zn K_{α} intensities were divided by those of pure Al and Zn standards, respectively. Then the composition was calculated from the corresponding intensity ratios applying the approach described in Ref. [127]. For the determination of the concentration profiles the electron beam was moved along a straight line on the specimen cross-sections with intervals from 1 to 5 μm between the locations for point measurements.

6.3. Results and discussion

6.3.1. *As-cast microstructure*

The as-cast microstructure of the as-prepared Zn-5 wt.% Al alloy, i.e. after solidification and cooling down to room temperature, is shown in Fig. 6.3. Eutectic colonies of Al-rich phase and Zn-rich phase lamellae, formed at the eutectic temperature $T_e = 654$ K during solidification, can be observed clearly (Fig. 6.3a; see Fig. 6.2 for the Zn-rich part of the Al–Zn phase diagram). Electron probe microanalysis indicates the existence of (only) two phases in these alloys, namely the Al-rich and Zn-rich solid solutions. In the optical micrographs the Zn-rich phase appears with a light grey colour and the Al-rich phase appears with a dark grey colour (Fig. 6.3a). Since the composition of the studied alloy is very close to the eutectic one, al-

most no primary Zn-rich phase crystals are present in the samples. The volume fraction of the Zn-rich phase solid solution in the eutectic is much larger than that of the Al-rich solid solution, in accordance with the lever rule. Therefore, each eutectic colony can be conceived as a Zn-rich grain containing Al-rich lamellae, and thus neighbouring eutectic colonies are separated by Zn-rich phase/Zn-rich phase GBs. Practically no Al-rich phase/Al-rich phase GBs occurred as colony boundaries; the Al-rich lamellae of neighbouring eutectic colonies meet at the Zn-rich phase/Zn-rich phase GBs as two combs.

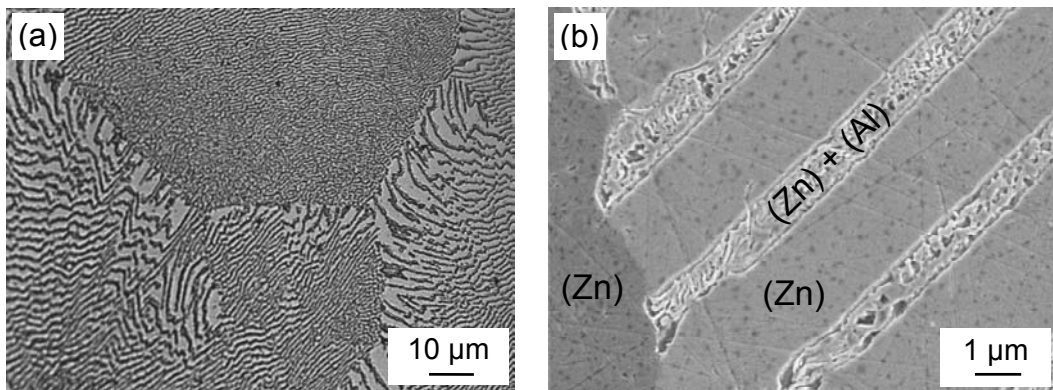


Fig. 6.3. Optical (a) and secondary-electron (b) micrographs of cross-sections of the as-cast Zn-5 wt.% Al alloy after cooling down to room temperature. A Zn-rich phase/Zn-rich phase GB is marked by arrows (b).

Upon casting, during the cooling to room temperature, a second (monotectoid) transformation proceeds at $T_{mt} = 550$ K in the Al-rich lamellae: the Al-rich solid solution with an Al content in the range of about 17–22 wt.% (cf. the phase diagram; Fig. 6.2) decomposes into an Al-richer solid solution (containing more than 67.6 wt.% Al [126]) and the Zn-rich solid solution. The corresponding, resulting fine structure of the parent eutectic Al-rich phase lamellae can be seen in Fig. 6.3b (see also Figs. 6.4c and 6.5a).

6.3.2. Morphology of the grain-boundary precipitation

Long-time annealings of the as-cast specimens at several temperatures between 523 and 648 K led to drastic changes of the initial microstructure. Typical microstructures of Zn-5 wt.% Al alloys annealed at 523, 556, 618 and 648 K are shown in Fig. 6.4. In all samples coarsening of the Al-rich phase lamellae had occurred in the bulk and Al-rich phase precipitates had grown at the Zn-rich phase/Zn-rich phase GBs. Note that after casting no precipitates were observed at the Zn-rich phase/Zn-rich phase GBs (see Fig. 6.3a and b). In Fig. 6.3b the Al-rich lamellae of the (former) eutectic microstructure are indicated as (Zn) + (Al). These solid solutions, (Zn) + (Al), formed by the monotectoid reaction at $T \leq 550$ K, are nearly pure Zn and pure Al, respectively, according to the phase diagram (Fig. 6.2). Upon heating of the as-cast specimens from room temperature to the annealing temperature, the Al-rich lamellae ((Zn) + (Al)) become a single Al-rich phase (again) after crossing the monotectoid temperature ($T_{mt} = 550$ K). The amount and composition of this Al-rich phase in the specimen may be approximately given by the equilibrium values at a temperature slightly above the temperature of the monotectoid reaction experienced during the preceding solidification (cf. Fig. 6.2 and Section 6.3.1 and results given in Section 6.3.3). Then, the (subsequent) annealing at $T_{mt} < T < T_e$ involves that the existing Al-rich phase has to adjust its composition by dissolution of Al in the surrounding Zn-rich phase and that new, additional Al-rich phase has to be formed, as follows from the phase diagram (Fig. 6.2). Against this background the development of Al-rich phase at the Zn-rich phase/Zn-rich phase GBs can then be understood as driven by a favourable change in the (total) interfacial energy (cf. Section 6.1). Indeed, adjacent to the precipitates at Zn-rich phase/Zn-rich phase GBs a depleted, precipitate-free zone can be observed (Fig. 6.4a–d).

Two different kinds of morphologies have been observed for the precipitates at the Zn-rich phase/Zn-rich phase GBs, depending on the annealing temperature. Chains of more or less isolated precipitates are observed at GBs of a specimen annealed at the relatively low temperature of 523 K for 672 h (Fig. 6.4a). A continuous solid Al-rich phase layer covering certain GBs is observed in specimens annealed at relatively high temperatures (Fig. 6.4b).

A triple junction of Zn-rich phase/Zn-rich phase GBs is shown in Fig. 6.4c. The GB positioned horizontally is fully covered by a uniform Al-rich phase layer. The two GBs on the right-hand side of the micrograph are covered by chains of lens-like Al-rich phase precipitates. The contact angle θ for the precipitate particle and the GB of the latter type at the triple junction is about 86° (Fig. 6.4c; cf. Fig. 6.1d).

The temperature of annealing appears to be decisive if wetting can occur: even 2016 h of annealing at the relatively low temperature of 556 K did not lead to wetted GBs (Fig. 6.4d). To verify that the observations on solid-phase GB wetting do not depend on the pre-history of the specimen, specimens annealed at 523, 548 and 556 K were annealed additionally at 648 K. Note that after the anneals at 523, 548 and 556 K no covered GBs occurred (see Section 6.3.4 and Fig. 6.6). After the additional anneal at 648 K for 2 days covered GBs appeared indeed: the microstructure was the same as that shown in Fig. 6.4b. Also the fraction of covered GBs, determined as about 35 %, well agrees with the value obtained after annealing of as-cast samples directly at 648 K (Fig. 6.6). Hence, the temperature appears to be a state variable for GB wetting by a solid phase.

As expected, with increasing annealing time at constant temperature all kinds of Al-rich phase precipitates coarsen. The coarsening is more pronounced at higher temperatures (compare Fig. 6.4a and b). The Al-rich phase lamellae in the bulk become unstable, break up and start to spher-

oidize. If individual precipitates occur at the GBs, upon continued annealing at the same temperature they remain lens-like. The continuous Al-rich phase layers at the GBs thicken with increasing annealing time.

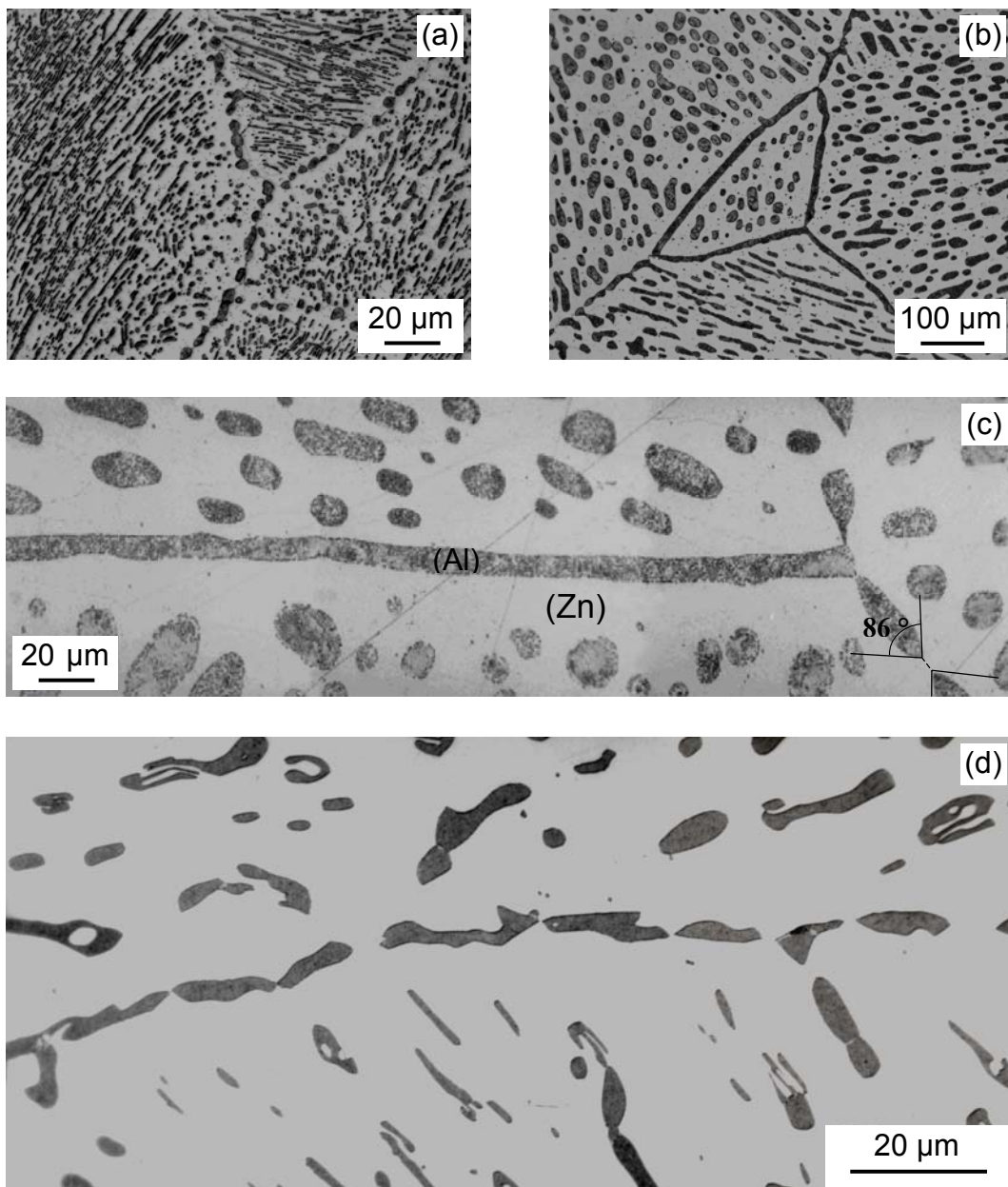


Fig. 6.4. Optical micrographs of the cross-sections of samples annealed for 672 h at 523 K (a), 648 K (b) and 618 K (c), and annealed for 2016 h at 556 K (d).

It can be concluded that GB wetting by a solid phase proceeds in the two-phase (Zn-rich phase/Al-rich phase) area of the Al–Zn bulk phase diagram confined by the eutectic and monotectoid temperatures, if the temperature is above a critical value.

6.3.3. Composition of the Al-rich and Zn-rich phases

The composition of the phases involved was determined by electron probe microanalysis. A concentration profile measured from a specimen annealed at 648 K for 672 h is shown in Fig. 6.5. The average composition of the Zn-rich solid solution (about 0.9 wt.% Al) as well as the overall composition of the (decomposed upon cooling, cf. Section 6.3.1) Al-rich solid solution (about 21 wt.% Al) correspond well with the equilibrium values for these phases at a temperature slightly higher than T_{mt} (Fig. 6.2), thereby supporting the discussion in Section 6.3.2. The fine microstructure due to the monotectoid decomposition of the Al-rich phase upon cooling is observed in Fig. 6.5a, and is revealed by oscillations in the concentration profile. X-ray diffraction patterns from samples annealed at 648 K for 672 and 2016 h were acquired. The calculated lattice parameters from the fitted patterns are close to those reported in the literature for pure Al and for pure Zn. These results are consistent with the results from the metallographic observations and from the electron probe microanalysis measurements, recognizing the decomposition of the Al-rich phase by monotectoid decomposition upon cooling after the anneal.

6.3.4. Quantification of the solid-phase wetting

The fraction of GBs fully covered by continuous layers of the Al-rich solid solution has been determined at each annealing temperature. A total of a-

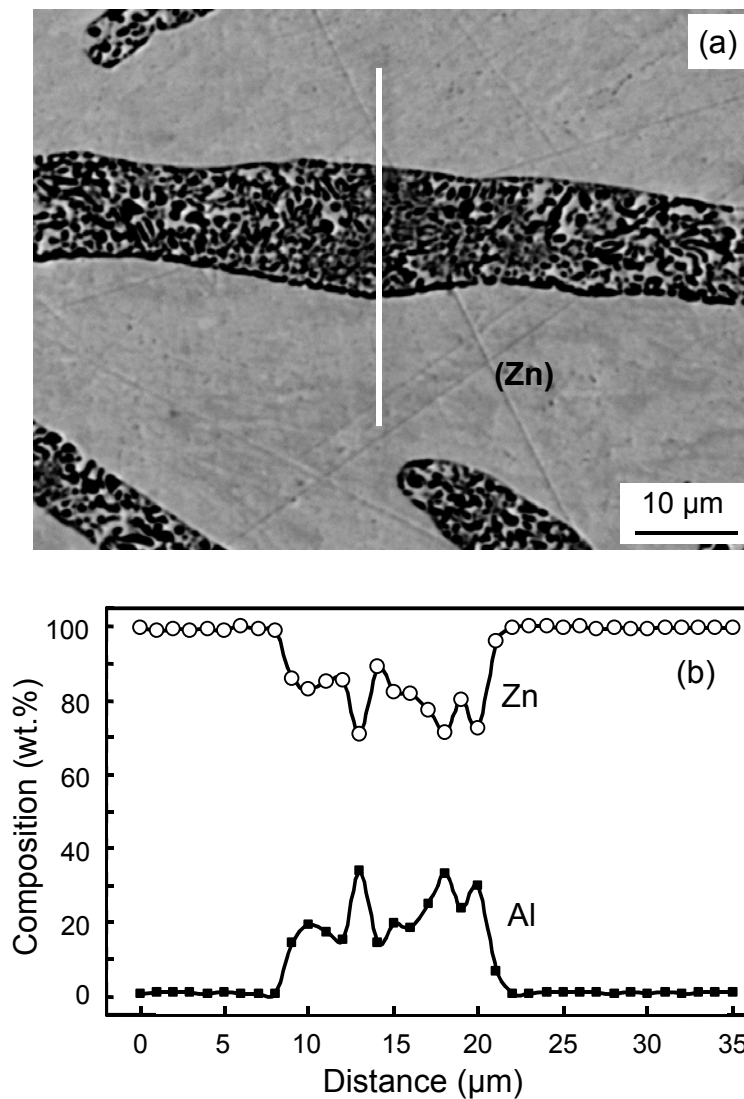


Fig. 6.5. Secondary-electron micrograph of a specimen annealed at 648 K for 672 h (a). Composition profile along the line indicated in the micrograph as determined by electron probe microanalysis (b).

bout 100 GBs was considered. The data obtained at the applied temperatures and annealing times have been gathered in Table 6.1. Evidently, the fraction of wetted GBs does *not* depend on annealing time at constant temperature. The temperature dependence of the fraction of GBs covered by a continuous layer of the Al-rich phase is shown in Fig. 6.6. The temperatures of the bulk monotectoid and eutectic transformations, T_{mt} and T_e ,

have been indicated. Below T_{mt} no GB was covered by a continuous layer of a solid phase (Fig. 6.4a). At $T = 556$ K ($>T_{mt}$) all GBs contain only chains of isolated Al-rich phase particles (Fig. 6.4d). At 573 K the first GBs occur which are completely covered by a continuous layer of the Al-rich phase. Hence, the minimal temperature of GB wetting by a solid phase, T_{wsmin} , for Zn-rich phase/Zn-rich phase GBs is in the range 556–573 K. The corresponding tie-line has been drawn in the phase diagram (Fig. 6.2). The fraction of covered GBs increases with increasing temperature. The fraction of covered GBs does not reach 100 %. Just below the eutectic temperature, T_e , the fraction of covered GBs equals only about 35 %. This implies that T_{wsmax} (see Section 6.1) is higher than T_e and no T_{wsmax} tie-line of complete solid-phase wetting can be indicated.

The increase in the fraction of wetted GBs with increasing temperature is indicative of the presence of GBs in the specimens with different GB energies. Even for a single GB the GB energy is not constant: differently oriented parts of a curved GB have different energies [128,129]. Thus, GBs could be found where parts with different orientations can be either completely (section AB in Fig. 6.7a) or incompletely (section BC in Fig. 6.7a) covered by the second solid phase.

Table 6.1. Fraction of Zn-rich phase/Zn-rich phase GBs wetted by the Al-rich phase.

T (K)	$t = 336$ h	$t = 672$ h	$t = 2016$ h
523	0	0	0
548	0	0	0
556	0	0	0
573	0.05	0.05	0.04
588	0.06	0.06	0.07
603	0.09	0.09	0.10
618	0.12	0.09	0.11
633	0.25	0.25	0.26
648	0.36	0.35	0.34

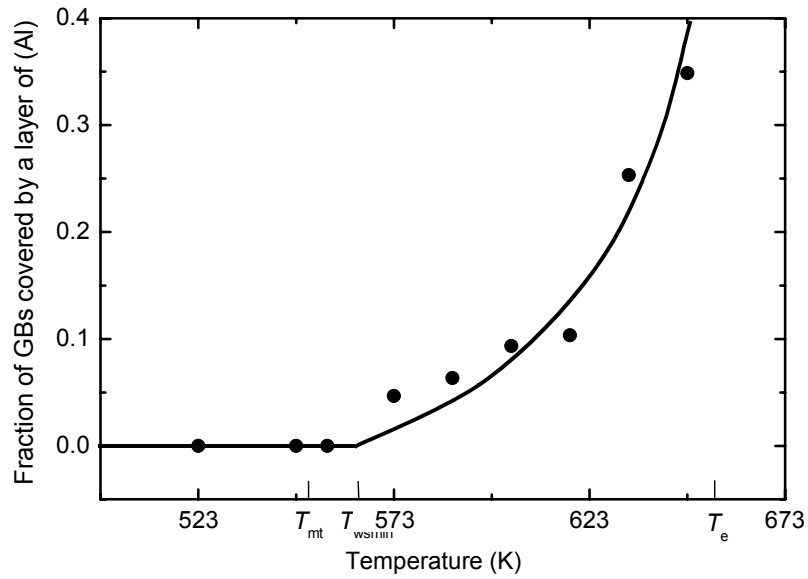


Fig. 6.6. Temperature dependence of the fraction of Zn-rich phase/Zn-rich phase GBs fully wetted by a continuous layer of the Al-rich phase. The temperatures T_{mt} and T_e of the bulk monotectoid and eutectic transformations have been indicated. T_{wsmin} is the minimal temperature of GB wetting by a solid phase. The data points for every temperature are averages of the data given in Table 6.1 for the different annealing times at each temperature.

The minimal value for the GB energy of a high-angle GB occurs for a twin GB. Therefore, twin GBs must have the highest possible critical temperature, T_{ws} . Twin plates in the Zn-rich phase (matrix) grains were recognized easily in the studied specimens using optical microscopy by applying polarized light. Indeed, even at the highest temperature studied (648 K) twin GBs were never covered with a continuous layer of the Al-rich phase (Fig. 6.7b). Furthermore, the contact angle θ at the intersection of the precipitate particle and the twin GB is close to 180° (Fig. 6.7b). Further, note that the Al-rich phase particles on the twin GB are not even elongated along the twin GB. For chains of particles on other GBs the value of θ is between 30 and 100° . Evidently, T_{ws} correlates with the GB energy: the lower σ_{GB}^{aa} , the higher T_{ws} .

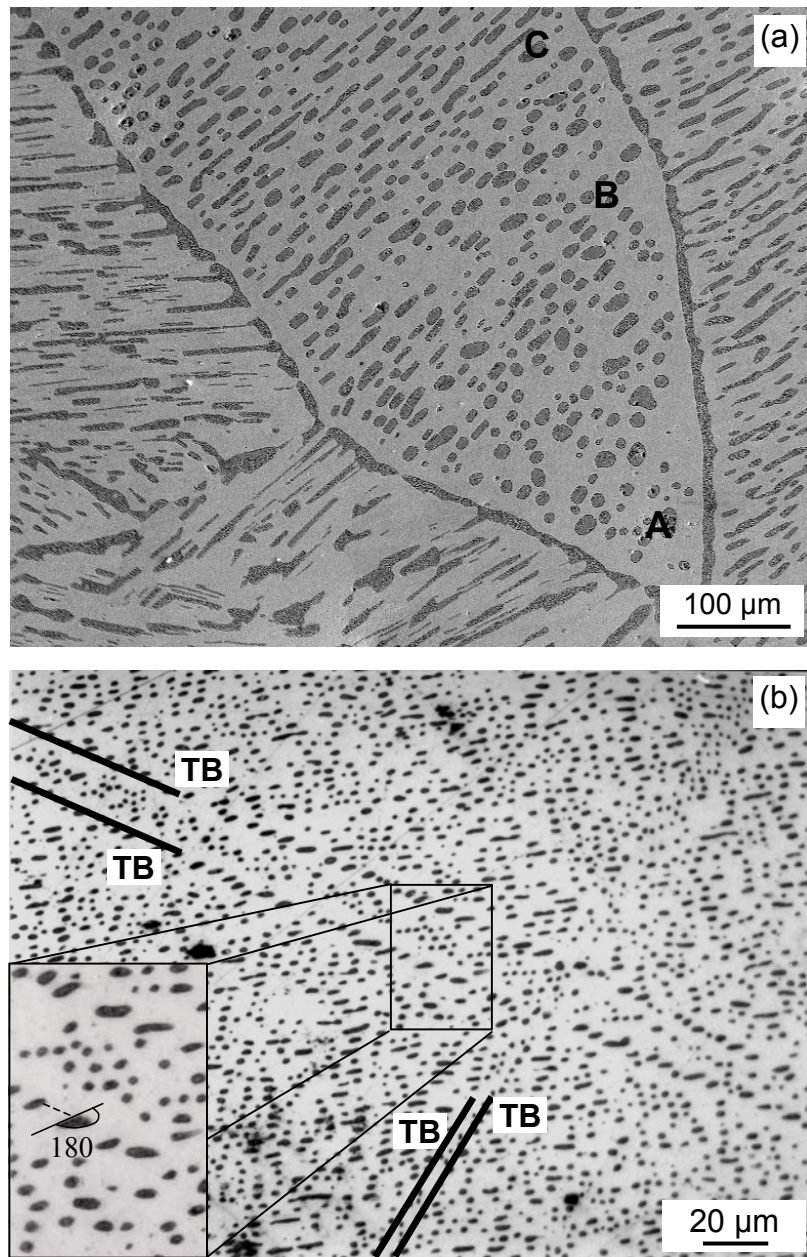


Fig. 6.7. (a) Curved Zn-rich phase/Zn-rich phase GB in a specimen annealed at 648 K for 672 h (optical micrograph). Due to the inclination dependence of GB energy, the section AB with (apparently) relatively high $\sigma_{GB}^{\alpha\alpha}$ is wetted by a continuous layer of the Al-rich phase, and the section BC with (apparently) relatively low $\sigma_{GB}^{\alpha\alpha}$ is occupied by a chain of Al-rich phase particles. (b) Twin GBs in the Zn-rich phase of a specimen annealed at 648 K for 336 h (optical micrograph). Due to the low GB energy of twin GBs, the twin boundaries are not wetted but are occupied by chains of Al-rich phase particles. TB = twin boundary.

6.3.5. Growth kinetics of the Al-rich phase formed at the GBs

The increase of the (average) thickness, L , of the Al-rich phase formed at the GBs was measured. Either chains of elongated lens-like precipitates ($T < T_w$) or layers ($T > T_w$) occur. In both cases L was determined as the average of 40–50 measurements. A parabolic growth for L was observed with increasing annealing time, t (e.g. see Fig. 6.8a). The kinetic growth parameter $k = L^2/t$, as determined from least-squares fitting of straight lines to the data in plots of L^2 vs. t for the temperatures investigated, increases exponentially with increasing temperature (i.e., Arrhenius behaviour occurs; see Fig. 6.8b). It follows that the kinetics of thickness growth of both the (isolated) elongated precipitates and the layers can be described by one and the same Arrhenius plot, implying that the corresponding thickness increases are controlled by the same mechanism.

The results shown in Fig. 6.8 indicate that the growth is controlled by a diffusion process: The activation energy, Q , was determined as 96 kJ/mol and the pre-exponential factor, k_0 , was found to be about $4 \times 10^{-9} \text{ m}^2/\text{s}$. For comparison, the Arrhenius plots for the self-diffusion coefficients, D , of Zn [130,131] are also shown in Fig. 6.8b (diffusion data on Al bulk diffusion in Zn are not available in the literature). The value of Q for (lateral) growth of the Al-rich phase at the GBs agrees very well with the Q values for bulk self-diffusion for the diffusion perpendicular and parallel to the crystal c -axis in Zn, (96 and 92 kJ/mol, respectively [131]). It is concluded that the thickness increase of the Al-rich phase formed at the GBs is controlled by volume diffusion in the Zn-rich phase.

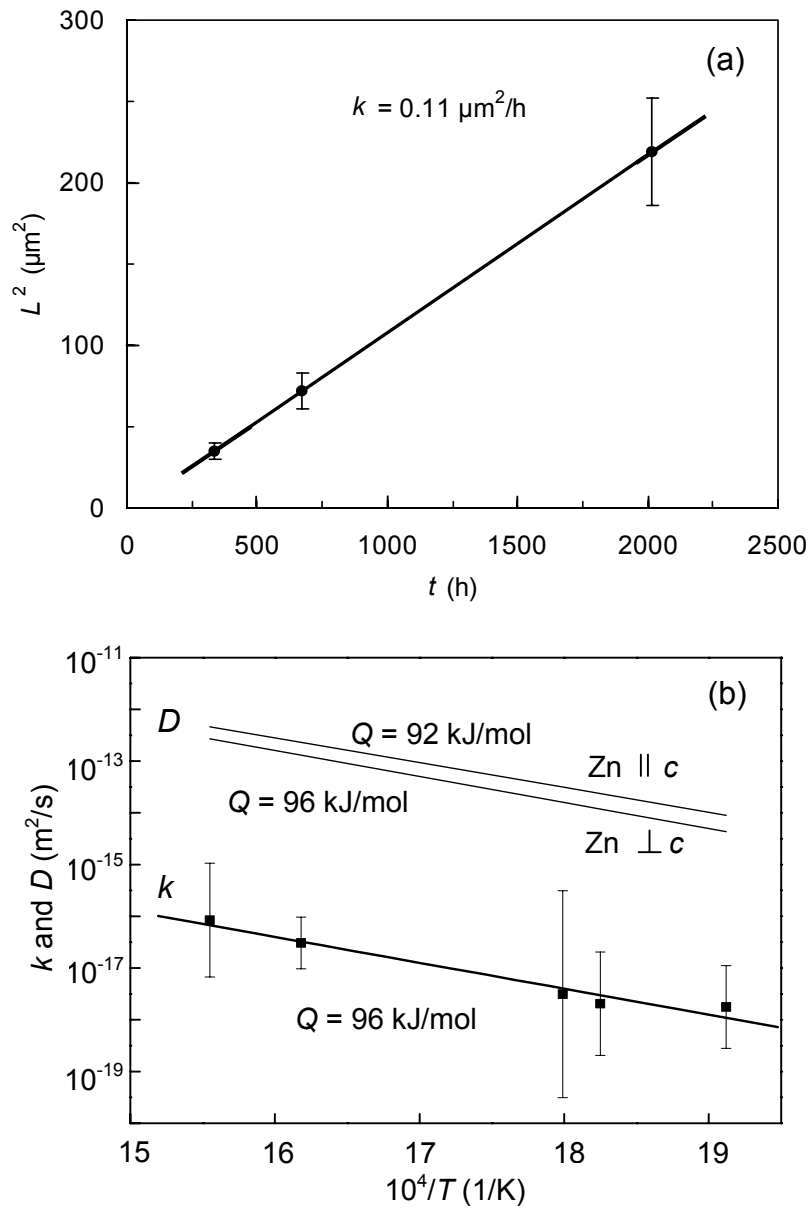


Fig. 6.8. (a) Parabolic growth of the thickness L of Al-rich phase formed at the GBs in specimens annealed at 648 K. (b) Arrhenius plot of the kinetic growth constant k . The data for the bulk self-diffusion coefficients of Zn perpendicular and parallel to the crystal c -axis (thin lines: [130,131]) are shown for comparison. The variation of the k values as indicated in Fig. 6.8b follows from the possible variations in k as determined from least-squares fittings as that shown in Fig. 6.8a.

6.4. Final remark

An important difference between GB wetting by a liquid phase and GB wetting by a solid phase can be indicated. In general, in a two-phase ($\alpha + \beta$) region of a (binary) phase diagram α/α , β/β and α/β interfaces can occur. The composition of the binary Zn–Al alloy of this study was such that in the two-phase region analysed (see Fig. 6.2) β/β (i.e. Al-rich phase/Al-rich phase) GBs were practically not observed (see Section 6.3.1). Now consider an alloy of such a composition that a relatively large amount of β -phase occurs in the ($\alpha + \beta$) area. Then a relatively large amount of β/β GBs can be present. The β/β GBs can in principle also exhibit wetting: wetting by a solid α -phase. Generally, $T_{ws\beta\beta}$ will not be the same as $T_{ws\alpha\alpha}$. Hence, two kinds of GB wetting tie-lines can be drawn in the two-phase ($\alpha + \beta$) area of the phase diagram: one at $T_{ws\alpha\alpha}$ for wetting of α/α GBs by the β -phase and one at $T_{ws\beta\beta}$ for wetting of β/β GBs by the α -phase (Fig. 6.1a).

If $T_{ws\alpha\alpha} < T_{ws\beta\beta}$, upon increasing the temperature α/α GBs will be first wetted by the β -phase and when the temperature is higher than $T_{ws\beta\beta}$ β/β GBs will be wetted by the α -phase. Eventually, at sufficiently high temperature, only α/β GBs are stable in the polycrystal. This must lead to a configuration of α and β based on the alternating principle as exhibited by the light and dark fields on a chess-board (Fig. 6.1f).

6.5. Conclusions

- The transition from incomplete coverage of Zn-rich phase/Zn-rich phase grain boundaries by an Al-rich solid phase to complete wetting of the grain boundary by a continuous Al-rich phase layer oc-

curs upon increasing the temperature at a critical temperature of solid-state wetting, T_{ws} .

- The critical temperature T_{ws} is different for grain boundaries and grain-boundary areas with different energies: T_{ws} decreases for increasing grain-boundary energy.
- The tie-line for the minimal temperature of wetting by a solid phase, T_{wsmin} , was determined for the Zn-rich phase/Al-rich phase two-phase area of the Al–Zn phase diagram confined by the monotectoid temperature, T_{mt} , and by the eutectic temperature, T_e . T_{wsmin} in the Zn–Al system lies slightly above T_{mt} .
- T_{wsmax} in the Zn–Al system lies above the temperature of the eutectic transformation, T_e .
- The fraction of grain boundaries wetted by a solid phase depends only on the temperature and not on the annealing time, and increases from 0 to about 35 % with increase of temperature from T_{wsmin} to T_e .
- The thickness of the Al-rich phase formed at the grain boundaries is controlled by volume diffusion in the Zn-rich phase.

7. Kurzfassung der Dissertation in deutscher Sprache

7.1. Einleitung

Die Eigenschaften von Materialien werden nicht nur von der chemischen Zusammensetzung, sondern weitgehend durch den Gefügestand bestimmt. Heutzutage ist das Hauptziel der modernen Werkstoffwissenschaft, die Materialien hinsichtlich Kosten und Leistung zu optimieren.

Um dieses Ziel zu erreichen, kann das Verständnis von Phänomenen, die an Korngrenzen und freien Oberflächen auftreten, besonders wichtig sein. Zu diesen Vorgängen gehören die Korngrenzen- und Oberflächen-segregation, die diskontinuierliche Ausscheidung sowie die Benetzung von Korngrenzen. Sie sind Gegenstand dieser Dissertation.

Ein besonderes Ziel dieser Arbeit war es, die Korngrenzen- und Oberflächensegregation im System Cu–Bi unter identischen Bedingungen vergleichend zu untersuchen. Dies gelang durch ein besonderes Herstellungsverfahren von Zweikristallen, die im *Probeninneren* freie Oberflächen aufwiesen. Nach Auslagerung der Proben bei Temperaturen zwischen 1073 und 1223 K wurde die Segregation von Bi an der Korngrenze und freien Oberfläche orientierter Cu-Zweikristalle gemessen. Erstmals wurde die Segregation von Bi an freien Oberflächen von Cu unter Gleichgewichtsbedingungen bestimmt; sie ist deutlich stärker als an Korngrenzen.

Ferner wurden im System Cu–C erstmals zuverlässige Daten zur Löslichkeit von C in festem Cu ermittelt. Dank eines sehr präzisen Analyseverfahrens wurde der C-Gehalt der ausgelagerten Proben mit einer Genauigkeit von ± 0.1 Gew.-ppm bestimmt. Die ermittelten Werte sind 50 mal kleiner als die in der Literatur veröffentlichten Daten zur Löslichkeit von C in festem Cu.

In einer Cu-4.5 At.-% In-Legierung wurde erstmals eine lokale Analyse der Wachstumskinetik der diskontinuierlichen Ausscheidungsreaktion die Diffusivität individueller Korngrenzen bestimmt. Besondere Aufmerksamkeit wurde der Bestimmung der in der entmischten Matrix verbleibenden Konzentrationsgradienten gewidmet. Die bestimmten Korngrenzendiffusivitäten belegen, dass sich wandernde und stationäre Korngrenzen im Diffusionsvermögen nicht wesentlich unterscheiden.

In den Systemen Al-Mg und Zn-Al wurde das Benetzungsverhalten von Korngrenzen gezielt metallographisch untersucht. Die konventionelle Korngrenzenbenetzung durch eine *flüssige* Phase wurde im System Al-Mg zum ersten Mal untersucht. Hierzu wurden Proben im Zweiphasengebiet des Zustandsdiagramms bei unterschiedlichen Temperaturen ausgelagert. Mit steigender Temperatur wurde ein Übergang von nicht-benetzen Korngrenzen zu benetzten Korngrenzen beobachtet. Die Temperaturen, bei denen 0 und 100 % der Korngrenzen benetzt sind, wurden bestimmt und in das Zustandsdiagramm als zusätzliche Linien eingezeichnet. Aus diesen Ergebnissen wurde das Auftreten einer Vorbenetzung der Korngrenzen im einphasigen Bereich des Zustandsdiagramms vorgeschlagen als Erklärung für das enorme superplastische Verhalten von Al-Basis-Legierungen.

Ferner wurde zum ersten Mal die Korngrenzenbenetzung durch eine *feste* Phase untersucht. Hierzu wurde die Gefügeentwicklung in einer Zn-5 Gew.-% Al-Legierung in Abhängigkeit von der Temperatur beobachtet. Die Bildung einer Schicht oder isolierter Teilchen einer zweiten festen Phase an den Korngrenzen wurde quantitativ bestimmt. Die Temperatur, bei der die Benetzung 0 % beträgt, wurde bestimmt und in das Zustandsdiagramm eingetragen.

7.2. Korngrenzen- und Oberflächensegregation im System Cu–Bi

Unter Segregation an Grenzflächen versteht man die Anreicherung von Fremdatomen einer Legierung an Korngrenzen und freien Oberflächen. Die Eigenschaften eines Materials, wie z.B. die Sprödigkeit, können von der Segregation stark beeinflusst werden [4–6]. Um dieses Phänomen zu untersuchen, ist die Auger-Elektronenspektroskopie eine sehr geeignete Untersuchungsmethode [7].

Obwohl Segregation an Korngrenzen und freien Oberflächen in vielen Systemen erforscht wurde [4–6,8–11], liegen nur in wenigen Fällen systematische Vergleiche vor. Ob die Anreicherung an freien Oberflächen oder an Korngrenzen stärker ist, wurde bislang nicht eindeutig geklärt. Eine Hypothese ist, dass versprödende Atome stärker an freien Oberflächen segregieren und Fremdatome, die ein Material duktiler machen, stärker an Korngrenzen angereicht werden [20–22]. Um zur Klärung dieser Frage beizutragen, wurden die beiden Segregationsarten erstmals unter identischen Versuchsbedingungen studiert.

Es wurden hierzu Cu-Zweikristalle mit Hohlräumen hergestellt (Bild 7.1). Proben aus diesen Zweikristallen wurden mit Bi dotiert, bei 1223 K für 240 h homogenisiert und dann bei Temperaturen zwischen 1073 und 1173 K bis zur Gleichgewichtssegregation ausgelagert. Dank dieser Hohlräumen konnte – trotz des hohen Dampfdrucks von Bi – die Abdampfung von Bi-Atomen aus der segregierenden Oberflächenschicht vermieden werden. Die Bi-Anreicherung an beiden Grenzflächenarten wurde durch Auger-Elektronenspektroskopie auf der Bruchfläche der Proben gemessen.

Ein besonderes Verdienst dieser Arbeit ist es, dass der Vergleich der Segregation an Korngrenzen und freien Oberflächen unter Gleichgewichtsbedingungen erfolgte. Wie im Bild 7.2 dargestellt, segregiert Bi deutlich stärker an freien Oberflächen als an Korngrenzen.

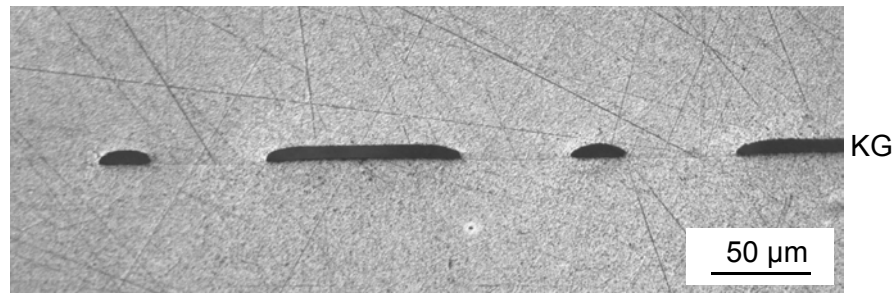


Bild 7.1. Lichtmikroskopische Aufnahme (Querschliff) eines symmetrischen {331}-Zweikristalls. Die Hohlräume entlang der Korngrenze (KG) wurden photolithographisch an einer der beiden Einkristallscheiben hergestellt, bevor sie durch Diffusionsverschweißen miteinander verbunden wurden. Die Hohlräume haben eine Höhe von $\approx 12 \mu\text{m}$ und einen Durchmesser von $\approx 100 \mu\text{m}$.

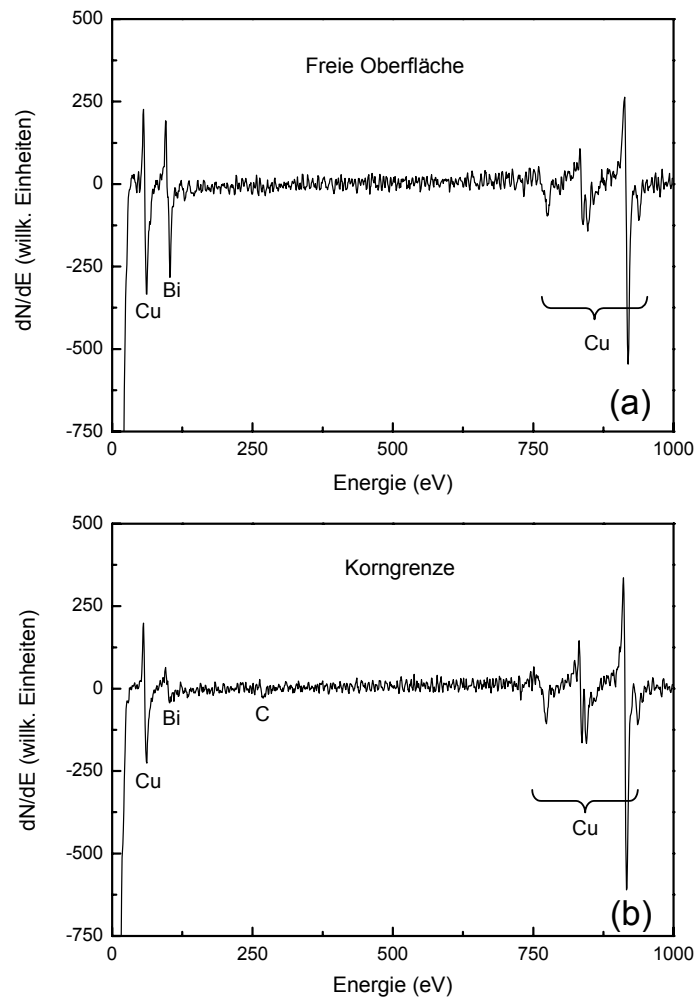


Bild 7.2. Differentielle AES-Spektren der freien Oberflächen von inneren Hohlräumen und der Korngrenze eines Cu-51 At.-ppm Bi Zweikristalls, der 6 h bei 1173 K ausgelagert wurde.

7.3. Löslichkeit von C in festem Cu

Es ist seit langem bekannt, dass sich C in festem Cu nur sehr wenig löst. Allerdings sind die verfügbaren Literaturdaten [38,43] sehr widersprüchlich. Die genaue Kenntnis des möglichen Verunreinigungsgehalts in hochreinen Metallen ist aber in modernen Fertigungsprozessen unabdingbar. Deshalb wurden in dieser Arbeit erstmals zuverlässige Daten zur Löslichkeit von C in festem Cu ermittelt.

In der Vergangenheit wurde die Verbrennungsmethode erfolgreich angewandt, um den C-Gehalt in Stählen zu bestimmen. Wegen systematischer Fehler, wie z.B. Adsorption kohlenstoffhaltiger Stoffe, war die Nachweisgrenze größer als 1 Gew.-ppm. Eine verbesserte Verbrennungsmethode wurde Ende der 80er Jahre entwickelt, und mit Hilfe neuer hochempfindlicher Infrarotzellen als CO₂-Detektor konnte die Nachweisgrenze reduziert werden [44,45]. Diese Methode wurde in dieser Arbeit verwendet.

Um die Gleichgewichtslöslichkeit von C in festem Cu zu bestimmen, wurden Cu-Proben mit C beschichtet und unter Vakuum bei 1143, 1223 und 1293 K für 72 und 240 h ausgelagert. Das verwendete Cu hatte einen C-Gehalt, der unter der neuen Nachweisgrenze (0,2 Gew.-ppm) lag. Wichtig war, dass die Proben, die bei einer bestimmten Temperatur unterschiedlich lang ausgelagert wurden, die gleichen C-Gehalte aufwiesen (Tabelle 3.1). Deshalb sind die ermittelten Löslichkeiten Gleichgewichtswerte. Sie sind 50 mal kleiner als die in der letzten Version des Cu–C-Zustandsdiagramms veröffentlichten Daten [37,38] zur Löslichkeit von C in festem Cu (Bild 7.3). Die Temperaturabhängigkeit der Löslichkeit gehorcht dem Henryschen Gesetz für interstitielle Mischkristalle. Die partielle Lösungsenthalpie von C in festem Cu beträgt 35,1 kJ/mol.

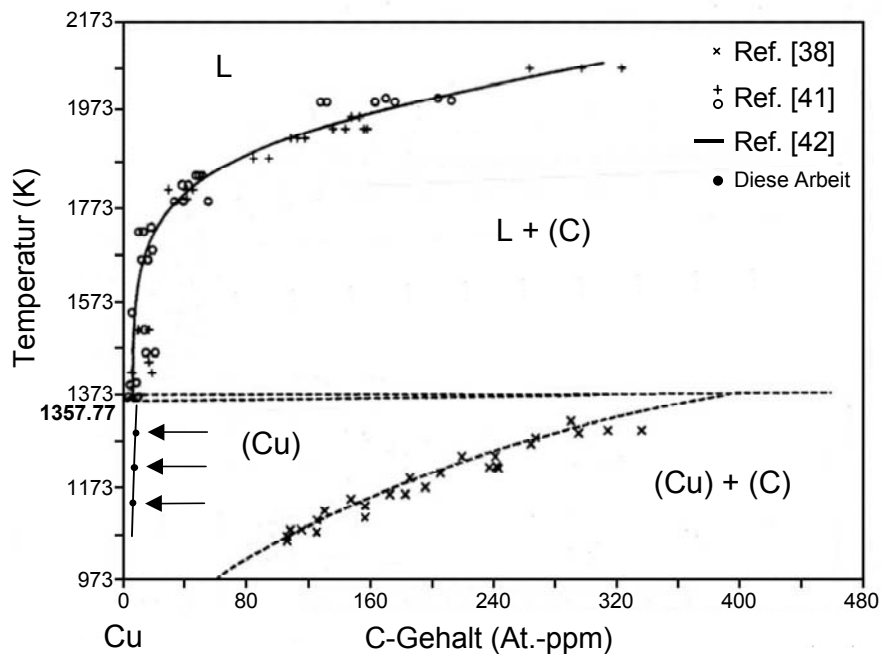


Bild 7.3. Cu-reiche Seite des Zustandsdiagramms Cu–C nach Ref. [37]; L = Schmelze. Die in dieser Arbeit neubestimmten Werte zur Löslichkeit von C in festem Cu sind zum Vergleich eingezeichnet. Sie liegen um etwa den Faktor 50 niedriger als die von McLellan [38] angegebenen Werte.

7.3. Diskontinuierliche Ausscheidung in einer Cu-4,5 At.-% In-Legierung

Bei der diskontinuierlichen Ausscheidung bildet sich in einem übersättigten Mischkristall – durch Auslagerung bei einer entsprechenden Temperatur – ein meist lamellares Zweiphasengefüge. Das Wachstum erfolgt durch Diffusion entlang der in den übersättigten Mischkristall hineinwandernden Reaktionsfront. Diese Reaktion weist senkrecht zur Reaktionsfront zwei charakteristische Merkmale auf: die Orientierung der Matrix beiderseits der Reaktionsfront ist verschieden und die Matrixkonzentration weist einen sprunghaften Übergang auf.

Seit den 70er Jahren ist die analytische Elektronenmikroskopie eine wertvolle Untersuchungsmethode, um Änderungen der chemischen Zu-

sammensetzung, die die diskontinuierliche Ausscheidung begleiten, zu untersuchen [50–52]. In letzter Zeit hat die *lokale* Analyse (anstelle der bislang verwendeten *globalen* Analyse) der Wachstumskinetik der diskontinuierlichen Ausscheidung an Bedeutung gewonnen. In dieser Arbeit wurde zum ersten Mal durch eine lokale Analyse der Wachstumskinetik der diskontinuierlichen Ausscheidungsreaktion die Diffusivität individueller Korngrenzen in einer Cu-4.5 At.-% In-Legierung bestimmt.

Proben dieser Legierung wurden mit einer Korngröße von 30–300 μm hergestellt. Anschließend wurde die diskontinuierliche Ausscheidung durch zweistufige Auslagerung gestartet. Die Bestimmung des Lamellenabstands, der Reaktionsfrontgeschwindigkeit und der Konzentrationsgradienten erfolgte mit einem Durchstrahlungselektronenmikroskop (Philips CM 20 Twin). Die in den entmischten Lamellen verbleibenden Konzentrationsgradienten wurden durch energiedispersive Röntgenanalyse bestimmt. Zwei Gruppen von Konzentrationsgradienten konnten unterschieden und quantitativ modelliert werden, nämlich symmetrische und asymmetrische Profile (Bild 7.4).

Die Korngrenzendiffusivitäten wurden aus den gefitteten Konzentrationsprofilen berechnet. Die in dieser Arbeit lokal bestimmten Werte stimmen gut überein mit den in der Literatur angegebenen Korngrenzendiffusivitäten, die durch eine globale Analyse ermittelt wurden (Bild 7.5). Die bei jeder Temperatur bestimmten unterschiedlichen Werte stellen keine Streuung im Sinne einer Messunsicherheit dar, sondern sind durch die individuellen Eigenschaften der unterschiedlichen Korngrenzen bestimmt. Wie aus Bild 7.5 zu ersehen, unterscheiden sich wandernde und stationäre Korngrenzen im Diffusionsvermögen nicht wesentlich.

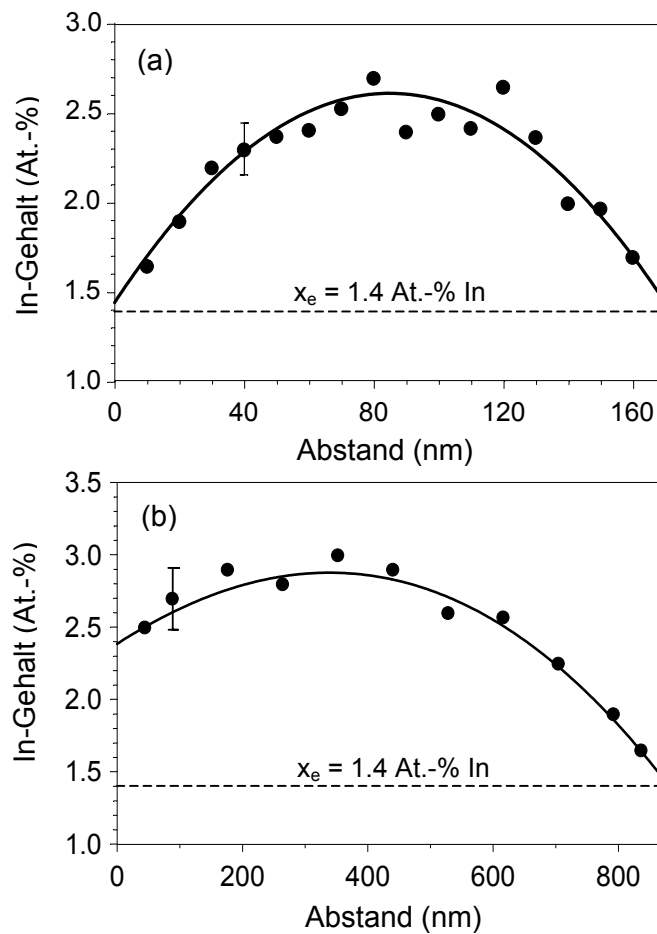


Bild 7.4. Beispiele von symmetrischen (a) und asymmetrischen (b) In-Konzentrationsprofilen senkrecht zu einer α -Lamelle in einer Cu-4.5 At.-% In-Probe, die zunächst 10 h bei 600 K und danach 10 h bei 550 K ausgelagert wurde. Die Gleichgewichtskonzentration x_e [76] in der α -Lamelle an der α/δ -Grenzfläche ist zur Orientierung eingezeichnet (lokales Gleichgewicht). α ist der entleerte Mischkristall und δ die ausgeschiedene Phase.

7.5. Korngrenzenphasenumwandlungen im System Al-Mg und ihr Einfluss auf die Superplastizität

Wie schon erwähnt, können alle Vorgänge, die die Grenzflächeneigenschaften verändern, das Verhalten eines Materials stark beeinflussen. Die Korngrenzenbenetzung ist einer dieser Vorgänge. Kurz dargestellt, besteht die Benetzung aus dem Ersatz einer Korngrenze durch zwei Pha-

sengrenzen mit einer insgesamt kleineren Grenzflächenenergie. Für die extrem große Plastizität von Al–Mg–Zn-Legierungen gab es bislang keine eindeutige Erklärung. Hier wird als eine mögliche Ursache die untersuchte Korngrenzenbenetzung vorgeschlagen.

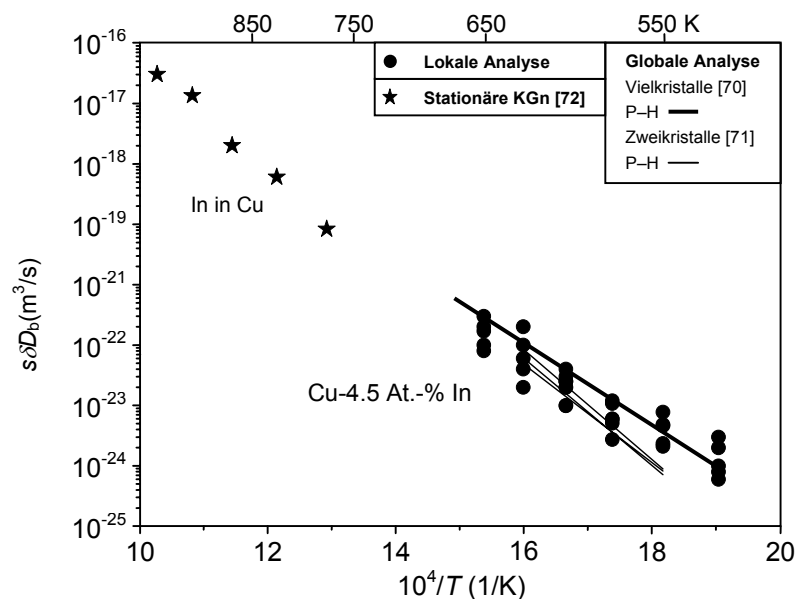


Bild 7.5. Arrhenius-Diagramm der Korngrenzendiffusivität $s\delta D_b$ der wandernden Reaktionsfront im Falle der diskontinuierlichen Ausscheidung in Cu-4,5 At.-% In. Die in dieser Arbeit lokal ermittelten Werte werden zum einen mit globalen Werten gemäß dem Petermann–Hornbogen-Modell (Eq. (4.6)) und zum anderen mit Daten zur Tracerdiffusion von In in stationären Korngrenzen von Cu verglichen.

Im System Al–Mg wurde die konventionelle Korngrenzenbenetzung durch eine *flüssige* Phase metallographisch erstmals untersucht. Hierzu wurden Proben im Zweiphasengebiet des Zustandsdiagramms bei unterschiedlichen Temperaturen ausgelagert. Nach Auslagerung bei einer relativ hohen Temperatur (883 K) waren alle Korngrenzen benetzt (Bild 7.6a), wohingegen bei einer relativ tiefen Temperatur (803 K) keine benetzten Korngrenzen beobachtet wurden (Bild 7.6b).

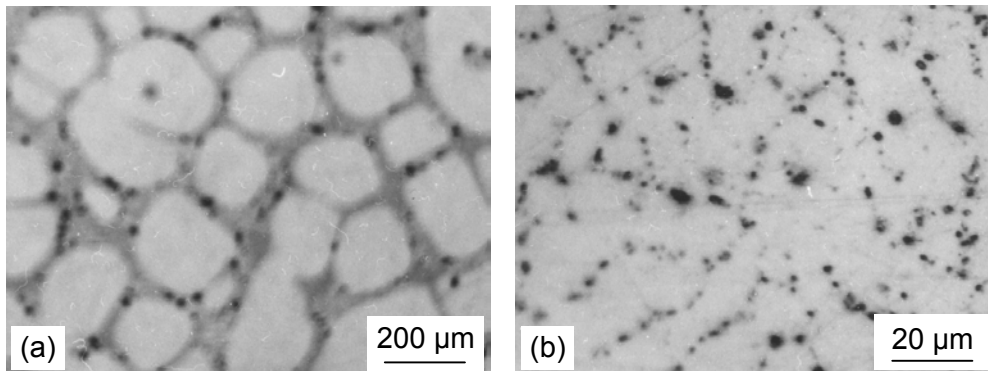


Bild 7.6. Lichtmikroskopische Aufnahmen von Proben, die 1 h lang bei 883 K (a) und 803 K (b) ausgelagert wurden.

Die Temperaturabhängigkeit des Anteils benetzter Korngrenzen ist in Bild 7.7 dargestellt. Daraus wurden die maximale und minimale Temperatur, bei der die Korngrenzenbenetzung 100 bzw. 0 % beträgt, ermittelt und in das Zustandsdiagramm eingetragen.

Eine Analyse der in der Literatur veröffentlichten Beiträge zur Plastizität von Al-Basis-Legierungen zeigte, dass dieses Phänomen unterhalb der Solidustemperatur auftritt. Das Auftreten einer Vorbenetzung von Korngrenzen im einphasigen Bereich des Zustandsdiagramms wird deshalb als Erklärung für das enorme superplastische Verhalten von Al-Basis-Legierungen vorgeschlagen.

7.6. Benetzung durch eine feste Phase: Gefügeentwicklung in einer Zn-5 Gew.-% Al-Legierung

In dieser Arbeit wurde zum ersten Mal die Gefügeentwicklung in einer Zn-5 Gew.-% Al-Legierung hinsichtlich Korngrenzenbenetzung durch eine feste Phase untersucht. Hierzu wurden Proben dieser Legierung bei verschiedenen Temperaturen für 336, 672 und 2016 h ausgelagert (Bild 7.8).

Querschliffe wurden unter Verwendung von Licht- und Rasterelektronenmikroskopie, Röntgenbeugung und Mikrosonde untersucht.

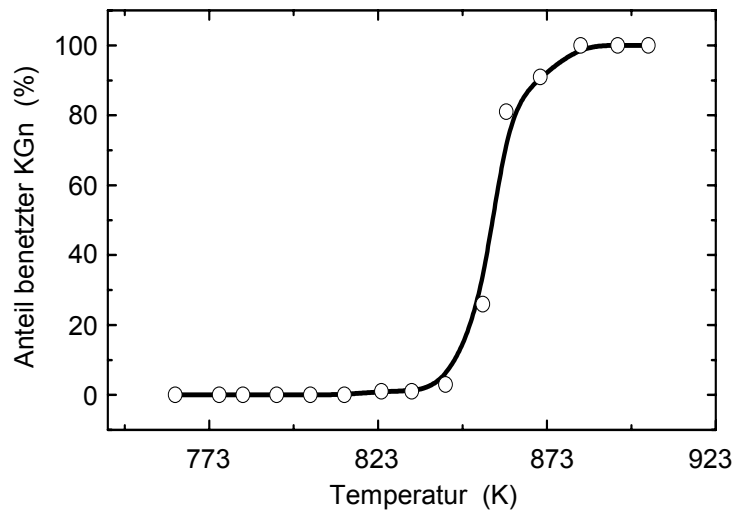


Bild 7.7. Temperaturabhängigkeit des Anteils benetzter Korngrenzen im System Al–Mg.

Im Ausgangsmaterial wurden keine Ausscheidungen an den Korngrenzen beobachtet. Nach Auslagerung bei relativ hohen Temperaturen wurden die (Zn)/(Zn)-Korngrenzen durch eine Schicht der festen Phase (Al) vollständig benetzt (Bild 7.9b). Bei einer relativ tiefen Temperatur wurden nur isolierte Teilchen der festen Phase (Al) an den Korngrenzen beobachtet (Bild 7.9a). Ein direkter Vergleich zwischen den beiden Korngrenzenzuständen ist in Bild 7.9c zu sehen: eine vollständig benetzte Korngrenze liegt horizontal im Querschliff und trifft zwei andere Korngrenzen am Tripelpunkt, die nicht benetzt sind. In einer der nicht-benetzen Korngrenzen ist der Kontaktwinkel angegeben (86°).

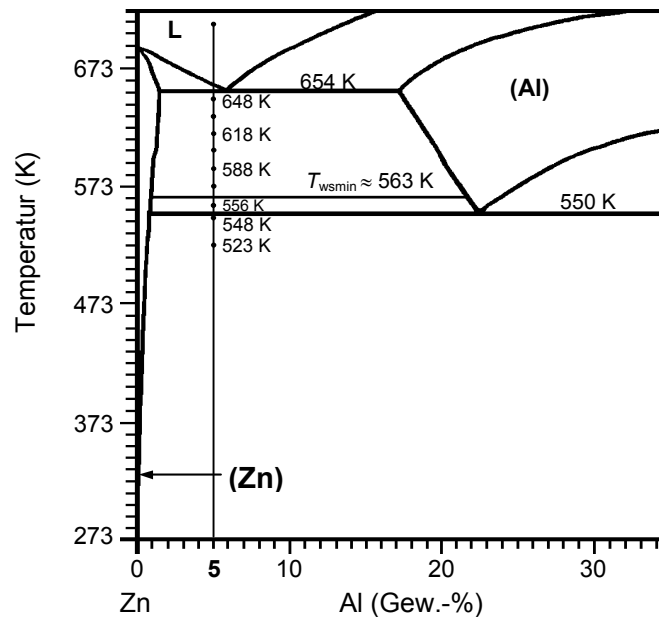


Bild 7.8. Zn-reiche Seite des Zustandsdiagramms Zn–Al [19]. Die vertikale dünne Linie kennzeichnet die untersuchte Legierung (Zn-5 Gew.-% Al). Die Punkte auf dieser Linie geben die angewandten Temperaturen an. Die Konode $T_{wsmin} \approx 563$ K gibt die minimale Temperatur an, bei der gerade noch keine (Zn)/(Zn)-Korngrenzen von der festen (Al)-Phase benetzt wurden.

Die Temperaturabhängigkeit des Anteils benetzter (Zn)/(Zn)-Korngrenzen, die vollständig von der festen Phase (Al) benetzt sind, ist in Bild. 7.10 dargestellt. Wie zu erwarten, nimmt die Benetzung mit steigender Temperatur zu. Die minimale Temperatur, bei der Benetzung stattfindet, liegt bei ca. 563 K.

Zusätzlich wurde die Wachstumskinetik der Ausscheidungen an den Korngrenzen untersucht. Es liegt ein parabolisches Wachstum vor. Die Aktivierungsenergie des Wachstums stimmt sehr gut mit der der Volumenselbstdiffusion in Zn überein. Deshalb wird das Wachstum der Ausscheidungen durch die Volumendiffusion kontrolliert.

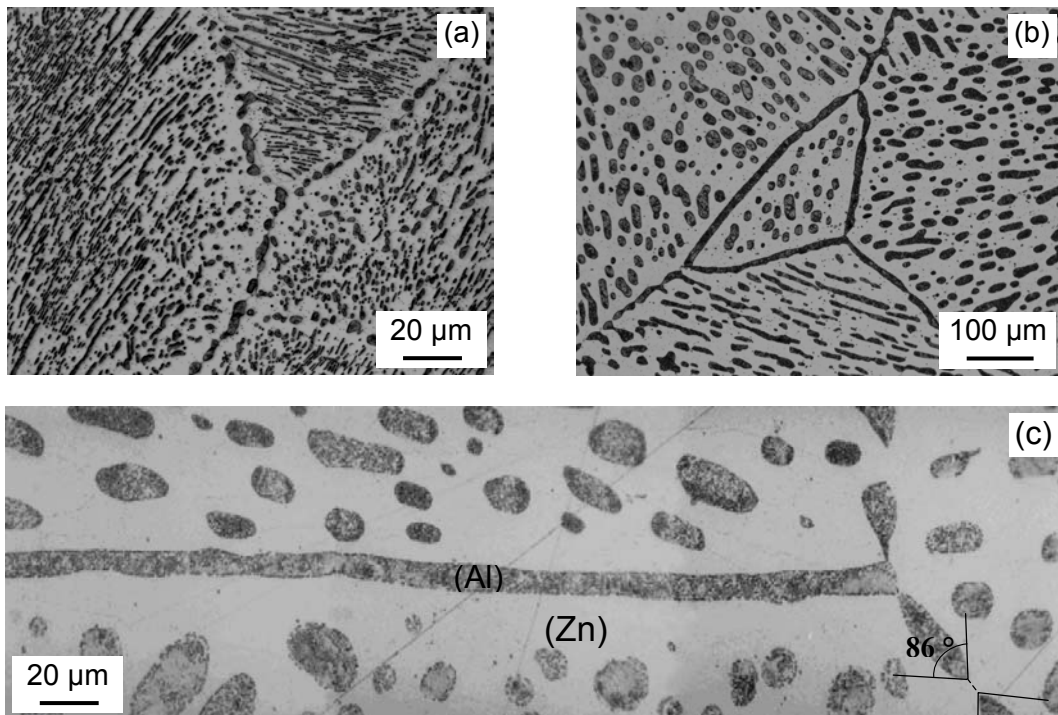


Bild 7.9. Lichtmikroskopische Aufnahmen (Querschliffe) von Proben, die 672 h bei 523 K (a), 648 K (b) und 618 K (c) ausgelagert wurden.

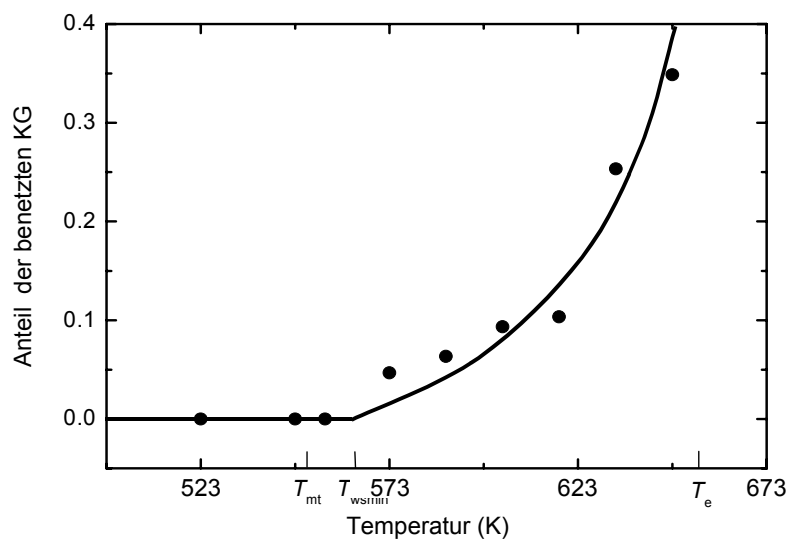


Bild. 7.10. Temperaturabhängigkeit des Anteils der benetzten (Zn)/(Zn)-Korngrenzen, die vollständig von der festen Phase (Al) benetzt sind. T_{mt} und T_e sind die monotektoide bzw. eutektische Temperatur. T_{wsmin} ist die minimale Temperatur, bei der die Korngrenzenbenetzung durch (Al) einsetzt. Die experimentellen Punkte sind Mittelwerte der in Tabelle 6.1 für die einzelnen Temperaturen angegebenen Werte.

7.7. Zusammenfassung und Ausblick

Das Ziel dieser Arbeit war es, zum Verständnis der Grenzflächenphänomene in Cu- oder Al-Legierungen beizutragen. Als besonderer Erfolg ist zu erwähnen, dass erstmals die Gleichgewichtssegregation von Bi an freien Oberflächen in Cu gemessen wurde. Dies gelang durch eine besondere Probenherstellung, die zudem einen direkten Vergleich zwischen der Segregation an Korngrenzen und freien Oberflächen erlaubte. Eine detaillierte Untersuchung der Wachstumskinetik der diskontinuierlichen Ausscheidung erfolgte im System Cu–In. Daraus konnte gefolgert werden, dass die Diffusivität von wandernden und stationären Korngrenzen ähnlich sind. Erstmals wurde auch die Korngrenzenbenetzung durch eine feste Phase beobachtet und quantitativ untersucht.

Diese Arbeit wurde somit mit erheblichem Erfolg abgeschlossen, aber natürlich regt sie auch zu weiteren Untersuchungen an. So wäre zum Beispiel die Bi-Segregation an Grenzflächen in Cu für andere Misorientierungen der Zweikristalle zu untersuchen.

Durch Untersuchung der diskontinuierlichen Ausscheidung lassen sich Daten zur Korngrenzendiffusivität für Systeme und/oder Temperaturen ermitteln, für die es keine Radiotracerdaten gibt. Mit den aktuellen Fortschritten in der Durchstrahlungselektronenmikroskopie lässt sich heutzutage eine laterale Auflösung von ca. 3 nm erreichen. So könnte man auch den zu erwartenden Konzentrationsgradienten entlang der Reaktionsfront der diskontinuierlichen Ausscheidung bestimmen. Einige Messungen zu dieser Thematik wurden schon unternommen. Dann könnte man den reinen Korngrenzendiffusionskoeffizienten anstatt des üblichen Tripelproduktes bestimmen.

Die Korngrenzenbenetzung in den Systemen Al–Mg und Zn–Al sollte zukünftig unter definierten Bedingungen an Zweikristallen untersucht wer-

den. Unter diesen Bedingungen könnte man den Kontaktwinkel in Abhängigkeit von der Temperatur messen und den „Dewetting“-Vorgang untersuchen.

References

- [1] J.W. Christian. *The theory of transformations in metals and alloys* (2nd edition). Oxford: Pergamon Press (1975).
- [2] D. Wolf, S. Yip. *Materials interfaces*. London: Chapman & Hall (1992).
- [3] A.P. Sutton, R.W. Balluffi. *Interfaces in crystalline materials*. Oxford: Clarendon Press (1995).
- [4] E.D. Hondros, M.P. Seah, S. Hofmann, P. Lejcek. In: R.W. Cahn, P. Haasen, editors. *Physical metallurgy*, vol. 2. Amsterdam: North-Holland (1996). p. 1201.
- [5] S. Hofmann, P. Lejcek. *Interface Sci.* 3 (1996) 241.
- [6] P. Lejcek, S. Hofmann. *Crit. Rev. Solid State Mater. Sci.* 20 (1995) 1.
- [7] P. Lejcek. *Surf. Interface Anal.* 30 (2000) 321.
- [8] E.D. Hondros, M.P. Seah. *Int. Met. Rev.* 22 (1977) 262.
- [9] C. Uebing. *Heter. Chem. Rev.* 3 (1996) 351.
- [10] E. Clauberg, C. Uebing, H. Viefhaus, H.J. Grabke. *Surf. Sci.* 454–456 (2000) 613.
- [11] P.A. Dowben, A. Miller, editors. *Surface segregation phenomena*. Boca Raton, FL: CRC Press (1990).
- [12] M.P. Seah, C. Lea. *Phil. Mag.* 31 (1975) 627.
- [13] T. Muschik, S. Hofmann, W. Gust. *Scripta Metall.* 22 (1988) 349.
- [14] T. Muschik, S. Hofmann, W. Gust, B. Predel. *Appl. Surf. Sci.* 37 (1989) 439.
- [15] A. Larere, M. Guttman, P. Dumoulin, C. Roques–Carnes. *Acta Metall.* 30 (1982) 685.
- [16] C. White. *J. Vac. Sci. Technol. A* 4 (1986) 1633.
- [17] A. Larere, K. Masuda–Jindo, R. Yamamoto, M. Doyama. In: Y. Ishida, editor. *Grain boundary structure and related phenomena*, Proc.

- 4th Jpn. Inst. Met. Int. Symp., *Trans. Jpn. Inst. Met. Suppl.* 27 (1986) 229.
- [18] T. Liu, C.L. White, J.A. Horton. *Acta Metall.* 33 (1985) 213.
- [19] P. Lejcek, A.V. Krajinikov, Y.N. Ivashchenko, M. Militzer, J. Adámek. *Surf. Sci.* 280 (1993) 325.
- [20] M.P. Seah. *Acta Metall.* 28 (1980) 955.
- [21] J.R. Rice. In: A.W. Thompson, I.M. Bernstein, editors. *Effect of hydrogen on behaviour of materials*. New York: The Metallurgical Society of AIME (1976). p. 455.
- [22] J.P. Hirth, J.R. Rice. *Metall. Trans. A* 11 (1980) 1501.
- [23] A. Joshi, D.F. Stein. *J. Inst. Met.* 99 (1971) 178.
- [24] L.S. Chang, B.B. Straumal, E. Rabkin, W. Gust, F. Sommer. *J. Phase Equilibria* 18 (1997) 128.
- [25] L.S. Chang, E. Rabkin, B.B. Straumal, B. Baretzky, W. Gust. *Acta Mater.* 47 (1999) 4041.
- [26] L.S. Chang, E. Rabkin, S. Hofmann, W. Gust. *Acta Mater.* 47 (1999) 2951.
- [27] S. Sigle, L.S. Chang, W. Gust. *Phil. Mag. A* 82 (2002) 1595.
- [28] C. Molinari, J.C. Joud. In: P. Lacombe, editor. *Physical chemistry of solid state: applications to metals and their compounds*. Amsterdam: Elsevier (1984). p. 151.
- [29] B.D. Powel, D.P. Woodruff. *Phil. Mag.* 34 (1976) 169.
- [30] M. Menyhard, B. Blum, C.J. Jr. McMahon. *Acta Metall.* 37 (1989) 549.
- [31] D. Wolf. *Acta Metall. Mater.* 38 (1990) 781.
- [32] A. Fraczkiewicz, M. Biscondi. *J. Phys.* 46 (1985) C4-497.
- [33] D. McLean. *Grain boundaries in metals*. Oxford: Clarendon (1957).
- [34] M. Menyhard, B. Blum, C.J. Jr. McMahon, S. Chikwambani, J. Weertman. *J. Phys.* 49 (1988) C5-457.
- [35] J.R. Michael, D.B. Williams. *Metall. Trans. A* 15 (1984) 99.

- [36] B.W. Kempshall, B.I. Prenitzer, L.A. Gianuzzi. *Scripta Mater.* 47 (2002) 447.
- [37] P.R. Subramanian, D.E. Laughlin. In: P.R. Subramanian, D.J. Chakrabarti, D.E. Laughlin, editors. *Phase diagrams of binary copper alloys. Monograph series on alloy phase diagrams*, vol. 10. Materials Park, OH: ASM International (1994). p. 109.
- [38] R.B. McLellan. *Scripta Metall.* 3 (1969) 389.
- [39] S. Dorfman, D. Fuks. *Compo. Sci. Technol.* 57 (1997) 1065.
- [40] S. Dorfman, D. Fuks. *Compos. Part A–Appl. S.* 27 (1996) 697.
- [41] M.B. Bever, C.F. Floe. *T. Metall. Soc. AIME* 166 (1946) 128.
- [42] L.L. Oden, N.S. Gokcen. *Metall. Trans. B* 23 (1992) 453.
- [43] G. Mathieu, S. Guiot, J. Cabané. *Scripta Metall.* 7 (1973) 421.
- [44] K. Gretzinger, E. Grallath, G. Tölg. *Anal. Chim. Acta* 193 (1987) 1.
- [45] W. Gruner, E. Grallath. *Steel Res.* 66 (1995) 455.
- [46] R.B. McLellan. In: P.S. Rudman, J. Stringer, R.I. Jaffee, editors. *Phase stability in metals and alloys*. New York: McGraw–Hill (1966). p. 398.
- [47] A.D. Le Claire. In: H. Mehrer, editor. *Landolt–Börnstein; Diffusion in solid metals and alloys*, vol. 26. Berlin: Springer (1990). p. 498.
- [48] D.B. Williams, E.P. Butler. *Int. Met. Rev.* 26 (1981) 153.
- [49] I. Manna, S.K. Pabi, W. Gust. *Int. Mater. Rev.* 46 (2001) 53.
- [50] D.A. Porter, D.B. Williams, J.W. Edington. *Proc. 8th Int. Congr. on Electron Microscopy*, vol. 1. Canberra: The Australian Academy of Sciences (1974). p. 656.
- [51] D.B. Williams, J.W. Edington. *Acta Metall.* 24 (1976) 323.
- [52] D.A. Porter, J.W. Edington. *Proc. Roy. Soc. Lond. A* 358 (1977) 335.
- [53] J.W. Cahn. *Acta Metall.* 7 (1959) 18.
- [54] I.G. Solorzano, G.R. Purdy, G.C. Weatherly. *Acta Metall.* 32 (1984) 1709.
- [55] P. Zieba. *Mikrochim. Acta* 15 Suppl. (1998) 73.

- [56] P. Zieba, W. Gust. *Scripta Mater.* 39 (1998) 13.
- [57] P. Zieba. *Acta Mater.* 46 (1998) 369.
- [58] P. Zieba, G. Cliff, G.W. Lorimer. *Acta Mater.* 45 (1997) 2093.
- [59] D. Duly, M.C. Cheynet, Y. Brechet. *Acta Metall. Mater.* 42 (1994) 3843.
- [60] D. Duly, M.C. Cheynet, Y. Brechet. *Acta Metall. Mater.* 42 (1994) 3855.
- [61] K.B. Alexander. *The growth kinetics of cellular precipitation*, Ph.D. Thesis, Carnegie–Mellon University, Pittsburgh, PA, 1985.
- [62] P. Zieba, W. Gust. *Z. Metallkd.* 88 (1997) 270.
- [63] P. Zieba, W. Gust. *Acta Mater.* 47 (1999) 2641.
- [64] P. Zieba, W. Gust. *Z. Metallkd.* 92 (2001) 645.
- [65] P. Zieba. *Local characterization of the chemistry and kinetics in discontinuous solid state reactions*. Cracow, Poland: Orekop Ltd. (2001).
- [66] J.M. Shapiro, J.S. Kirkaldy. *Acta Metall.* 16 (1968) 1239.
- [67] R.A. Fournelle, J.B. Clark. *Metall. Trans.* 3 (1972) 2757.
- [68] B. Predel, W. Gust. *Mater. Sci. Eng.* 17 (1975) 41.
- [69] I.G. Solorzano, M. Audier. *Proc. 50th Annual Meeting of the Electron Microscopy Society of America*. San Francisco, CA: San Francisco Press (1992). p. 26.
- [70] W. Gust. *Investigation of the growth kinetics, thermodynamics and diffusion for the discontinuous precipitation reaction*. Habilitation Thesis, University of Stuttgart, Stuttgart, Germany (1980). p. 125.
- [71] W. Gust, B. Predel, U. Roll. *Acta Metall.* 28 (1980) 1395.
- [72] I. Kaur, W. Gust, L. Kozma. *Handbook of grain and interphase boundary diffusion data*. Stuttgart, Germany: Ziegler (1989). p. 397.
- [73] I.G. Solorzano, W. Gust. *Mater. Sci. Forum* 94–96 (1992) 659.
- [74] P. Zieba, W. Gust. *Arch. Metall.* 43 (1998) 217.
- [75] G. Cliff, G.W. Lorimer. *J. Microsc.–Oxford* 103 (1975) 203.

- [76] P.R. Subramanian, D.E. Laughlin: *Bull. Alloy Phase Diagr.* 10 (1989) 554.
- [77] I.G. Solorzano, M.F.S. Lopes. In: G.W. Lorimer, editor. *Phase transformations*. London, UK: The Institute of Metals (1988). p. 242.
- [78] G.P. Geber, R. Kirchheim. *Acta Mater.* 45 (1997) 2167.
- [79] J. Petermann, E. Hornbogen. *Z. Metallkd.* 59 (1968) 814.
- [80] T.H. Chuang, R.A. Fournelle, W. Gust, B. Predel. *Trans. Jpn. Inst. Met.* 27 Suppl. (1986) 419.
- [81] A. Bögel, W. Gust. *Z. Metallkd.* 79 (1988) 296.
- [82] W. Gust, C. Ostertag, B. Predel, U. Roll. *Philos. Mag. A* 47 (1983) 395.
- [83] T.G. Langdon, T. Watanabe, J. Wadsworth, M.J. Mayo, S.R. Nutt, M.E. Kassner. *Mater. Sci. Eng. A* 166 (1993) 237.
- [84] E.I. Rabkin, V.N. Semenov, L.S. Shvindlerman, B.B. Straumal. *Acta Metall. Mater.* 39 (1991) 627.
- [85] O.I. Noskovich, E.I. Rabkin, V.N. Semenov, B.B. Straumal, L.S. Shvindlerman. *Acta Metall. Mater.* 39 (1991) 3091.
- [86] B.B. Straumal, O.I. Noskovich, V.N. Semenov, L.S. Shvindlerman, W. Gust, B. Predel. *Acta Metall. Mater.* 40 (1992) 795.
- [87] B. Straumal, E. Rabkin, W. Lojkowski, W. Gust, L.S. Shvindlerman. *Acta Mater.* 45 (1997) 1931.
- [88] B.B. Straumal, W. Gust. *Mater. Sci. Forum* 207–209 (1996) 59.
- [89] B. Straumal, T. Muschik, W. Gust, B. Predel. *Acta Metall. Mater.* 40 (1992) 939.
- [90] B. Straumal, D. Molodov, W. Gust. *J. Phase Equilibria* 15 (1994) 386.
- [91] B. Straumal, V. Semenov, V. Glebovsky, W. Gust. *Defect Diff. Forum* 143–147 (1997) 1517.
- [92] L.S. Chang, E. Rabkin, B.B. Straumal, S. Hofmann, B. Baretzky, W. Gust. *Defect Diff. Forum* 156 (1998) 135.

- [93] B. Straumal, W. Gust, T. Watanabe. *Mater. Sci. Forum* 294–296 (1999) 411.
- [94] K. Higashi, S. Tanimura, T. Ito. *Mater. Res. Soc. Symp. Proc.* 196 (1990) 385.
- [95] M. Mabuchi, T. Imai. *J. Mater. Sci. Lett.* 9 (1990) 763.
- [96] T.G. Nieh, C.A. Henshall, J. Wadsworth. *Scripta Metall.* 18 (1984) 1405.
- [97] M. Mabuchi, K. Higashi, Y. Okada, S. Tanimura, T. Imai, K. Kubo. *Scripta Metall.* 25 (1991) 2003.
- [98] T.G. Nieh, P.S. Gilman, J. Wadsworth. *Scripta Metall.* 19 (1985) 1375.
- [99] K. Higashi, Y. Okada, T. Mukai, S. Tanimura. *Scripta Metall.* 25 (1991) 2053.
- [100] K. Higashi, T.G. Nieh, M. Mabuchi, J. Wadsworth. *Scripta Metall. Mater.* 32 (1995) 1079.
- [101] Y. Takayama, T. Tozawa, H. Kato. *Acta Mater.* 47 (1999) 1263.
- [102] T.B. Massalski et al., editors. *Binary alloy phase diagrams*. Materials Park, OH: ASM International (1993). p. 169.
- [103] H. Iwasaki, T. Mori, M. Mabuchi, K. Higashi. *Acta Mater.* 46 (1998) 6351.
- [104] J.W. Cahn. *J. Chem. Phys.* 66 (1977) 3667.
- [105] J.W. Cahn. *J. Phys. Colloq.* 43-C6 (1982) 199.
- [106] J. Schöllhammer, B. Baretzky, W. Gust, E. Mittemeijer, B. Straumal. *Interface Sci.* 9 (2001) 43.
- [107] D.A. Molodov, U. Czubyko, G. Gottstein, L.S. Shvindlerman, B.B. Straumal, W. Gust. *Phil. Mag. Lett.* 72 (1995) 361.
- [108] B. Baudelet, M.C. Dang, F. Bordeaux. *Scripta Metall. Mater.* 26 (1992) 573.
- [109] T. Imai, M. Mabuchi, Y. Tozawa, Y. Murase, J. Kusui. *Metal & ceramic matrix composites: processing, modelling & mechanical behaviour*. Warrendale, PA: TSM-ASME (1990). p. 124.

- [110] M. Mabuchi, K. Higashi, T. Imal, K. Kubo. *Scripta Metall.* 25 (1991) 1675.
- [111] N. Furushiro, S. Hori, Y. Miyake. In: S. Hori et al., editors: *Proc. Int. Conf. Superplast. Adv. Mater. (ICSAM-91)*. Sendai: Japan Soc. Res. Superplast. (1991). p. 557.
- [112] As Ref. [1]. p. 452.
- [113] C. Herring. In: W.E. Kingston, editor. *The physics of powder metallurgy*. New York: McGraw–Hill (1951). p. 143.
- [114] I.I. Novikov. *Theory of thermal treatment of metals* (4th ed.). Moscow: Metallurgia (1986). p. 480 [in Russian].
- [115] H. Schumann. *Metallography* (13rd ed.). Leipzig: Deutscher Verlag für Grundstoffindustrie (1991) [in German].
- [116] Y.E. Geguzin. *Physics of sintering* (2nd ed.). Moscow: Nauka (1984). p. 280 [in Russian].
- [117] V.N. Eremenko, Y.V. Naidich, I.A. Lavrinenko. *Sintering in the presence of liquid phase*. Kiev: Naukova Dumka (1968). p. 132 [in Russian].
- [118] V.V. Skorokhod, V.V. Panichkina, N.K. Prokushev. *Poroshk Metall* 8 (1986) 14 [in Russian].
- [119] W.J. Huppmann, H. Riegger. *Acta Metall.* 23 (1975) 965.
- [120] M.J. Iribarren, O.E. Agüero, F. Dymont. *Defect Diff. Forum* 194–199 (2001) 1211.
- [121] I. Apykhtina, B. Bokstein, A. Khusnutdinova, A. Peteline, S. Rakov. *Defect Diff. Forum* 194–199 (2001) 1331.
- [122] N. Eustathopoulos, L. Coudurier, J.C. Joud, P.J. Desre. *J. Crystal Growth* 33 (1976) 105.
- [123] E. Rabkin, D. Weygand, B. Straumal, V. Semenov, W. Gust, Y. Brechet. *Phil. Mag. Lett.* 73 (1996) 187.
- [124] Chapter 5 in this thesis.
- [125] G.A. López, B.B. Straumal, W. Gust, E.J. Mittemeijer. In: M.J. Zehetbauer, R.Z. Valiev, editors. *Nanomaterials by severe plastic de-*

- formation. Fundamentals – processing – applications*. Weinheim: Wiley–VHC (2004). p. 642.
- [126] As Ref. [102]. p. 239.
- [127] J.L. Puchou, E. Pichoir. *La Res. Aerospaciale* 3 (1984) 13.
- [128] T. Muschik, W. Laub, M.W. Finnis, W. Gust. *Z. Metallkd.* 84 (1993) 596.
- [129] A.I. Barg, E. Rabkin, W. Gust. *Acta Metall. Mater.* 43 (1995) 4067.
- [130] N.L. Peterson, S.J. Rothman. *Phys. Rev.* 163 (1967) 645.
- [131] H. Mehrer, editor. Landolt–Börnstein, vol. 26, *Diffusion in solid metals and alloys*. Berlin: Springer-Verlag (1990). p. 192.

Danksagung

Eine Doktorarbeit durchzuführen und die entsprechende Dissertation anzufertigen, bleibt nicht auf die schreibende Person beschränkt. Mehrere Menschen werden in der einen oder anderen Weise beteiligt. Allen diesen gebührt mein Dank für ihre Geduld und ihre Bereitschaft zu helfen.

In erster Linie möchte ich mich bei Prof. Dr. Ir. E.J. Mittemeijer für die Aufnahme in seine Abteilung, für sein Interesse an dieser Arbeit sowie für die Übernahme des Hauptberichts bedanken. Insbesondere bedanke ich mich bei ihm für sein außergewöhnliches Engagement bei der fachlichen Betreuung. Die grundlegenden und zahlreichen Diskussionen mit ihm haben ganz wesentlich zum Erfolg dieser Arbeit beigetragen.

Herrn Prof. Dr. Dr. h. c. M. Rühle danke ich für die Übernahme des Mitberichts und Herrn Prof. Dr. F. Aldinger für die Zusage, als Mitprüfer dieser Dissertation zu wirken.

Zum Gelingen dieser Arbeit hat Prof. Dr. Dr. h. c. W. Gust, mein in den ersten Jahren dieser Arbeit täglicher Betreuer, in großem Masse beigetragen. Seine stete Diskussionsbereitschaft und wertvollen Ratschläge zu allen Fragestellungen wurden von mir sehr geschätzt.

Für das Ermutigen, eine Doktorarbeit in Deutschland durchzuführen, danke ich Prof. Dr. J.A. Vivas Hohl.

Herrn Prof. Dr. P. Zieba und Herrn Prof. Dr. B.B. Straumal möchte ich für die fachliche Unterstützung und erfolgreiche Zusammenarbeit speziell danken.

Allen Mitarbeitern des Max-Planck-Instituts sei für die gute Zusammenarbeit bei den kleinen und großen Problemen des Forschungsalltages und die angenehme Arbeitsatmosphäre gedankt.

Am Schluss möchte ich einen besonderen Dank für meine Familie aussprechen. Sie war immer da als Unterstützung aus der Ferne. Meiner Freundin, Rosana, danke ich in starkem Maße für ihre Geduld und ihren Beistand.

Curriculum Vitae

Gabriel Alejandro LÓPEZ

born on 13th of January 1975 in San Pedro, Argentina

School

- | | |
|-------------|---|
| 1981 – 1987 | School, “Escuela N° 35”, Gobernador Castro, Argentina |
| 1988 – 1993 | Secondary school, “E.E.T. N° 1”, San Pedro, Argentina |

Higher Education

- | | |
|---------------|--|
| 03/94 – 08/00 | University, “Universidad Nacional del Comahue”, Neuquén, Argentina
Diploma thesis: “Diffusion soldering in Ni/Al/Ni interconnections”
Degree: Chemical Engineer |
| 11/00 – 06/04 | Ph.D. at the Max Planck Institute for Metals Research and Institute of Physical Metallurgy, University of Stuttgart, Germany under supervision of Prof. Dr. Ir. E.J. Mittemeijer |
